Morphological and dynamic perturbations of autorotating samaras

A Dissertation Presented for the
Doctor of Philosophy
Degree
The University of Tennessee, Knoxville

Breanna Marie Schaeffer

December 2025

Dedication

To my husband, James

To my husband, my best friend, and my greatest encourager—thank you for being by my side through it all, for making space for late nights, long drafts, and endless edits. Your unwavering support turned this journey into one of joy. Through every challenge and triumph, your love and kindness have been a constant reminder of the power of perseverance and faith.

To my parents, John and Angie Cunningham

Who filled my life with love and my mind with the belief that I could achieve anything.

To Jesus Christ, my Redeemer—

To the One who called me, equipped me, and walked with me through every season: thank You for being my source of hope, peace, and purpose. To Him who is able to do immeasurably more than all I ask or imagine, be all the glory.

With deepest appreciation,
Breanna

Acknowledgements

I would like to express my sincere gratitude to all those who contributed to this research. The support, expertise, and encouragement I received were truly invaluable.

I am especially grateful to Dr. Andrew Dickerson, whose mentorship, creativity, and critical insight shaped every stage of this work. His guidance consistently pushed me to think more deeply and explore new ideas. I also thank the University of Tennessee, Knoxville, for providing the fellowship that supported my academic journey and allowed the research to flourish. Special appreciation goes to Dr. Tadd Truscott, whose timely guidance and fresh perspective were instrumental at a critical point in the project.

Many dedicated undergraduate students made important contributions that enriched the quality and scope of the work. Through careful efforts in experimental setup, data collection, and video analysis, they played an essential role in the success of this research. I am thankful for Andrew Fuson, Colton Chandler, Colby Hale, Will Eriksson, Courtney Rose, Jaime Chapman, Lauren Harnetty, Ashlyn Garrett, Nathan McCollum, and Faylon Nixon—each brought curiosity and commitment that left a lasting impact.

Supportive labmates and collaborators—Gene, Emaz, and Jacob—offered insight, encouragement, and camaraderie that made the lab an inspiring and enjoyable place to work.

My heartfelt thanks go to my brother, John Cunningham; my sister, Brandee Cunningham; and my niece, Everlee, for their unwavering love and enthusiasm throughout this journey. Deep gratitude also goes to my parents, whose constant encouragement and support carried me forward. Early inspiration from my grandparents instilled a lifelong love of learning that laid the foundation for this academic path.

The steadfast friendship of Hannah, Whitney, Brianna, Mary Kay, and Casey has been a true gift. Moments of laughter, wisdom, and strength from each of you arrived exactly when needed.

To everyone who offered support, belief, or kindness along the way—thank you. Your presence made the journey not only possible but deeply meaningful.

The beginning of wisdom is this: Get wisdom, and whatever you get, get insight.
Proverbs 4:7

Abstract

Samaras, the winged seeds of trees such as maple, ash, and poplar, utilize passive aerodynamic mechanisms for wind-driven dispersal. While maple samaras are well-documented for their stable autorotation, rolling samaras, including those from ash and poplar species, exhibit a coupled rolling-autorotative motion that remains less understood. The aerodynamic mechanisms governing both maple and rolling samaras are characterized, with a particular focus on their response to morphological and dynamic perturbations. High-speed imaging, wind tunnel experiments, and computational modeling quantify the kinematics, aerodynamic stability, and recovery mechanisms of samaras under controlled conditions. The influence of mass distribution, wing morphology, and environmental perturbations—such as crosswinds and raindrop impacts—on dispersal efficiency is analyzed. Experimental results demonstrate that maple samaras maintain robust autorotation despite external disturbances, rapidly recovering from transient aerodynamic disruptions. In contrast, rolling samaras exhibit a more complex aerodynamic response, where rolling motion influences both stability and lateral displacement in turbulent environments. Bridging gaps in the understanding of natural dispersal mechanisms advances ecological studies of wind-dispersed seeds and informs bio-inspired flight applications, particularly in passive aerial vehicle design. Insights from this work contribute to improving seed dispersal models, optimizing conservation strategies, and inspiring innovations in bio-inspired robotics and micro-airborne systems.

Table of Contents

List of Figures

Chapter 1
Introduction

1.1 Motivation

This dissertation seeks to understand the physics of flight in nature and apply those insights to robust, adaptive technologies. Bio-inspired flight research has advanced micro air vehicles and autonomous delivery platforms by learning from insects[1–3], birds[4–6], and wind-dispersed seeds[7–9]. Fundamental questions in unsteady aerodynamics, vortex dynamics, and passive stability benefit from models that evolved for reliability rather than control.

Samaras from maple, poplar, and ash provide a uniquely informative model of passive yet stable flight[10–13]. Engineered flyers rely on control surfaces and feedback, whereas samaras achieve resilience through geometry and passive aeroelastic response, tolerating gusts[14] and even raindrop impacts[15]. Study of their structure–function relationships yields principles that translate naturally to simple, robust, and fault-tolerant vehicles.

Forests sustained by these genera underpin biodiversity, carbon storage, hydrologic regulation, and ecosystem stability[16–19]. Maple, poplar, and ash also support livelihoods through timber, urban canopy services, and syrup production in northern regions, making seed dispersal not only an ecological process but also a contributor to regional economies. Public statistics from agencies such as USDA NASS and Natural Resources Canada document the scale of maple production, and industry reports highlight its sensitivity to climate and forest health, reinforcing the need for accurate dispersal and regeneration models.

Important knowledge gaps remain regarding the kinematics and aerodynamics of rolling samaras, their performance in turbulence and crosswind, and their comparative efficacy relative to spinning samaras such as maple. The research addresses these gaps by resolving governing principles for rolling flight, quantifying environmental responses, and benchmarking performance against spinning counterparts. Insights advance fundamental flight science while informing conservation, reforestation, and design of bio-inspired aerial devices that are efficient, resilient, and environmentally aligned.

1.2 Flight of the samara

Plants employ diverse seed dispersal strategies to maximize reproductive success. Wind-dispersed samaras are winged achenes that exploit two dominant passive flight modes, au-

torotation characteristic of *Acer* (maple) and rolling common in *Fraxinus* (ash) and *Liriodendron* (poplar), with each strategy relying on distinct aerodynamic principles[10–13]. In autorotation, an offset center of mass and cambered wing establish a stable leading-edge vortex that produces lift and regulates descent rate[10,13]. In rolling, the seed rotates about its span while precessing, sampling crossflow over a cycle and converting wind energy into lateral drift that aids dispersal[11]. Morphology governs both behaviors, with aspect ratio, thickness-to-chord ratio, span, and mass setting key dimensionless groups and kinematic outcomes such as Reynolds number, moment of inertia, cone angle, and tip-speed ratio[12,13]. Passive stabilization enables resilience to gusts and even raindrop impacts[14,15]. Ecologically, these flight modes promote colonization, maintain genetic connectivity, and sustain forests that support biodiversity, carbon storage, and regional economies such as maple syrup production[16–19]. A mechanistic account of samara aerodynamics therefore advances fundamental flight science while informing conservation, reforestation, and the design of simple and fault-tolerant bio-inspired aerial systems.

1.2.1 Autorotation in samara flight

The mesmerizing aerial performance of the samara seeds, known as autorotation, has long captured the curiosity of both nature enthusiasts and scientists alike. Beyond their visual appeal, the autorotating flight of maple seeds, also called samaras, serves an ecological purpose. Samara-bearing trees have developed the ability to produce winged seeds as a means to enhance proliferation. The samara wings enable the seeds to leave the parent trees, extending their reproductive reach and enhancing the chances of successful establishment by increasing the time from tree to ground[13,14,20–22]. The subjects of this study, fruits of the genus *Acer* (*A.*) seeds vary in size, mass, and shape (**Fig.1.1**), yet maintain a tight band of descent velocities across species.

To increase the time from tree to ground, samaras slow their descent by autorotation that generates lift and exposes more of the samara area to oncoming air, increasing drag in descent. Samara seeds have developed a sophisticated interplay between morphological factors to facilitate autorotation. The winged structure of the seed increases the surface area exposed to the air, resulting in an aerodynamic drag force preventing the seed from falling rapidly[23], an ability that remains intact even in the presence of a strong crosswind[14]. The majority of samara mass is concentrated towards the heavier nutlet[10,24], such that on one side of the center-of-mass, the samara is denser and rounded. On the other side of the center-of-mass is the high-aspect-ratio, and higher drag wing. The result is that samaras autorate with the nutlet down to create a coning angle θ, shown in **Fig.2.2**a. Aerodynamic

Figure 1.1: Samara species tested in this study. The average span of the species increases from left to right.

and centrifugal forces of the spinning samara achieve equilibrium, imparting stability to both the angle of attack and coning angle during descent[13,25,26].

The relation between the dynamics of autorotation and the morphological features of samaras is complex, has been the focus of multiple previous studies[10,13,27–30], and is not yet fully characterized. Efforts to improve modeling accuracy by increasing complexity have not provided tools by which multiple samara species can be compared. Among the various aerodynamic variables measured, descent velocity V_d stands out as the most investigated quantity. The standard approach to link V_d to morphological characteristics, is what has been termed wing loading[27],

$$V_\mathrm{d}^2 \sim mg/A, \tag{1.1}$$

where m is samara mass, A is plan-view area, and g is the acceleration due to gravity. We present the relation between V_d^2 and mg/A for the samaras of this study shown in **Fig.3.1**a. Wing loading suitably assesses the loading profile of an individual wing across diverse speeds but proves less effective as a metric for comparing distinct wing shapes between *Acer* species– a distinction we explore in greater detail.

Furthermore, as we compile and analyze previous samara studies[8,27,31], a striking lack

of agreement between terminal velocity and wing loading becomes apparent, as depicted in **Fig.3.1**b. This recurring pattern strongly suggests that additional factors should be considered when forming a relationship that relates samara size to its rate of descent.

1.2.2 Rolling in samara flight

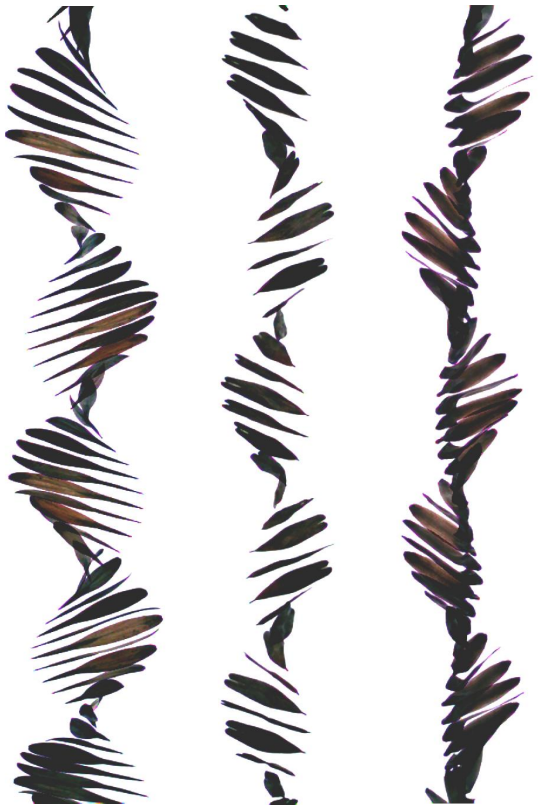

Figure 1.2: Composite image showing the descent of three different samara species—*Fraxinus americana*, *Fraxinus excelsior*, and *Liriodendron tulipifera* captured at 1000 fps. The images illustrate the differences in falling trajectories and rotational motion among species.

Aerodynamic adaptations for improved seed dispersal are exemplified by samaras, winged seeds that exploit autorotation to enhance wind-assisted travel by prolonging the time in flight[23,32]. Maple (*Acer spp.*) samaras descend solely through stable helical autorotation, whereas samaras from species such as (*Fraxinus spp.*) and tulip poplar (*Liriodendron tulipifera*) combine spanwise rolling with precession to produce a dual-axis rotation during descent[33] as seen in **Fig.1.2**. Both rolling and non-rolling samaras follow helical trajectories but differ in the aerodynamic mechanisms that produce lift. While descent dynamics of maple samaras have been well characterized, the aerodynamic role of rolling motion remains

largely unexplored, despite early observations recognizing that ash and tulip samaras rotate about both their spanwise and vertical axes[33].

Prior studies of autorotating samaras[34], fluttering plates[35,36], and tumbling parallelograms[37,38] reveal that morphological asymmetries and rotational dynamics significantly influence aerial trajectories. Fluttering involves oscillatory see-saw-like motion in which the falling plate does not flip, as is typical of falling paper[35,36]. Tumbling, in contrast, is characterized by end-over-end rotation driven by dynamic instabilities in aerodynamic torque[37,38]. Tumbling generates lift and lateral propulsion. Rolling is tumbling, but in the context of samaras, tumbling through a precessional rotation. The interplay between mass distribution, geometry, and rotational kinematics governs which descent mode–fluttering, tumbling, or rolling–is observed. Rolling samaras share descent characteristics with both non-rolling autorotators and tumbling plates.

Rolling motion introduces continuous reorientation of the wing relative to the airflow, fundamentally altering the aerodynamic forces compared to non-rolling autorotators. Unlike maple samaras, which maintain a relatively fixed angle of attack and generate lift through stable leading-edge vortices (LEVs)[39,40], rolling samaras experience periodic modulation of angle of attack as they rotate spanwise[41]. Dynamic rolling generates time varying lift force and torque, leveraging unsteady aerodynamic mechanisms similar to those observed in flapping insect flight[42].

1.2.3 Disturbance and resilience in samara flight

Raindrop impacts on samaras

Trees release their seeds across an array of atmospheric conditions from calm to blustery and torrential[43–45]. Those that drop their seeds with the aid of mechanical perturbation[9,46], such as wind, are likely to do so in the presence of rainfall. While seeds such as acorns and walnuts will be little affected by raindrop collisions during their descent, those that rely on high drag to slowly descend[47–50] are likely to encounter ballistic drops during their passive flight. Studies of aircraft[51,52] and flying animals[53] have demonstrated that rain slows flight. Encountering rainfall during flight is a shared experience among all biological flyers and gliders across several orders of magnitude in scale, from gnats to birds. Birds and bats experience decreased flight efficiency but are not notably pushed by drop impacts[25,53]. By contrast, small insects are displaced downward several body lengths and at high acceleration before their hydrophobicity and high drag profile permit separation from the drop and flight recovery[54–56]. Impacts with small insects weighing $\lesssim 3$ mg do not result in raindrop splashing whereas impacts with birds fracture drops.

Samaras from the genus *Acer* (*A.*), the subjects of this study, occupy the middle ground between small insects and birds where impacts can result in a non-fragmenting push or a splash[55], dependent upon the size of the two bodies and impact dynamics. Rain of various intensities, dripping from above leaves, and splashes from other impacts all generate drops that may strike a samara mid-flight. A typical impact sequence between a samara and a drop is pictured in **Fig.1.3**. To simulate the impact of raindrops on samaras, we levitate autorotating samaras in a wind tunnel and subject them to drop collisions as illustrated in **Fig.2.4**a. Our samaras have a mass $m_s = 25 - 40$ mg and total length, or span, $S = 27 - 48$ mm. Drops toward the larger end of the raindrop spectrum were chosen for this study because they can transfer more momentum and wetting mass than smaller drops, thereby presenting greater in-flight perturbations. Our drops have a representative mass of $m_d = 31$ mg and diameter $D = 3.88$ mm and are categorized as "large" raindrops[57]. The experimental velocity of $U + V = 433 \pm 40$ cm/s reflects both the measured speed of drops released $\sim$1 m above the wind tunnel, $U = 349 \pm 25$ cm/s, and tunnel windspeed. This corrected impact velocity falls within the range of natural raindrop speeds[57] while providing drops that can be aimed at levitating samaras. We plot non-dimensional length S/D to mass m/m_d for samaras and similarly sized flyers from literature[58] in **Fig.2.4**c, by fixing $m_d = 32$ mg, $U = 500$ cm/s, and $D = 3.88$ mm. The boundaries between splashing, coating, and pushing impacts are provided by Dickerson *et* al(2014)[55]. In a pushing impact, the drop and object move together, while in a splashing impact, the drop separates upon contact with the object. In a coating impact, the drop primarily covers a portion or the entirety of the object's surface. The model predicts that samaras in this study are more likely to fragment raindrops than to leave them intact. The boundaries between impact regimes assume impacts such that the center of gravity of the drop and target are aligned. Misalignment between the center of gravity of the drop and the samara promotes a"pushing" interaction by lengthening the timescale of the initial collision and reducing the force imparted to the drop. Of course, a myriad of different impact behaviors manifests for plant material[59–61] and insects[62] not in flight.

Crosswind effects on samara flight

Wind, often regarded as a nuisance on an otherwise pleasant day, offers a vital dispersal mechanism for seeds adapted to aerial transport. Morphological structures such as wings, plumes, or membranes allow seeds to harness aerodynamic forces, slowing their descent and increasing horizontal displacement through the atmosphere[63,64]. The extent of dispersal is governed by a falling time and the rate of lateral transport. In particular, turbulent updrafts and shear layers in the canopy can significantly enhance vertical lift and transport poten-

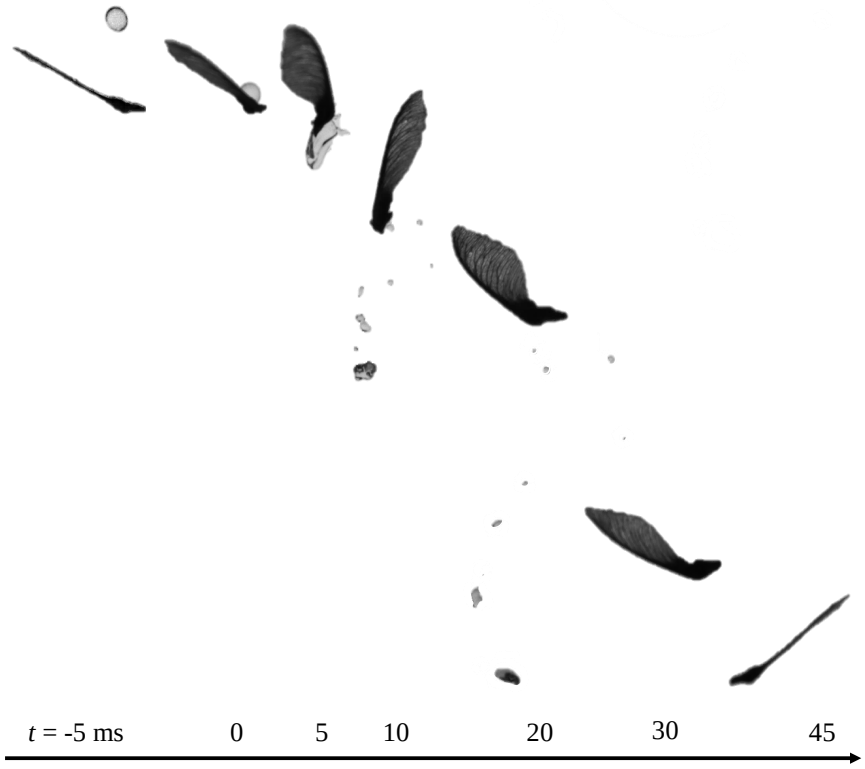

Figure 1.3: Image sequence of a *A. ginnala* impacted by a simulated raindrop, lasting 45 ms. Raindrops momentarily disrupt stable autorotation, which is recovered after the samara separates from the drop.

tial[9,65]. Exposure to crosswinds further modifies seed trajectories, with outcomes ranging from destabilization to enhanced lift, depending on the geometry of the seed and its mode of descent[37,66].

Among wind-dispersed seeds, samaras represent a class of diaspores that achieve extended aerial times through autorotation. Characterized by a single-winged structure extending from the seed, samaras passively generate lift by precessing as they fall. Autorotational motion stabilizes descent and reduces terminal velocity by converting vertical motion into rotational kinetic energy, allowing the seed to glide away from the parent plant. The aerodynamic behavior of samaras depends strongly on their geometry, including wing shape, wing curvature, mass distribution, and angle of attack during descent[67,68]. While most studies have focused on autorotating *Acer* samaras, which exhibit a stable helical descent, some species employ a rolling mode of descent, spinning along their spanwise axis while also precessing like a helicopter blade. Such rolling dynamics may offer aerodynamic advantages in turbulent or crosswind conditions by stabilizing orientation, sustaining lift under fluctuating flow, and exploiting lateral gusts to enhance dispersal range, highlighting their potential role as an adaptive strategy warranting further investigation.

Figure 1.4: Time-resolved image sequences showing descent trajectories of *F. Americana* samaras under increasing crosswind speed. Each trace captures a stacked sequence of images extracted from high-speed video at 0.001-ms time intervals, illustrating spanwise rotation, precession, and lateral drift. From left to right: $U = 0$, 1, 3, 5 m/s.

Prior studies on *Acer* samaras show how crosswind exposure influences descent dynamics[37,67]. When subjected to concentrated lateral gusts, autorotating samaras exhibit one of two characteristic behaviors. In the dropout mode[14], the seed ceases rotation and descends rapidly. In floating mode[14] autorotation continues during lateral displacement. The expression of each mode is predicted by the dimensionless ratio of crosswind speed to the rotational tip velocity of the samara. Kinematic tracking shows that stall events are often marked by a sudden cessation of rotation, occasionally followed by a reversal in rotation direction[14]. In the face of disturbances, *Acer* samaras are very capable of quickly recovering autorotation[14,15,37,67].

In contrast to *Acer* samaras, rolling samaras descend while spinning rapidly about their spanwise axis, generating lift through periodic fluctuations in angle of attack as broad wing

surfaces cyclically encounter the oncoming airflow[33,69]. Like *Acer* samaras, rolling samaras descend on a helical path but exhibit more complex dynamics; their tips exhibit small-amplitude oscillations superimposed on their dominant precession[69]. Lift arises from a combination of asymmetric flow separation and rotationally induced pressure gradients, consistent with mechanisms identified for unsteady falling and rotating plates[35,70]. Despite extensive study of autorotating samaras, responses of rolling samaras to lateral wind disturbances remain underexplored. Rolling introduces a second rotational axis and engages with cross-flow in ways distinct from autorotating counterparts[33], as shown in **Fig.1.4** Understanding behavior in crosswind is essential for a broader aerodynamic framework for seed dispersal and may reveal strategies for passive stability and drift across canopy environments[9,66].

Continuous spiral tumbling in falling paper and rolling samaras

Seed dispersal in plants relies on passive aerodynamic mechanisms that prolong time aloft and enhance transport distances[9,71,72]. Winged seeds exploit autorotation to generate lift with minimal energetic input, achieving efficient and stable descent[73]. Classical work on wind-dispersed diaspores distinguishes parachuting by pappi from winged-seed modes of gliding, rocking, and autorotation, with planform and center-of-gravity location strongly shaping both mode and descent rate[74].

Maple samaras (*Acer* spp.) provide a canonical example of single-axis helical autorotation with a relatively steady angle of attack[73]. Other species, including ash (*Fraxinus* spp.) and tulip poplar (*Liriodendron tulipifera*), display a dual-axis descent that combines spanwise rolling with azimuthal precession, forming a coupled helical path known as continuous spiral tumbling[33,41]. Variation in wing thickness and aspect ratio produces repeatable differences in the size and tightness of the helical path, while maintaining consistent descent periodicity and directional stability as shown in **Fig.1.5**. The same coupled motion occurs across a range of plate geometries that mimic samara morphology, revealing a shared aerodynamic mechanism that links natural and synthetic flyers[24,41].

Connections between samaras and freely falling plates motivate the use of simplified analogues. At intermediate Reynolds numbers, falling plates organize into regimes of steady descent, flutter, tumble, autorotation, and mixed motion, which are largely determined by the Reynolds number Re and a dimensionless moment of inertia I^*[35,75–77]. Experiments by Varshney *et al.*[24] demonstrated that thin parallelogram plates naturally enter a helical descent mode that couples tumbling and precession through aerodynamic torque balance. The motion persists across aspect ratios and densities, suggesting that aerodynamic lift is sustained through coupled rotation and translation rather than through instantaneous angle of attack. The robustness of the cone angle and helical geometry highlight the stability of

continuous spiral tumbling as a self-organized aerodynamic state.

The role of mass distribution adds an additional layer of control to these dynamics. Shifting the center of mass along the chord modifies flight behavior across a continuum from fluttering and tumbling to gliding and diving[78]. Quasi-steady modeling and experiments by Li *et al.*[78] show that changes in center-of-mass position alter aerodynamic torque balance and stability through modified pitch and moment coupling, creating transitions between steady and unsteady descent. Subtle morphological adjustments therefore reorganize flow structure and stability through coupled force and torque interactions.

The present study employs flat parallelogram plates as controlled analogues for rolling samaras to identify the aerodynamic principles that govern continuous spiral tumbling. By systematically varying aspect ratio, thickness, and geometric scale, the resulting trajectories are mapped within dimensionless regimes, and the corresponding descent velocity, coning angle, rolling and precessional frequencies, and precessional radius are quantified. The analysis extends biological observations of rolling samaras to engineered analogues, providing a unified aerodynamic and geometric framework for understanding the stability and structure of helical descent **Fig.1.5**.

1.3 Research Problem and Contributions

The aerodynamic performance of samaras has long fascinated biologists and engineers, yet key questions remain unanswered regarding the diversity of mechanisms that enable passive stability and dispersal. Maple (*Acer*) samaras are well known for their robust autorotation, but rolling samaras from ash and poplar species employ a more complex coupled motion of rolling and precession that remains poorly understood. Furthermore, both rolling and autorotating samaras encounter natural perturbations such as gusts and raindrops, yet the mechanisms of resilience and recovery have not been fully characterized. Addressing these gaps requires a systematic experimental framework that spans species, flight modes, and disturbance conditions.

The originality of this work lies in combining detailed morphological characterization with dynamic flight measurements across both autorotating and rolling samaras, while explicitly testing their robustness to environmental perturbations. For maple samaras, we measure the morphological and dynamic characteristics of eight species, quantify descent velocities and angular kinematics, and apply a classical aerodynamic drag model to demonstrate a unified scaling framework. For rolling samaras, we extend high-speed three-dimensional tracking to resolve trajectories, rolling and precessional velocities, and periodic modulation of angle of attack, uncovering wing thickness as a critical morphological driver of descent velocity.

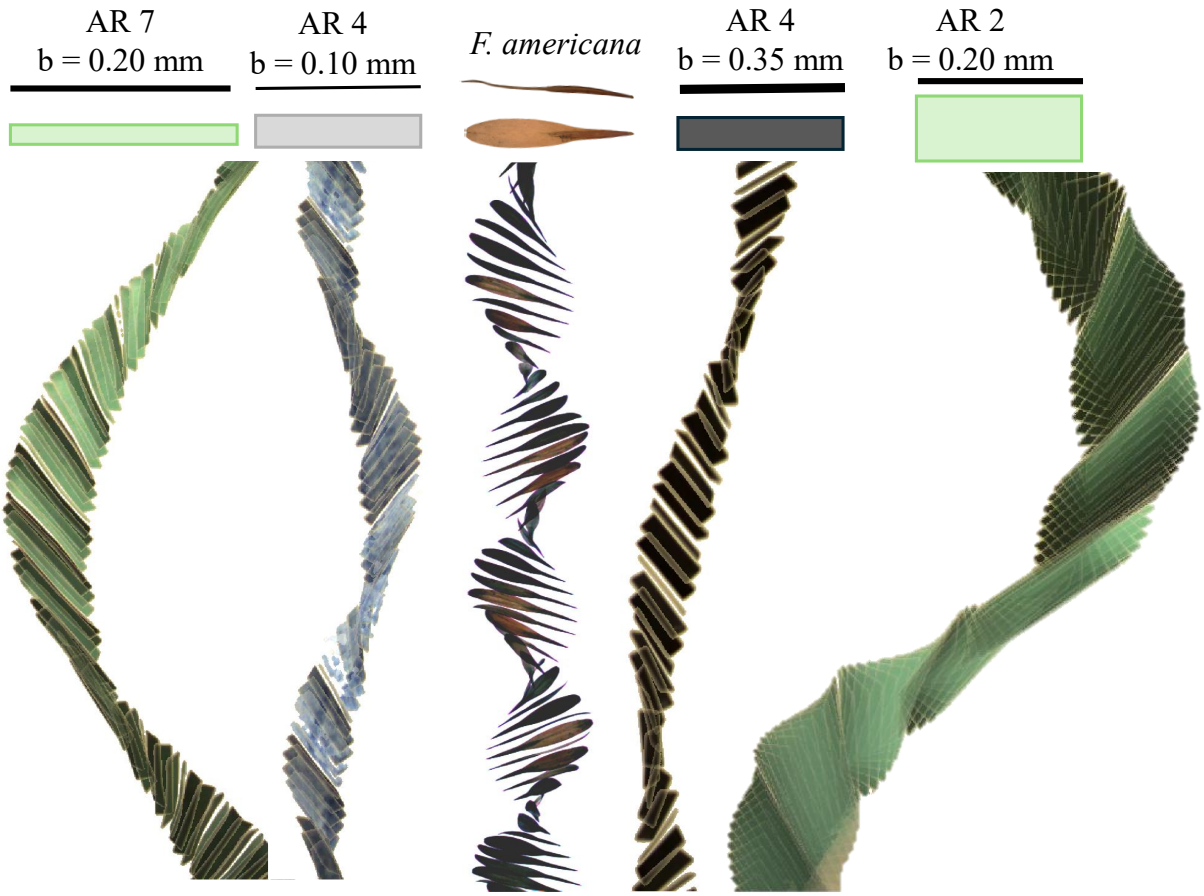

Figure 1.5: Representative helical centerlines of falling plates and a natural samara arranged by aspect ratio (AR) and thickness b in millimeters. Labels above each column give AR and b. Larger b or lower AR produce tighter, wider sweeps, whereas thinner sheets or higher AR yield looser trajectories. The *F. americana* panel provides a natural reference.

Beyond baseline kinematics, the study advances originality by introducing controlled perturbations. Autorotating samaras are subjected to added mass, wing ablation, and raindrop impacts to test the limits of their aerodynamic resilience, revealing compensatory mechanisms in rotation rate and coning angle that restore stable descent. Rolling samaras are released in crosswinds and tracked at $U = 1, 3, 5$ m s^{-1}, producing new insights into how lateral gusts alter trajectories, transport distances, and drag characteristics. Together, these approaches provide the first systematic comparison of resilience between autorotating and rolling samaras under both morphological and dynamic perturbations.

The central problem addressed in this dissertation is how morphology and unsteady aerodynamics govern the stability and dispersal performance of samaras under natural perturbations. Key questions include: (i) How do morphological traits such as span, chord, thickness, and nutlet mass regulate descent velocity and rotational dynamics? (ii) What aerodynamic mechanisms underlie the coupled rolling-precessional motion of ash and poplar samaras?

(iii) To what extent do samaras tolerate perturbations such as mass addition, wing damage, raindrop collisions, or lateral crosswinds, and by what mechanisms do they recover? By resolving these questions, the dissertation advances both ecological understanding of seed dispersal and the development of bio-inspired aerial systems that leverage passive stability.

1.4 Overview

Understanding the flight of wind-dispersed seeds offers both ecological and engineering value. Samaras, the winged seeds of maple, ash, and poplar, achieve remarkable stability and range without active control, relying solely on passive aerodynamic mechanisms. The success of these seeds raises broad questions about how morphology and motion interact to produce robust dispersal across varied environments.

The study is undertaken to explore how samaras maintain effective flight when subjected to natural perturbations such as crosswinds, turbulence, or raindrop impacts. Particular attention is given to differences between maple samaras, which descend through autorotation, and rolling samaras, which couple rolling and precession in dual-axis motion. By examining both morphological variation and environmental disturbance, the work seeks to identify the governing principles that enable resilience and efficiency in passive dispersal.

At a broader level, the questions addressed include: How do differences in geometry shape stability and performance? What mechanisms allow recovery when flight is disrupted? And in what ways can these natural solutions inform models of seed dispersal and inspire bio-inspired aerial technologies? The chapters that follow address these questions through a combination of experiments, analysis, and scaling frameworks.

Chapter 2
Methods

2.1 Dynamic Measurements and Filming

2.1.1 2D Vertical Wind-Tunnel Measurements

A schematic of our experimental flight setup is shown in **Fig.2.2**c. Two wind tunnels were constructed specifically for studying samara flight, with dimensions of 15 × 15 cm and 20 × 20 cm. The construction of two tunnels is essential to provide sufficient room for the larger seeds to fly without encountering the boundaries of the smaller tunnel. The larger wind tunnel accommodated *Acer Macrophyllum* and *Acer Negundo* specimens, in addition to accommodating samaras with added mass and reduced area. A 20.3-cm inline duct fan pushes air into the bottom of the tunnel by way of a flexible duct and through 2.5 cm of aramid honeycomb with a 3.2-mm cell diameter that laminarizes flow[79]. Fan speed is controlled by an ITECH IT-M7721 AC power supply. Wind speed V_{d} is measured by a Koselig KI-10001 anemometer with 0.01-m/s precision. A Photron NOVA S6 camera captures samara hovering at 2000 fps.

Samaras are released into wind tunnels by hand. Wind speed is adjusted to facilitate stable hovering such that samaras do not ascend or descend > 1 cm per 7 revolutions. The coning angle is determined by averaging three angle measurements taken during seven complete rotations. Angular velocity is determined by measuring the time taken for the samara seed to complete one rotation, and another, after seven subsequent rotations.

2.1.2 3D Multi-Camera Free-Fall Measurements

Samaras from three species—*Fraxinus* (*F.*) *americana* L., *F. excelsior* L., and *Liriodendron* (*L.*) *tulipifera* L.—are collected in Knoxville, TN, after natural dispersal. Only visually undamaged samaras are selected for measurement and experimentation. Representative examples of each test species are pictured in **Fig.2.1**a.

Samara mass m is measured using a Sartorius Secura 225D–1S analytical balance with a resolution of 0.0001 g before flight trials. Samara area A, span S, and chord c are measured from still images as described in Schaeffer *et* al(2024)[11]. Thickness T is measured at the point of maximum chord using a Mitutoyo caliper with 0.01 mm resolution.

Kinematic tracking of falling samaras is conducted using four high-speed video cameras, as

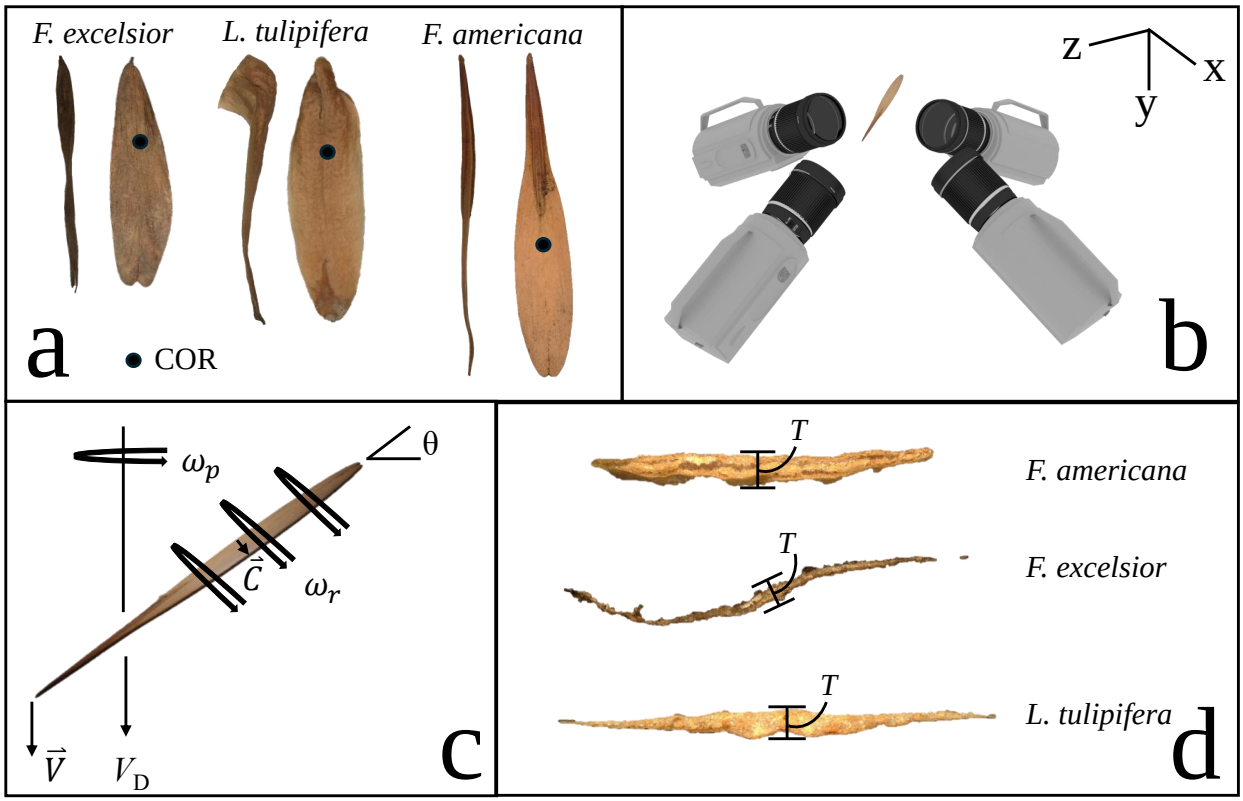

Figure 2.1: Overview of samara species and experimental setup. **(a)** Representative samaras from the three focal species: *F. Americana*, *F. excelsior*, and *L. tulipifera*. Black dots represent the approximate center-of-rotation. **(b)** Experimental setup for high-speed video tracking of falling samaras using four synchronized cameras. **(c)** Kinematic and dynamic flight variables analyzed in this study, including rotational velocity ω, coning angle θ, rolling velocity ϕ, and descent velocity V_d. **(d)** Cross-sectional views of samara seeds illustrating variations in thickness b.

illustrated in **Fig.2.1**b. The analysis of the video recordings was performed using DLTdv[80]. The extracted three-dimensional (3D) position data is used to compute kinematic parameters, including rotational velocity ω_p, coning angle θ, rolling velocity ω_r, and descent velocity V_d, using MATLAB. The measured values are summarized in **Fig.2.1**c.

To assess the impact of initial orientation on flight dynamics, samaras are held manually at specified orientations before being released into a wind tunnel, described in Schaeffer et al(2025)[15]. Airflow is adjusted to match stable levitation velocity, allowing for a controlled comparison of automation initiation times and trajectories.

2.1.3 Statistical Analysis

We employ the MATLAB box chart tool to visualize the experimental data distributions, including the minimum, maximum, average, and first and third quartiles. These values were

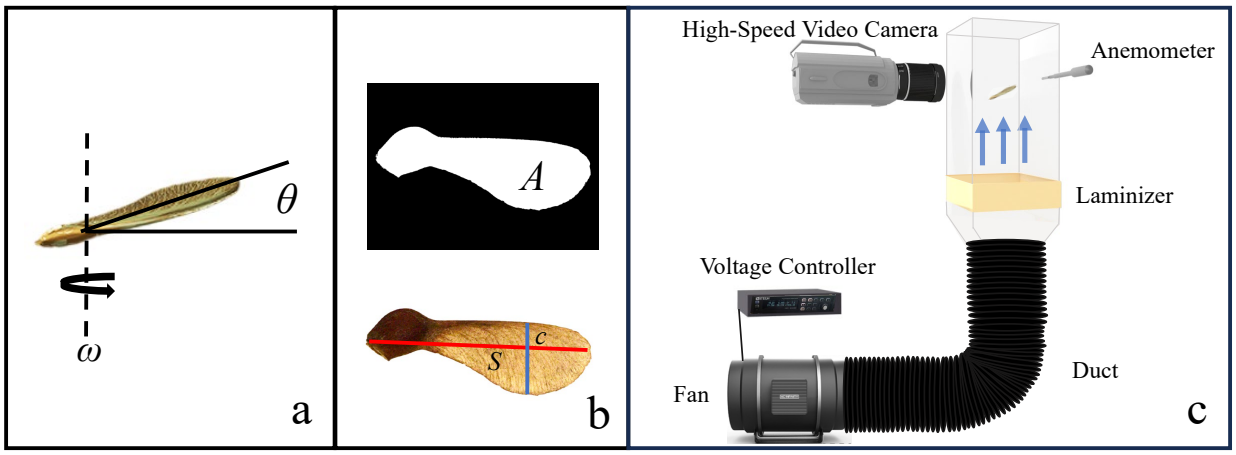

Figure 2.2: **(a)** Schematic of samara in flight with coning angle θ and angular velocity ω labeled.**(b)** Visual representation of area A, span S, and chord c taken from image analysis. **(c)** Experimental setup.

presented in the colored boxes of **Fig.3.2** and **Fig.3.4**. All wind tunnel trials are comprised of three replicates. All reported averages in tables and plots derived from wind tunnel experiments have standard deviations smaller than the marker size.

2.2 Falling Paper as Spiral Continuous Tumbling

All experiments were performed in still air within a closed laboratory to eliminate environmental disturbances. Flat, parallelogram-shaped cards were fabricated from white cardstock, with no internal angle between adjacent edges. Each plate had a defined span S, chord c, and thickness b. The cards were released with their spanwise edge oriented horizontally and dropped from a height of 2.5 m. Only trials exhibiting continuous spiral tumbling, characterized by stable periodic rolling and precession without chaotic or planar flutter, were retained for analysis.

Three geometric parameters were systematically varied, including aspect ratio $\lambda = S/c$, scale, and thickness. Aspect ratio values ranged from $\lambda = 1, 2, 4, 7$, and 10. Scale corresponded to proportional enlargement of all dimensions, with characteristic chord lengths of $c = 0.020$, 0.028, 0.040, 0.056, and 0.080 m for scales 1 through 5. Three plate thicknesses were tested, with $b = 0.10$, 0.20, and 0.36 mm, representing increasing paper density and stiffness. In total, 75 unique geometric configurations were fabricated and analyzed.

Motion was recorded using a high-speed camera operating at 240 frames per second, capturing the side view of each falling plate, as illustrated in **Fig.2.3**a. Four tracking markers were placed on each card, with two positioned at the endpoints of the span S and two po-

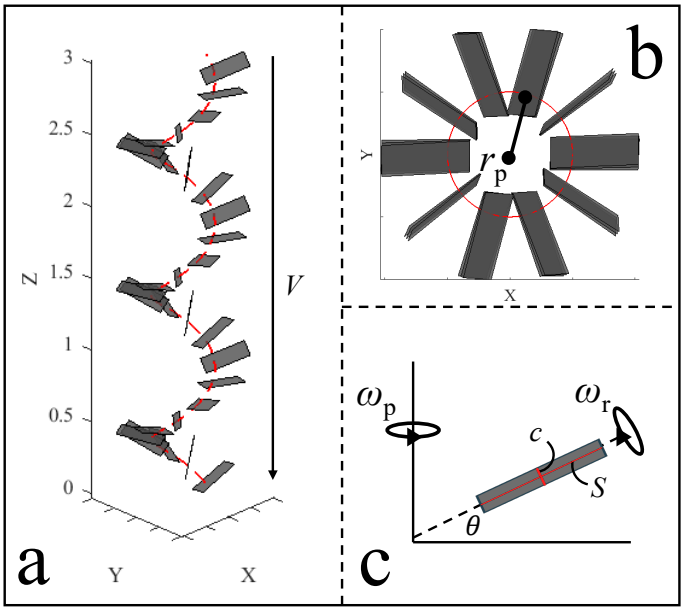

Figure 2.3: Schematic of the rolling–precessional descent mode. (**a**) Side view of a representative trajectory showing helical descent with vertical velocity V_d. (**b**) Top view illustrating precessional radius R_p and azimuthal rotation. (**c**) Definition of measured quantities: coning angle θ, precessional velocity ω_p, and rolling velocity ω_r. Span S and chord c define the geometry of the plate.

sitioned at the endpoints of the chord c. The tracked points were used to reconstruct both translational and rotational kinematics through custom MATLAB scripts.

From the tracked trajectories, we compute five key dynamic quantities: descent velocity V_d, coning angle θ, precessional velocity ω_p, rolling velocity ω_r, and precessional radius r_p. The precessional radius is defined as the mean lateral offset of the centroid of the plate relative to the vertical axis, shown in **Fig.2.3**b. The coning angle θ, rolling velocity ω_r, and precessional velocity ω_p were extracted from angular relationships between spanwise and chordwise markers, as depicted in **Fig.2.3**c.

2.3 Raindrop Impact Experiments

Samaras from three Acer species—*A. ginnala* Maxim., *A. floridanum* Chapm., and *A. negundo* L.—were collected underneath trees in Knoxville, TN, post-natural dispersal. Only visually undamaged samaras were selected for measurement and experimentation. Representative examples of each test species are pictured in **Fig.2.4**c. Samara mass m_s is measured using a Sartorius Secura 225D–1S analytical balance with 0.0001-g resolution before flight trials. Samara area A and span S, are measured from still images[11]. Advancing contact angles are measured by growing a drop on the samara wing and optically measuring the

angle with Tracker. Measurements across multiple regions of the wing revealed an isotropic, average contact angle of 115 ± 3°.

A vertical wind tunnel with a transparent test section 50-cm tall and 15×15 cm in cross-section allows for stable levitation of samaras in laboratory coordinate y, and is illustrated in **Fig.2.4**a. Airflow is generated by a 20-cm inline duct fan, controlled by an ITECH IT-M7721 AC power supply, passing through an aramid honeycomb to ensure laminar flow. Wind speed is measured with a Koselig KI-10001 anemometer with 1-cm/s precision. Two high-speed Photron NOVA S6 cameras, operating at 1000 fps and 90° opposed, capture samara position. Samaras are released into the wind tunnel by hand; wind speed is adjusted to facilitate stable hovering such that samaras ascend or descend < 1 cm per 7 revolutions. A needle with an outer diameter of 1.5 mm releases drops above autorotating samaras. The coning angle (θ) is measured continuously by aggregating both camera views using DLTdv[80].

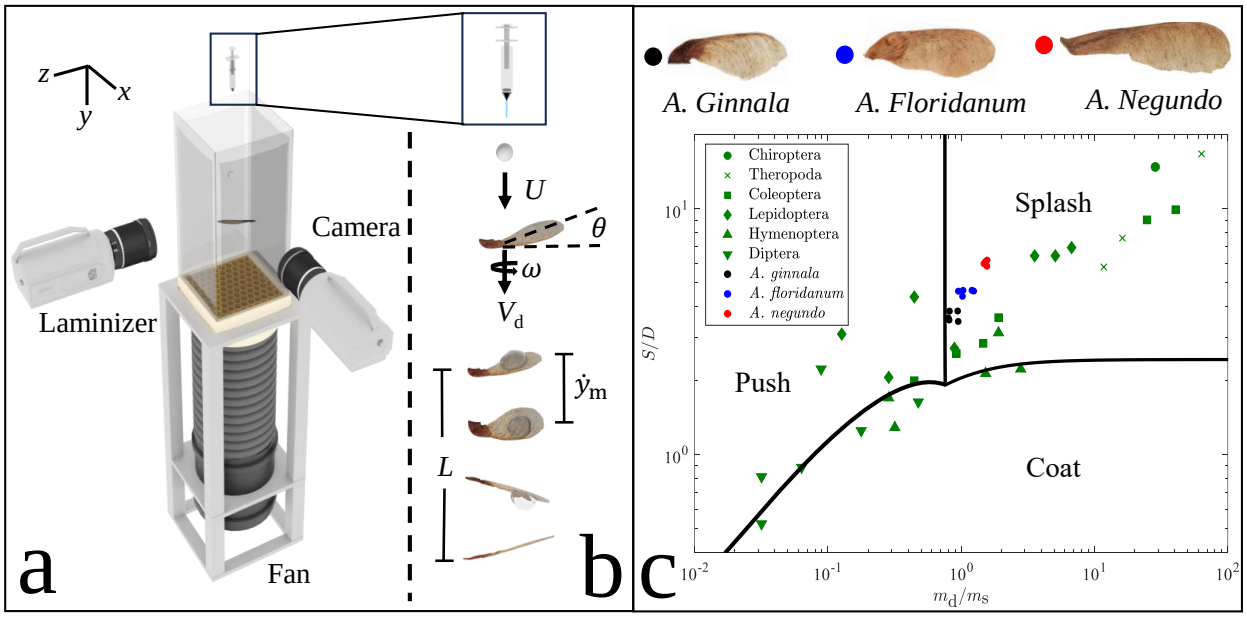

Figure 2.4: (a) Vertical wind tunnel. (b) Schematic of dynamic variables pertinent to impact. (c) The relationship between length ratio S/D and mass ratio m/m_d of insects[58] (green) and the samaras in this study. Boundaries between impact modes are drawn from theory[55].

2.4 Crosswind Jet Experiments

Samaras from three rolling species and one *Acer* species—*Fraxinus americana*, *Fraxinus excelsior*, *Liriodendron tulipifera*, and *A. ginnala*—are collected in Knoxville, TN following natural dispersal. Only undamaged specimens, as determined by visual inspection, are selected for measurement and testing. Samara mass m is measured using a Sartorius Secura

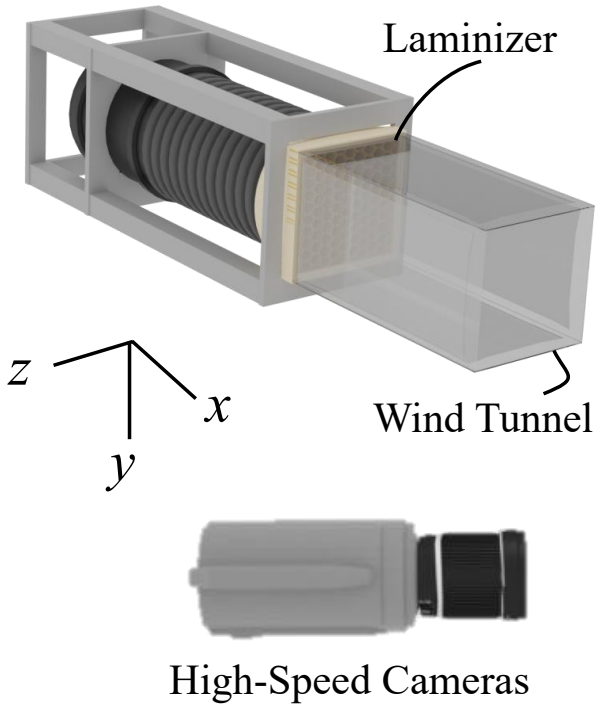

Figure 2.5: Schematic of the experimental setup used to study samara descent under crosswind. The setup includes a lateral wind tunnel with a laminizer to produce a steady crossflow, high-speed cameras to track the motion of samaras, and a clearly defined coordinate system with the z-axis aligned with gravity. Viewing areas are arranged to capture both lateral and vertical components of motion.

225D–1S analytical balance with a resolution of 0.0001 g prior to flight trials. Planform area A , span S, and chord length c are obtained from high-resolution still images following methods described in Schaeffer et al.[11]. Thickness b is measured at the location of greatest chord length using a Mitutoyo digital caliper (0.01 mm resolution).

Lateral crosswinds are created by the issuance of a free jet from a 10 cm $\times$ 10 cm acrylic channel. Air enters the channel through a honeycomb laminarizer, 1.27-cm thick and with 0.32-cm cells. Crosswind speed is controlled by a ITECH IT-M7721 AC power supply powering a 20-cm inline duct fan.

Fifteen samaras—five from each species—are tested. Each specimen is released in still air from approximately 0.5 m above the acrylic channel. Three wind speeds are tested: 1 m/s, 3 m/s, and 5 m/s. For each specimen, three trials are conducted per speed setting. The full test volume has a height of approximately 2 m, with a $\sim$0.5 m drop height before crosswind entry and approximately 1.4 m for post-crosswind recovery. All samaras recovered autorotation and vertical descent within this recovery distance.

Flights are filmed with two cameras. A Photon Nova S6 high-speed camera at 1000 fps

is positioned perpendicular to the acrylic channel to capture high-resolution motion of the samara before, during, and after entry into the crosswind jet. A secondary camera, an iPhone operating in 240 fps slo-mo mode, recorded the full descent trajectory from release to final recovery beyond the viewing window of the Nova S6. While lower in frame rate, this camera provides a view of the complete flight path. Videos are analyzed in MATLAB.

Chapter 3
Kinematics and Morphological Scaling Relationships

3.1 Maple samara flight is united by a classic drag model

Maple samaras exhibit remarkable aerodynamic consistency despite substantial variation in shape and scale. Stable autorotation, steady descent, and comparable terminal velocities are observed across species. While many models have been proposed to explain samara descent, a unifying framework has remained difficult to establish due to the complex coupling between lift, drag, rotation, and morphology. The following chapter evaluates whether a classical drag-based force balance can describe the descent behavior of maple samaras. Dynamic and morphological data from nine species are used to examine how descent velocity scales with wing loading and projected area. A single effective drag term, combining both form drag and lift, emerges as a powerful predictor of flight performance. The model reveals strong interspecific agreement, while also identifying species with unexpectedly high or low aerodynamic resistance relative to their mass. Those deviations, not evident from dynamic variables alone, become clear when samaras are treated as falling blunt bodies governed by simple aerodynamic scaling.

3.1.1 Aerodynamic drag unifies maple samara species

We begin exploring the slow descent of samaras by filming hovering, stably autorotating samples in a wind tunnel, and measuring the dynamic quantities recorded in **Fig.3.2**. We find our samaras have an average terminal velocity $V_{\mathrm{d}} = 0.83 \pm 0.08$ m/s, values which appear to have no apparent correlation with coning angle $\theta = 117.8 \pm 29.1°$, or angular velocity $\omega = 18.8 \pm 4.6$ [rad/s] (see **Fig.A.2**). The angle of attack varies by wing location and thus is tabulated at $0.75S$ from the nutlet tip such that $\phi = \arctan(V_d/0.75S\omega) = 42.5 \pm 3.2°$, and is nicely schematized by Lentink *et al.* (2009)[81]. Included as supplementary plots in **Fig.A.2**-**Fig.A.4**, our exploration of isolated dynamic variable relationships did not reveal any notable correlations. Instead, considering dynamic variables in functional groups is more fruitful.

At its core, the idea of 'wing loading' as plotted in **Fig.3.1** is an expression of aerodynamic drag by considering the samara a free-falling blunt body. In fact, the form drag and lift

generated by an autorotating samara act against the direction of motion. We, therefore, lump the two effects into a simple force $F_D = \rho V_d^2 A \cos\theta$. From a vertical force balance, one would expect

$$mg \sim \frac{1}{2} C_D \rho V_d^2 A \cos\theta, \tag{3.1}$$

where $g = 9.81$ m/s^2 is the acceleration due to gravity, C_D is a drag coefficient, $\rho = 1.23$ g/cm^3 is the air density, and $A\cos\theta$ is the projected area of the seed in the direction of motion (**Fig.2.1**c). This approach is similar to the descent factor proposed by Lentink *et al.* (2009)[81]. We plot $\rho V_d^2 A \cos\theta$ versus seed weight mg for all tested samaras in **Fig.3.3**a. Each data point in **Fig.3.3** is comprised of three replicates. The slope of the line of best fit in **Fig.3.3**a, with a correlation coefficient $R^2 = 0.72$, indicates $C_D = 5.99$ across all test species. A unifying drag coefficient allows for the comparison of individual seed performance to the bulk and lumping dynamic variables as done in **Fig.3.3**a supplies a superior correlation between descent and weight than the wing loading of **Fig.3.1** ($R^2 = 0.35$). Lentink *et al.* (2009)[81] also combined the drag and lift forces in the vertical direction through a descent factor. Here, we add the coning angle θ which incorporates the effective lift force in the vertical direction. This important distinction will be shown in Section 4.1.2 to scale all samaras better as it connects the lift force to ω, V_d, and mg.

Emerging from the drag plot of **Fig.3.3**a are two species that notably depart from the

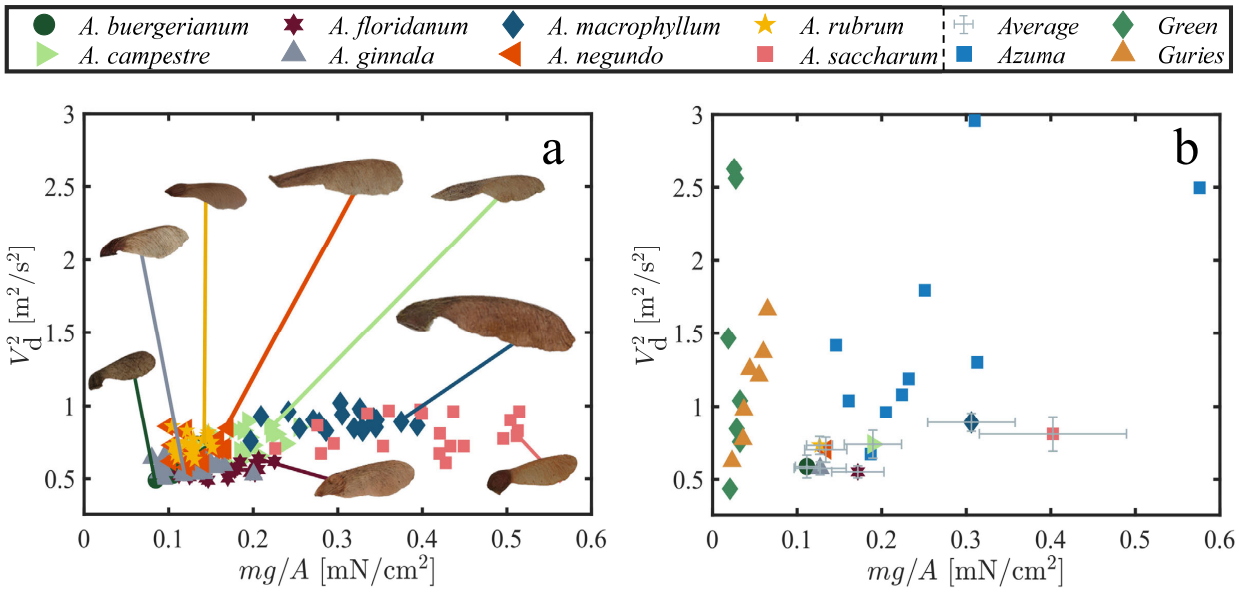

Figure 3.1: Relation between descent velocity V_d and wing loading mg/A from **(a)** this study, and (b) previous studies [Azuma and Yasuda (1989)[31], Green (1980)[27], Guries et al(1984)[8]] with matched axis scales for comparison. Points in (b) with error bars are averages of species taken in this study. Error bars represent one standard deviation.

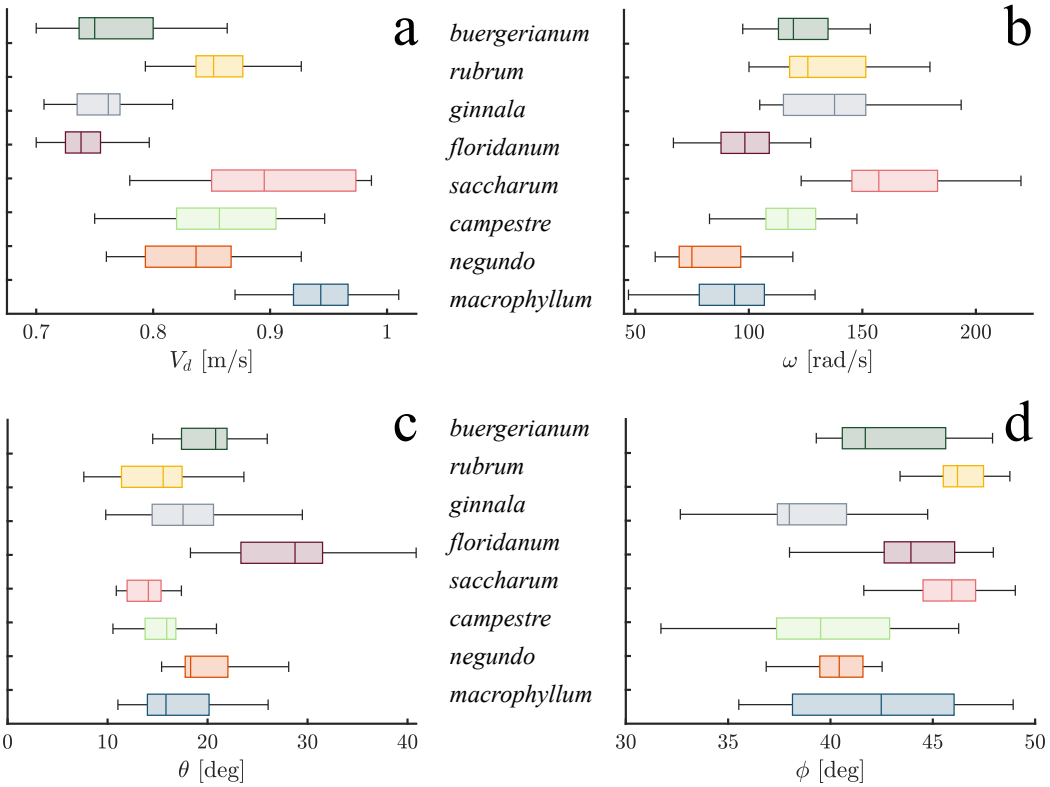

Species	V_d [m/s]	θ [deg]	ω [rad/s]	ϕ [deg]
A. buergerianum	0.77 ± 0.05	20 ± 3	122.3 ± 15.1	42.4 ± 3.3
A. rubrum	0.86 ± 0.04	15 ± 4	136.0 ± 24.1	40.3 ± 1.2
A. ginnala	0.76 ± 0.03	28 ± 6	137.6 ± 23.7	39.9 ± 3.2
A. floridanum	0.74 ± 0.03	28 ± 6	97.9 ± 15.6	45.8 ± 1.6
A. saccharum	0.90 ± 0.07	14 ± 2	154.1 ± 16.9	43.9 ± 2.0
A. campestre	0.86 ± 0.06	16 ± 3	117.6 ± 16.6	38.7 ± 2.6
A. negundo	0.84 ± 0.05	20 ± 4	81.8 ± 17.4	46.4 ± 1.2
A. macrophyllum	0.94 ± 0.03	17 ± 4	95.2 ± 9.9	42.7 ± 2.3

Figure 3.2: Dynamic measurements of test species: **(a)** descent velocity V_d, **(b)** angular velocity ω, and **(c)** coning angle θ. The table contains dynamic measurement averages and standard deviations. N = 20 for each species.

trend line. *A. Negundo* samaras have greater drag than might be expected for their weight, a possible consequence of mass distribution across a long, flat body (**Fig.1.1**). We deem *A. Negundo* samaras to be 'underweighted' in this context. *A. Saccharum* samaras fall more quickly than expected for their weight, or are 'overweighted', a likely consequence of their bulbous seed mass (**Fig.1.1**). The concepts of over- and underweighted do not materialize from tabulated dynamic measurements (**Fig.3.2**), but do from simple morphological measurements presented in Section 3.2.

The consideration of samaras as falling blunt bodies fails to capture the rotational dynamics occurring in the plane normal to descent. The autorotation of samaras is a direct result of the air momentum passing over the wings[13], to produce a centrifugal force about the samara centroid. Such rotation increases the aforementioned C_{D}, thus slowing the samara V_{d}. Therefore, the expected relation between descent and rotation is not abundantly clear[82], and samara rotation is underexplored in literature. Previous studies[13,31] analyzed rotational velocity within species, but lacked correlations across different species. We explore descent and rotation by plotting their respective associated forces in **Fig.3.3**b. It should be noted that we do not expect the relation between drag force and centrifugal force to be linear, but the slope of the line of best fit, 5.3×10^{-3} ($\mathrm{R}^2 = 0.58$), in **Fig.3.3**b provides a metric to compare the magnitude of the forces acting on the samara centroid. Centrifugal forces dominate those acting at the centroid. Underweighted seeds convert relatively less momentum from the passing air to angular momentum than overweighted seeds.

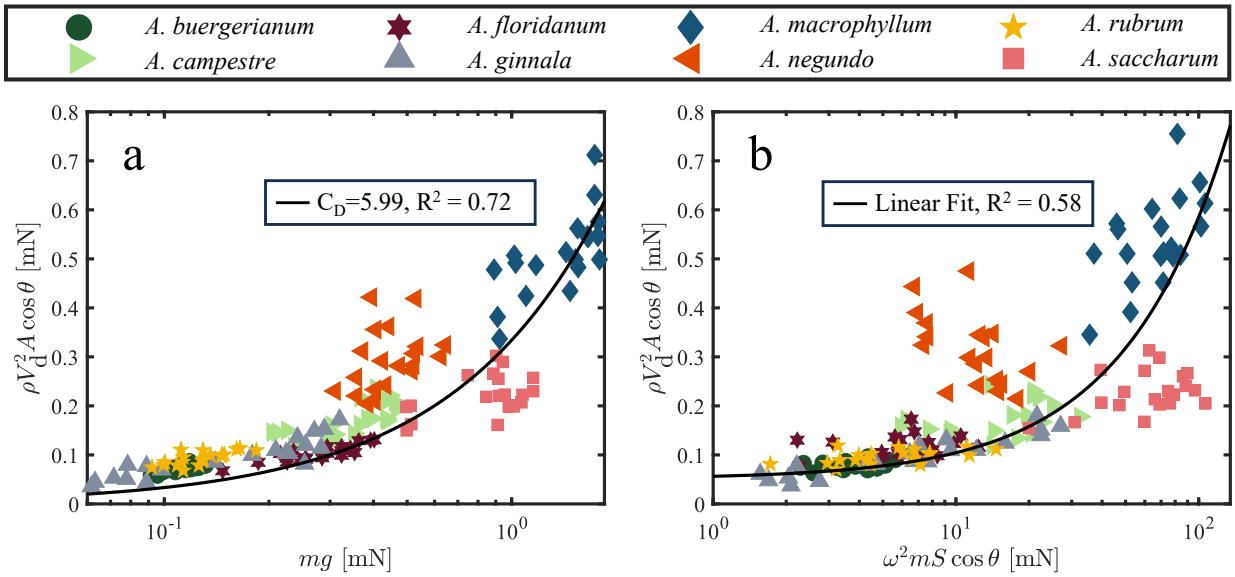

Figure 3.3: Salient forces acting on centroid during descent. **(a)** Drag force to samara weight mg and **(b)** drag force to centrifugal force.

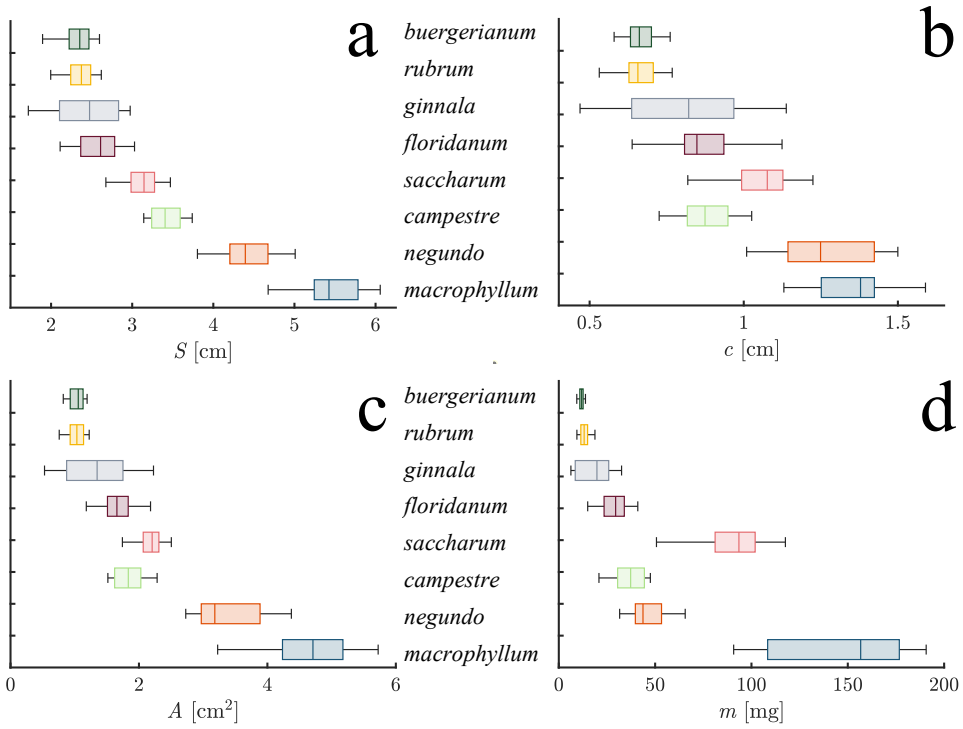

Species	S [cm]	c [cm]	A [cm^2]	m [mg]
A. buergerianum	2.33 ± 0.19	0.67 ± 0.05	1.04 ± 0.11	11.7 ± 1.3
A. rubrum	2.35 ± 0.18	0.66 ± 0.06	1.03 ± 0.14	13.3 ± 2.5
A. ginnala	2.44 ± 0.40	0.81 ± 0.20	1.32 ± 0.50	17.9 ± 9.2
A. floridanum	2.57 ± 0.27	0.87 ± 0.11	1.65 ± 0.26	29.0 ± 7.0
A. saccharum	3.12 ± 0.23	1.07 ± 0.10	2.16 ± 0.22	89.1 ± 21.6
A. campestre	3.42 ± 0.20	0.88 ± 0.08	1.84 ± 0.22	35.9 ± 8.8
A. negundo	4.41 ± 0.34	1.27 ± 0.16	3.42 ± 0.55	46.2 ± 9.2
A. macrophyllum	5.47 ± 0.35	1.35 ± 0.13	4.64 ± 0.67	145.6 ± 34.8

Figure 3.4: Morphological measurements for tests species: **(a)** span S, **(b)** chord c, **(c)** area A, and **(d)** mass m. The table values are averages and standard deviations. N = 20 for each species.

3.2 Samara morphology distinguishes species

In this section, we explore the drag and centrifugal force trends described in Section 3.1.1 by considering simple morphological measurements and their respective relationships.

3.2.1 Samara morphology is diverse

It is a wonder that samaras within and across species descend with such similar speeds despite their large variation in shape, scale, and proportion (**Fig.1.1**). Such a variation likely contributes to researchers' struggle to succinctly characterize samara mechanics. Our specimens range in mass $m = 6.3 - 19.1$ mg, span $S = 17.2 - 60.6$ mm, and area $A =$

$0.53 - 5.72$ cm^2, as recorded in **Fig.3.4**. *A. saccharum* and *A. buergerianum* possesses sizeable, quasi-spherical nutlets, whereas *A. negundo* and *A. campestre* are equipped with elongated, flat nutlets. *A. macrophyllum* showcases trichomes adorning the nutlet area, while *A. ginnala* nutlets culminate in a distinct, sharp, flat edge. Samara wings likewise have broad variations in both aspect ratios, curvature, and texture. We measure the chord-span ratios of the triangular wings of *A. ginnala* and the rectangular wings of *A. floridanum* to be 0.33 and 0.34 respectively. By comparison, the slender wings of *A. campestre* have a chord-span ratio of 0.25. Wing proportions govern lift production and the mass moment of inertia, and will have an influence on agility[82–84].

We arrange the order of species in **Fig.3.4** according to **Fig.1.1**, that of increasing span. Intraspecific variability is rampant in *Acer* samaras can be attributed to genetic diversity, environmental influences, selective pressures acting on populations, or the position of the seed within the tree canopy[85–88]. Notable intraspecific variation includes the chord and span of *A. Ginnala* with the smallest measured specimen achieving 41% the chord and 58% the span of the largest *A. Ginnala* specimen, as shown in **Fig.3.4**a,b, respectively. *A. Macrophyllum* has the largest intraspecific variation in mass, with the smallest specimen weighing just 48% that of the largest, as shown in **Fig.3.4**d. While tabulated values of morphological measurements are useful for assessing variation, the relation between physical dimensions is difficult to ascertain.

3.2.2 Samaras are two-dimensionally allometric

Within and across allometric species $A \sim L^2$ and $m \sim L^3$, where L is some characteristic length. Here we take the characteristic length of a samara to be its span S and likewise assume the other dominant length $c \sim S$. In this scenario, the chord is an alternative characteristic length scale. To satisfy allometry, it thus follows that

$$A \sim m^{2/3} \sim S^2 \sim c^2 \sim cS. \tag{3.2}$$

We explore the allometric predictions in Eq. (3.2) in **Fig.3.5**, and report our results in turn. We plot A versus m with a best-fit power law in **Fig.3.5**a. The allometric prediction yields a correlation coefficient $\mathrm{R}^2 = 0.69$. A best fit scaling for all our specimens, $A \sim m^{0.52}$, $\mathrm{R}^2 = 0.73$, a significant departure from Eq. (3.2). However, if we had not included *A. Negundo* and *A. Saccharum* in our study, our best fit would yield $A \sim m^{0.57}$. The origins of the underweighted (*A. Negundo*) and overweighted (*A. Saccharum*) species become apparent from **Fig.3.5**a, a classification that is difficult to ascertain from traditional treatment by wing loading of samaras (**Fig.3.1**). The mass-to-area ratios of **Fig.3.5**a suggest that

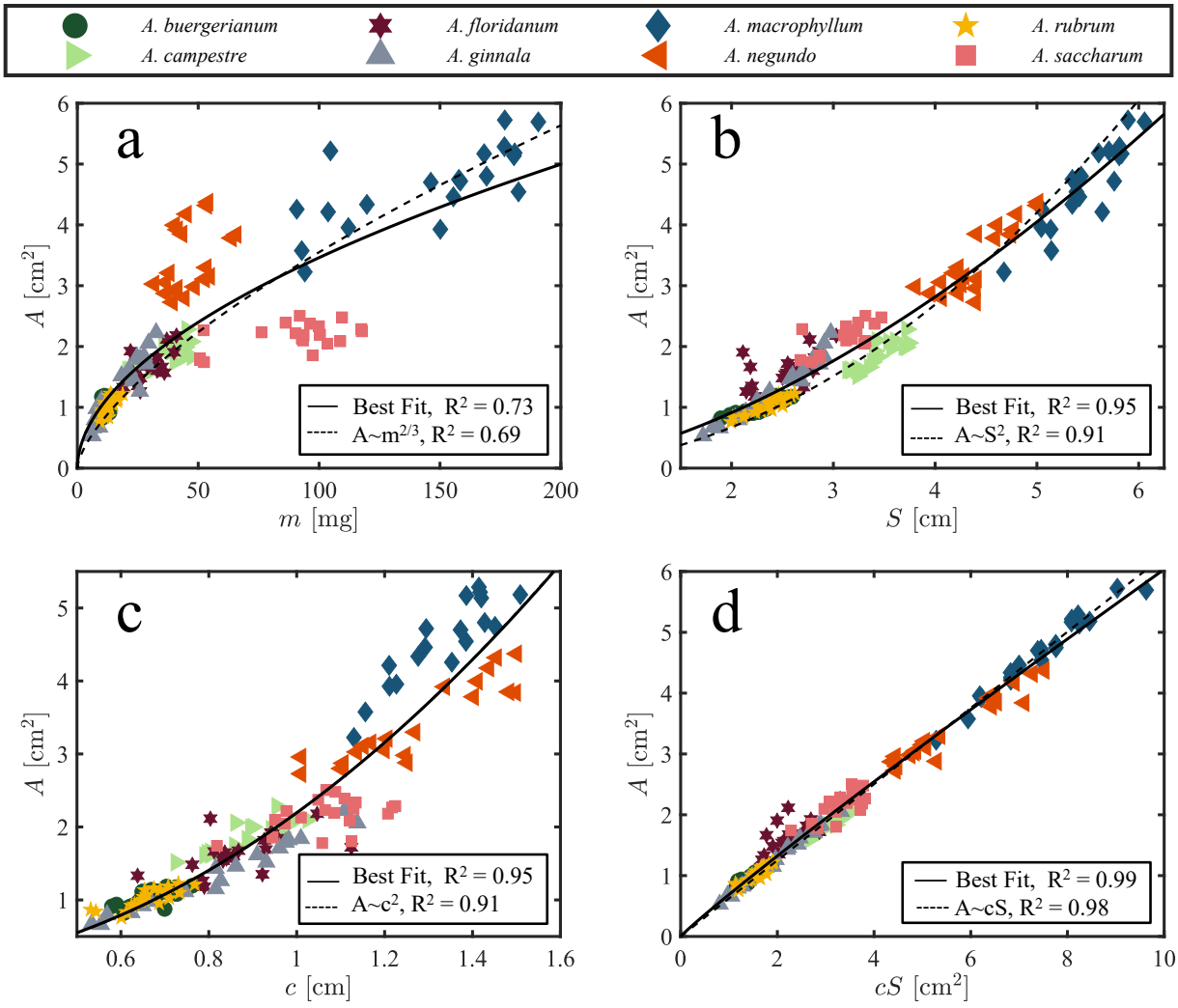

Figure 3.5: Allometric relations: **(a)** area A vs mass m, **(b)** A vs the square of span S^2, **(c)** A vs the square of chord c^2, and **(d)** A vs cS.

A. Saccharum samaras are naturally closer to the limit of mass they can support than are *A. Negundo* samaras, a hypothesis we test in Section 4.1.

Deviation from interspecific allometric predictions by *A. Negundo* and *A. Saccharum* appears to be caused only by nutlet mass. Otherwise, all our tested species are wonderfully allometric. We plot A versus S in **Fig.3.5**b, yielding a best-fit scaling of $A \sim S^{1.63}$, accompanied by a correlation coefficient of $R^2 = 0.95$ and a modest improvement over the predicted scaling correlation coefficient, $R^2 = 0.91$. The plot of A versus S supports span as an appropriate characteristic length scale. However, the best-fit power law of $A \sim c^{1.99}$, $R^2 = 0.95$ is remarkably close to Eq. (3.2), and is plotted in 3.5c. The allometric prediction yields a correlation coefficient of $R^2 = 0.91$. Chord is thus the single best length to characterize samara size. Lastly, the plot of A against cS exhibits a best-fit scaling of $A \sim cS^{0.94}$, yielding an exceptional correlation coefficient of $R^2 = 0.99$ 3.5d. While the A versus m plots distinctly differentiate between overweighted and underweighted seeds, the other allometric plots fail to showcase these distinctions explicitly. Within these plots, both *Acer Saccharum* and *Acer Negundo* demonstrate geometric correlations that align with allometric predictions.

While samaras do exhibit allometric relationships, deviations and interspecific variations in these relationships highlight the robustness, or perhaps lack of fine-tuning in their adaptations. Deviations from allometric predictions, particularly stemming from the mass-to-area relationship as illustrated in **Fig.3.5**a, underscore the uniqueness of each species' evolutionary trajectory. Key questions arise: How do external alterations in mass and area provided by environmental challenges influence individual seeds and their aerodynamic behavior? Does a simple drag model capture the behavior of modified samaras?

3.3 Precession and morphology of rolling samaras

We examine the morphology and descent kinematics of 30 rolling samaras, 10 each from three species: *F. americana*, *F. excelsior*, and *L. tulipifera*, with 3 replicate flights of each specimen. The samaras of this study roll about their span axis as they helically process downward. Such a precession is very similar to that of non-rolling samaras[11]. When released, samaras begin to roll before the onset of precession. The stochastic roll direction sets the direction of precession, clockwise or counterclockwise. Our tulip and ash samaras always roll such that the bottom chordal edge rolls forward, similar to a fluttering, translating plate[38], as schematized in **Fig.2.1**c.

Table 3.1: Summary of rolling samara kinematics and morphology. Each species includes $N = 10$ individuals, for a total of 30 samples. The final row reports mean values across all species.

Species	b (mm)	m (mg)	A (cm^2)	V_d (cm/s)	ω_r (rad/s)	ω_p (rad/s)
F.americana	0.50 ± 0.02	39 ± 3	1.9 ± 0.1	131 ± 9	443 ± 60	80 ± 7
F.excelsior	0.41 ± 0.02	60 ± 10	1.8 ± 0.1	191 ± 21	618 ± 77	119 ± 13
L.tulipifera	0.46 ± 0.02	47 ± 5	2.1 ± 0.2	148 ± 15	504 ± 66	94 ± 17
Mean	0.46 ± 0.03	50.4 ± 8.5	1.88 ± 0.21	158 ± 23	521 ± 96	97 ± 18

3.3.1 Samaras roll without wobble

To characterize descent behavior, we track the positions of four key points on rolling samaras: the seed tip, wingtip, left chordal edge, and right chordal edge. The 3D trajectories of representative samaras from each species are shown in **Fig.3.6**a. Once initiated, the rolling direction dictates the direction of precession. The roll propels the samara forward[38], but the seed is more massive and generates less propulsive force than the wing. The result is a circular rotation rather than the linear translation exhibited by symmetric plates. When the seed is removed, rolling and precession still occur, but the radius of precession increases, indicating that the center of aerodynamic rotation shifts further outward in the absence of the mass asymmetry. Findings from maple seed analog models similarly show that minor shifts in mass distribution can dramatically alter the descent trajectory from circular to compound paths[89].

Despite qualitatively similar descent dynamics across our three test species, morphological variation is stark. The heaviest species we test has the smallest wing area. Plan and side view photos are shown in **Fig.2.1**a while mass and area measurements are tabulated in Table 3.1. Broad morphological variation drives significant differences in descent velocity V_d, precession angular velocity ω_p, and rolling angular velocity ω_r, tabulated in Table 3.1. Rolling and precession angular velocities are tightly coupled, however, with an average across all trials of 5.2 ± 1.1 rad/s, number of trials $N = 90$.

Tabular values can be compared graphically by temporal representations of position. We plot lateral displacement of the tracked points in x versus time as shown in **Fig.3.6**b. The amplitude and frequency of oscillations in x are influenced by the span of the samara, with the relative rapidity in the rotation of *F. excelsior* being cursorily explained by its stubbiness compared to the other two species. Lateral displacement of the seed tip indicates a center-of-rotation (COR) located closer to the wingtip. We estimate COR locations from videos and provide labels in **Fig.2.1**a. Among the studied species, the COR in *F. americana* is located nearer mid-span, while *F. excelsior* and *L. tulipifera* have a COR is closer to the

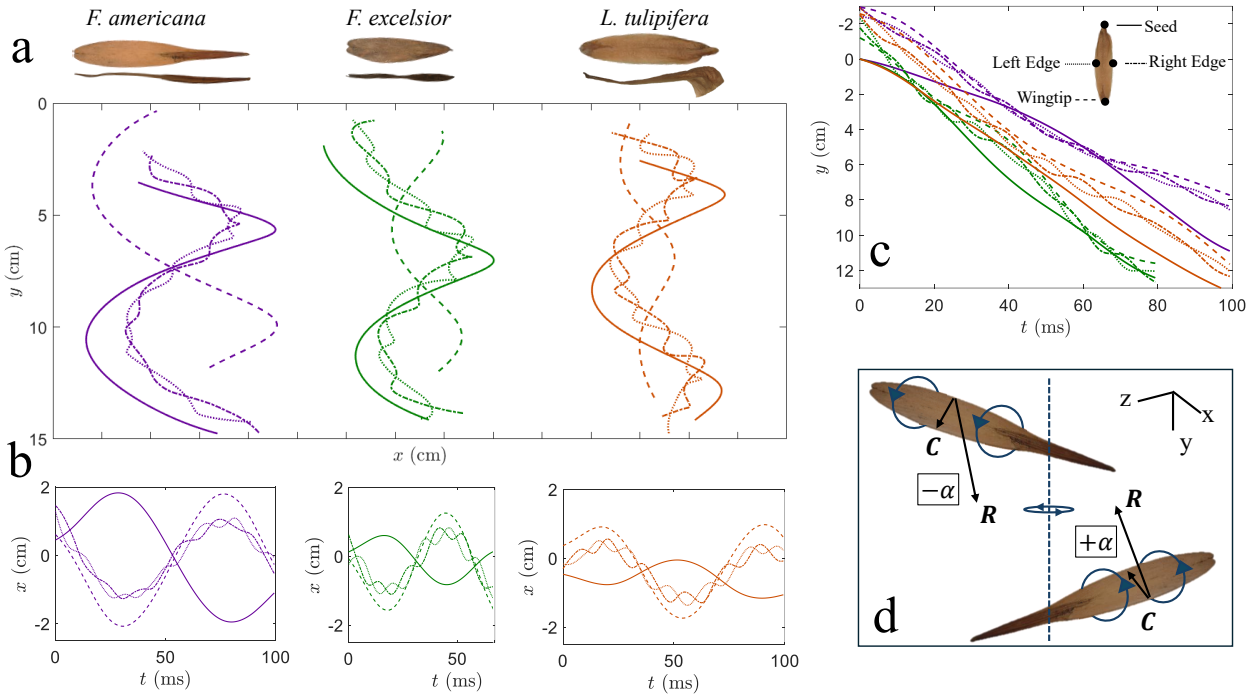

Figure 3.6: Kinematic and dynamic behavior of rolling samaras. **(a)** $x-y$-projections of helical descents, tracking the seed, wingtip, and chordal edges. **(b)** Temporal x-projections of descent show graphical comparisons of COR and rolls per precession cycle. **(c)** Temporal y-projections of descent show smooth tracks of seed and wingtip. **(d)** Representative orientations of a rolling samara showing positive $+\alpha$ and negative $-\alpha$.

seed.

We plot the temporal vertical displacement of the seed, wingtip, and chordal edges for three representative cases in **Fig.3.6**c. The seed follows a relatively smooth vertical trajectory, as its higher mass concentration attenuates local oscillations, maintaining a smooth helical path[24,25]. A subtle shift in the coning angle, obscured in the full descent profile shown in **Fig.3.6**a, becomes apparent when examining the vertical trajectories of each tracked point in **Fig.3.6**c. Similar behavior has been reported in other autorotating systems, where uneven mass distribution leads to periodic aerodynamic adjustments and variability in descent trajectory[90]. Across all test species, the average descent velocity V_d is 153 ± 32 cm/s, $N = 90$. By comparison, maple samaras (*Acer* spp.), which do not exhibit rolling, descend more slowly at 102 ± 9 cm/s[11,91].

Prior studies of autorotating seeds and flapping insects have shown that unsteady aerodynamic features—such as vortex shedding and lift oscillations—can promote flight stability rather than sensitivity[41,42]. Rolling samaras appear to leverage similar dynamics, using periodic changes in angle of attack to maintain controlled descent. We assert that the magnitude and timescale of lift oscillations are too small to interfere with precession, which is explored

below, and therefore the cause for the aforementioned coning angle oscillations, with a frequency that does not match ω_r, is unknown but may be the result of transients incurred during samara release.

Unlike flapping wings[73,92], which oscillate and periodically reverse their angle of attack α, rolling samaras undergo continuous spanwise rotation that steadily modulates α. The resulting periodic fluctuations reflect continuous rolling, rather than true reversals in wing–airflow alignment. Angle of attack α is periodic and discontinuous, transitioning from 90° to −90° upon the wing surface normal aligning with the airflow vector. The angle of attack is generically defined as,

$$\alpha = \tan^{-1}\left(\frac{\|\mathbf{R}\|\|\mathbf{C}\|}{\mathbf{R}\cdot\mathbf{C}}\right), \tag{3.3}$$

where $\mathbf{R} = \tan^{-1}()V_\mathrm{d}/0.75S\omega_p)$ is the local velocity vector and $\mathbf{C}$ is the vector between the chordal edges. Representative orientations of a rolling samara with positive ($+\alpha$) and negative ($-\alpha$) angles of attack, defined relative to the local direction of motion $\mathbf{R}$, are shown in **Fig.3.6**d. In contrast to rolling samaras, maple samaras (*Acer* spp.) maintain nearly constant angles of attack between 20° and 40° during descent[11,34,81]. Insects such as bumblebees[93], dragonflies[94], and beetles[95] maintain high angles of attack between 30° and 60°, enabling unsteady lift mechanisms such as delayed stall and leading-edge vortices[96]. Rolling samaras may leverage analogous aerodynamic effects through passive, cyclic modulation of angle of attack. Periodic fluctuations in α can regulate descent by adjusting lift across each rotation, a mechanism also observed in biological flyers such as mosquitoes[97].

Rolling induces small-amplitude perturbations superimposed on the dominant precession, introducing unsteady aerodynamic effects that should, intuitively, result in vertical oscillation of the wingtip[37]. However, we observe no such wobble of the wingtip. Prior studies of autorotating and fluttering plates suggest that the lift coefficient C_L during periodic motion can be approximated as a sinusoidal function[37]. Following Fang et al.[41], we can write the lift force due to rolling as

$$F_{L,r}(t) = \frac{1}{2}\underbrace{\left(C_1 \sin\left(\frac{2\pi t}{T}\right) + C_2\right)}_{C_L}\rho V_\mathrm{d}^2 A, \tag{3.4}$$

where $\rho = 1.23\,\mathrm{kg/m^3}$ is air density, and constants[41] $C_1 = 0.9$ and $C_2 = 0.7$. Eq. (3.4) mandates we assume $\mathrm{d}\omega_\mathrm{r}/\mathrm{d}t = 0$, which is confirmed by kinematic tracks (**Fig.3.6**b). Assuming this force acts at a moment arm of $S/4$ from the wingtip, the corresponding torque is

$$\tau_\mathrm{max} = \frac{S}{4}F_\mathrm{max}. \tag{3.5}$$

The moment of inertia for a thin plate of uniform density, about its short axis $mb^2/12$. We assume that the samara will pivot $S/4$ from the seed tip due to fluctuation in lift. The moment of inertia relevant to roll-induced lift can be estimated by the parallel axis theorem,

$$I = \frac{1}{12}mb^2 + m\left(\frac{S}{4}\right)^2. \tag{3.6}$$

The maximum angular acceleration induced by lift fluctuation is then

$$\dot{\omega}_{\max} = \frac{\tau_{\max}}{I} = \frac{3(C_1 + C_2)\rho V_{\mathrm{d}}^2 AS}{2mb^2 + 6mS^2}, \tag{3.7}$$

where $\dot{\omega}_{\max} \approx 197\,\mathrm{rad/s^2}$, using representative averages from *L. tulipifera*: $V_{\mathrm{d}} = 131$ cm/s, projected area $A = 2.141$ cm^2, span $S = 3.9$ cm, mass $m = 47$ mg, and wing thickness $b = 0.46$ mm.

To estimate the vertical displacement generated by $\dot{\omega}_{\max}$, we assume the acceleration acts over a quarter roll cycle. The resulting vertical displacement of the wingtip is

$$y_{\max} = \frac{3}{32}S\pi^2\frac{\dot{\omega}_{\max}}{\omega_{\mathrm{r}}^2}, \tag{3.8}$$

which yields $27\,\mu$m for $\omega_{\mathrm{r}} = 510.2$ rad/s. Such a minuscule displacement at the wingtip, an estimate that neglects added mass effects, explains why the roll does not visibly wobble the samara wingtip throughout precession.

3.3.2 Wing thickness is the prevailing dimension governing descent velocity

Our three focal species—*F. americana*, *F. excelsior*, and *L. tulipifera*—illustrate that rolling-autorotation can occur across a range of samara shapes. Tulip poplar (*L. tulipifera*) samaras are dry, woody, winged fruits with a span of 3.6 ± 0.3 cm, $N = 10$, each derived from a single carpel within an upright conical aggregate that disaggregates at maturity in late fall[98]. *L. tulipifera* samaras have bulbous seeds and strongly curved wings extending dorsally from the upper edge. Each unit in the conical aggregate contains one or two samaras that feature a dorsally extended wing that facilitates wind dispersal over distances up to five times the height of the parent tree[98]. In contrast, ash samaras exhibit flat, teardrop-shaped seeds[99]. The planar wings of *F. americana* taper symmetrically, while *F. excelsior* samaras have a subtly helical wing, introducing spanwise curvature **Fig.2.1**a. Morphological differences among our two ash species align with previous studies highlighting substantial inter- and

intraspecific variation in wing length, area, and seed-to-wing proportions[33,41,100]. Despite variability in form, all three species maintain an aspect ratio S/c averaging 4.5 ± 0.7 and seed-biased mass distribution that promotes autorotation. Despite their morphological differences, our three focal species share a surprising aerodynamic commonality; thickness b emerges as the most predictive trait shaping flight performance.

One might expect conventional length-based scaling laws to predict differences in aerodynamic behavior because many aerodynamic traits scale predictably with a characteristic length[101,102] L. In allometric scaling, planform area scales as $A \sim L^2$, and mass scales volumetrically as $m \sim L^3$. Such assumptions are widely applied to engineered rotors[103–105] and biological structures, including seed wings[11], to estimate drag, lift, and dispersal potential[34,106]. Across all three species in this study, however, neither the square of span S^2 nor chord length c^2 strongly correlates with area ($R^2 < 0.1$, **Fig.A.8**), challenging the intuition that planform dimensions reliably predict size and weight.

Instead, both mass and planform area exhibit strong scaling relationships with thickness for all test species. Mass follows an inverse power-law scaling based on best-fit regressions, with $m \sim b^{-1.44}$ ($R^2 = 0.811$), as shown in **Fig.3.7**a. Planform area scales positively with

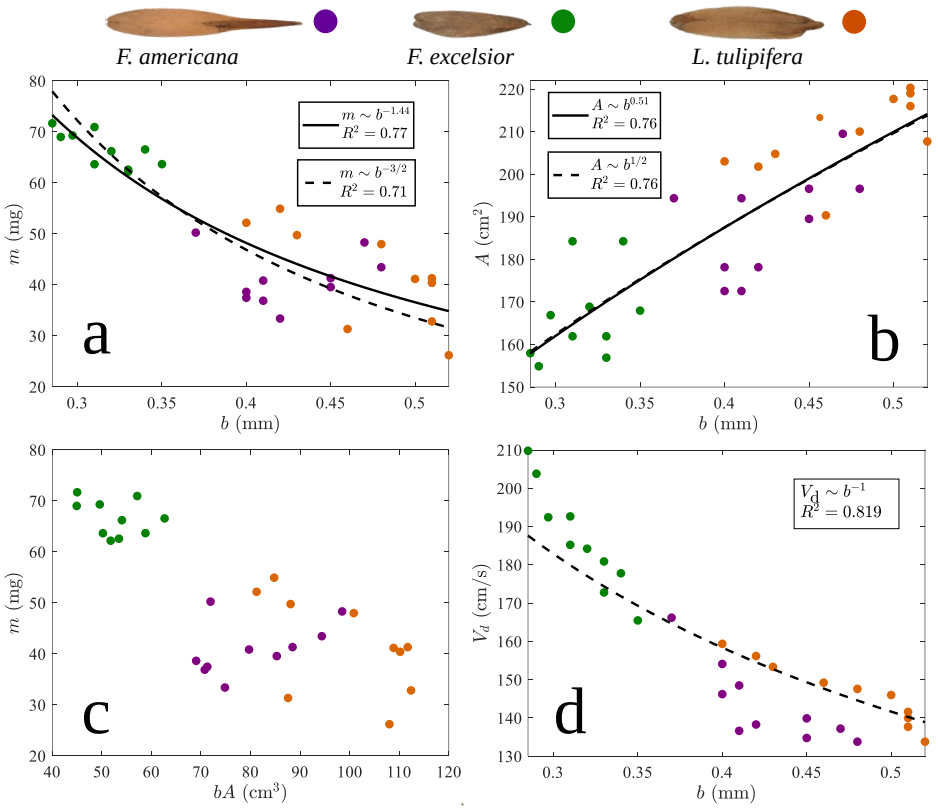

Figure 3.7: Scaling relationships in rolling samaras. **(a)** Mass m versus wing thickness b. **(b)** Planform area A versus b. **(c)** m vs bA. **(d)** Descent velocity V_d versus b.

thickness, following $A \sim b^{0.46}$ ($R^2 = 0.752$), as seen in **Fig.3.7**b. In short, the samaras with thinner wings are the heaviest. Although the relationships shown in **Fig.3.7** appear approximately linear on a log-log scale, the regressions are best fit by power-law models, which yield higher R^2 values than simple linear regressions. The reported coefficients and R^2 values correspond to these power-law fits.

The unexpected relationships plotted in **Fig.3.7**a,b suggest that structural integrity is not the primary factor driving thickness. On the contrary, a plot of bA versus m shows that rolling samaras are volume-conserving, with each species having a slightly different density, as shown in **Fig.3.7**c. Rather than distributing material uniformly, samaras concentrate structural reinforcement in the reproductive seed and central spine, while maintaining thinness at wing edges (**Fig.2.1**d). Strategic allocation of material in these regions likely enhances stability and mechanical efficiency without compromising aerodynamic function[34,106,107], but such an investigation is a topic for future simulation. Comparable design principles appear in engineered flight systems, where internal spars or composite reinforcements provide stiffness without increasing thickness throughout[108–110].

In light of the unexpected morphological scaling with thickness, we next consider the role of thickness and wing area on descent velocity V_d. In a previous study[11], we successfully united the descent velocity of nine *Acer* samara species using a classical drag model that combines form drag and lift,

$$mg \sim \frac{1}{2} C_D \rho V_{\mathrm{d}}^2 A \cos\theta, \tag{3.9}$$

where g is gravitational acceleration, C_D is the drag coefficient. Our above best fit scalings, $m \sim b^{-1.44}$ and $A \sim b^{0.46}$, are very close to more convenient choices for scaling exponents. We thus choose $m \sim b^{-3/2}$ ($R^2 = 0.77$) and $A \sim b^{1/2}$ ($R^2 = 0.73$) for substitution into Eq. (3.9). The result provides

$$V_{\mathrm{d}} \sim \frac{1}{b}, \tag{3.10}$$

plotted in **Fig.3.7**d, with $R^2 = 0.85$. The emergence of a simple, predictive relationship between thickness and descent velocity reveals that thickness plays a fundamental and previously underappreciated role in rolling samara flight. The establishment of Eq. (3.9) challenges the traditional view of relating terminal velocity to wing loading $V_{\mathrm{d}} \sim (mg/A)^{1/2}$, most notably proposed by Ausperger (1986)[71]. We defend the use of Eq. (3.9) by plotting V_d vs $(mg/A)^{1/2}$ for our data alongside the rolling samara data from Ausperger (1986)[71], Greene (1990)[111], and Azuma (1989)[31] in **Fig.A.9**.

The aerodynamic importance of thickness parallels findings in tumbling plate dynamics[38,112], where thickness influences rotational stability and descent behavior. Experimental[35] and computational[70] studies of falling plates have shown that increased wing thickness

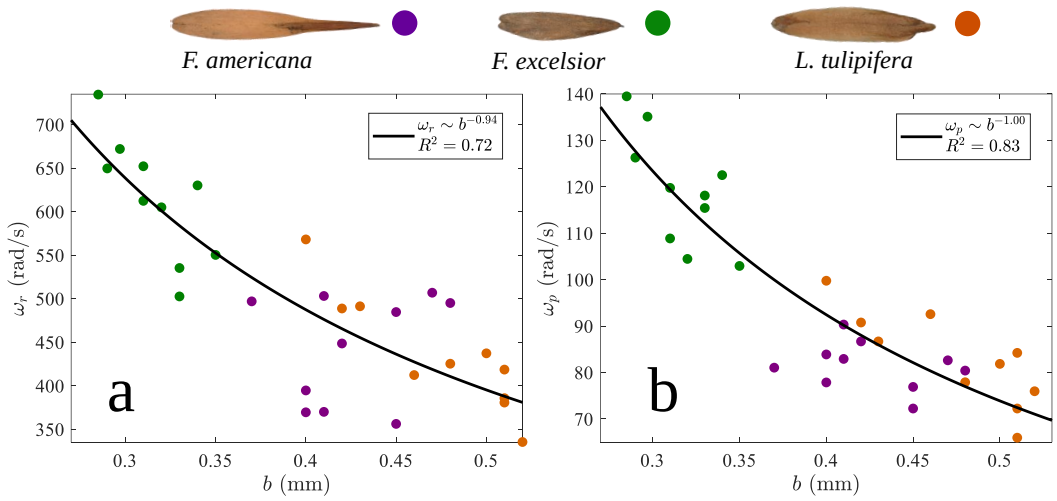

Figure 3.8: Relationship between wing thickness b and **(a)** rolling velocity ω_{r}, and **(b)** precession velocity ω_{p}.

suppresses chaotic or erratic motion and instead promotes periodic, stable rotation. Observations of rolling samaras reveal a similar trend. Rolling velocity decreases with thickness ($\omega_r \sim b^{-0.84}$, $R^2 = 0.72$, $N = 30$), an observation that is species independent, as shown in **Fig.3.8**a. precession velocity also decreases with thickness ($\omega_p \sim b^{-0.90}$, $R^2 = 0.83$, $N = 30$), as shown in **Fig.3.8**b. If we approximate the best fit in **Fig.3.8**b as $\omega_p \sim b^{-1}$, Eq. (3.10) provides $V_d \sim \omega_p$, an intuitive result. Seed descent traits such as morphology and terminal velocity influence not only flight dynamics but also ecological outcomes. Interspecific variation in descent rate has been shown to influence mean dispersal distance, with consequences for seedling establishment and overall plant fitness[71], suggesting that the aerodynamic differences reported here may carry important ecological implications.

3.3.3 Release position catalyzes rolling proceeding precession

Rolling, and thus precession, is more rapidly initiated from some static release positions than others. We filmed the release of three specimens from each species, with three replicates at each of five distinct starting orientations. Releases are initiated from the top of a vertical wind tunnel (Section 2). The wind tunnel provides a terminal velocity field that hastens the onset of stable autorotation in view of our high-speed camera. For each of 135 trials, we measure two key timepoints. The first is the time to complete one full rolling cycle, t_r. The second is the time to stable precession, t_p, defined as the time to levitation without further descent in the lab frame. We acknowledge that the method for determining t_r and t_p involves human interpretation during a frame-by-frame analysis, introducing a degree of subjective error, and estimate this error to be < 40 ms, or half the precession period of our

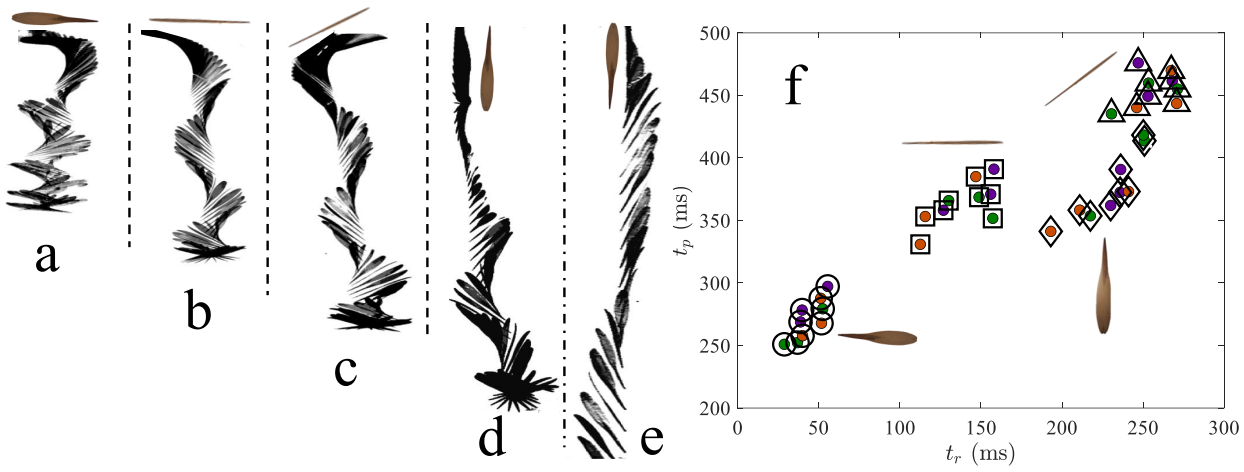

Figure 3.9: Initiation of autorotation in rolling samaras. (a–e) Sequential images illustrating different initial orientations of samaras relative to the airflow: **(a)** wing parallel to the flow, **(b)** wing perpendicular to the flow, **(c)** wing at a 45-degree angle to the flow, **(d)** wing parallel to flow with seed up, and **(e)** wing parallel to airflow with wingtip up. **(f)** Relationship between the time to complete one full roll (t_r) and the time required to achieve stable precession (t_p). Release orientation influences the time to steady autorotation.

slowest rotator. The qualitative responses to each initial orientation are consistent across all three species, enabling the generalization of behavioral trends without species-specific distinctions. Supplemental videos (Supp. M1–M5) are provided for each orientation to illustrate the observed responses.

The first orientation positions the samara chord parallel to gravity and span parallel to the horizontal, minimizing aerodynamic resistance at release, as depicted in **Fig.3.9**a (Supp. M1). In this configuration, the seed leads the descent, causing the wingtip to rotate upward. Rolling motion is initiated almost immediately, with an average time to roll of $t_r = 47 \pm 8\,\text{ms}$. Time to precession is also rapid, occurring within $t_p = 262 \pm 13\,\text{ms}$. All reported initiation times reported herein should be interpreted for the sake of comparison and are not representative of transients in natural conditions because the seeds experience a terminal velocity field immediately at release. Therefore, we expect natural entry into autorotation to be longer. Among all tested configurations, this orientation consistently produced the fastest transition into stable autorotation, confirming its aerodynamic favorability.

The second orientation positions the chord parallel with the horizontal, maximizing aerodynamic drag at release. In this case, rolling motion does not begin immediately; instead, the seed initially drops downward before rolling begins. Average time to roll increases to $t_r = 120 \pm 15\,\text{ms}$, while time to precession occurs at $t_p = 330 \pm 20\,\text{ms}$, as seen in **Fig.3.9**b. Once rolling begins, the transition to stable precession proceeds rapidly. A similar sequence occurs in the third orientation, where the wing is tilted at a 45° angle to the horizontal from

the second orientation. The seed initially flips downward, causing a brief delay in rolling initiation that can be attributed to the time it takes for the seed to rotate down. Time to roll in this case increases further to $t_r = 190 \pm 18$ ms, and precession is achieved at $t_p = 390 \pm 22$ ms, as shown in **Fig.3.9**c.

In the fourth orientation, the span is vertical with the seed facing upward. The samara flips seed-down to delay rolling compared to other orientations. Average time to roll is $t_r = 245 \pm 14$ ms, and stable precession develops after approximately $t_p = 460 \pm 18$ ms, as seen in **Fig.3.9**d. The fifth and final orientation positions the span vertically with the seed down. Intermittent rolling occurs throughout the descent, but the motion remains irregular. The samara does not fully transition to stable precession within our approximately 55-cm high tunnel viewing area, despite windspeed being set at the terminal velocity of the samara, as shown in **Fig.3.9**e.

Samaras that initiate rolling earlier (t_r) reach a steady precession (t_p) more quickly, as shown in **Fig.3.9**f. In natural conditions, samaras are unlikely to detach from the parent tree in the ideal orientation. Branch motion, wind disturbances, and variability in fruit abscission mechanics likely result in a wide distribution of initial orientations at release[111]. However, it has been shown that symmetric samaras released into a crosswind initiate rotation more rapidly than those in still air[113], indicating that orientation may be less critical than our results indicate.

Field observations have shown that tulip and ash samaras often fall in non-ideal orientations and may briefly descend without rotating before aerodynamic forces reengage and stabilize the flight path[33]. In these species, seed release occurs over an extended dispersal season—often lasting several weeks to months—during which environmental conditions such as wind, humidity, and temperature can vary substantially, increasing the likelihood of non-ideal release scenarios[111]. In contrast, species such as maples exhibit more temporally synchronized dispersal, with samara release typically concentrated within a narrow window of just a few days to a week[114], thereby limiting exposure to such variability. The observed consistency in rolling initiation across all species, even from suboptimal starting configurations, suggests that rolling samaras possess an inherent aerodynamic robustness that enables recovery from a range of initial states. Aerodynamic recovery from unfavorable orientations enhances time aloft and dispersal distance. Selection may therefore favor geometries that not only optimize steady-state flight but also promote reliable initiation of autorotation. Orientation-dependent initiation dynamics appear to be a critical, yet unstudied, component of the passive dispersal performance of rolling samaras.

3.4 Synthesis and Implications

A classical vertical force balance, $mg \sim \frac{1}{2} C_{\mathrm{D}} \rho V_{\mathrm{d}}^2 A \cos\theta$, unites autorotational descent across nine *Acer* species with a single effective coefficient ($C_{\mathrm{D}} \approx 6$), outperforming traditional wing loading by leveraging projected area $A\cos\theta$ (**Fig.3.1**). The drag balance captures interspecific agreement (drag $R^2 = 0.72$ vs. wing loading $R^2 = 0.35$) and exposes informative deviations: *A. negundo* behaves "underweighted" while *A. saccharum* appears "overweighted," signaling mass-distribution effects not evident from dynamics alone (**Fig.3.3**). Centrifugal forces are substantial, yet descent remains well described once $\cos\theta$ is included, yielding a practical, cross-species performance metric that integrates morphology (A), kinematics (θ, ω), and mass (m).

Rolling samaras reveal a complementary scaling regime governed by wing thickness. Empirical relationships $m \sim b^{-3/2}$ and $A \sim b^{1/2}$ inserted into the same drag framework predict $V_{\mathrm{d}} \sim 1/b$, matching measurements (**Fig.3.7**). Rolling and precession velocities decrease with thickness (**Fig.3.8**), while lift oscillations during spanwise rotation are too small to induce observable wobble, preserving smooth helical descent (**Fig.3.6**). Orientation at release modulates time to autorotation, yet robust initiation emerges across a wide range of starting states. Together, the autorotation and rolling results demonstrate that two compact descriptors—projected area with coning ($A\cos\theta$) and wing thickness (b)—provide predictive control parameters for passive seed flight. Subsequent sections link outliers to specific morphological traits (Section 3.2) and probe robustness under perturbations (e.g., added/removed mass; Section 4.1.2), with implications for dispersal modeling and bio-inspired aerial design.

Chapter 4
Samaras are robust to morphological perturbations

4.1 Morphological perturbations to maple samaras

4.1.1 Samaras are robust to mass addition

Suspended samaras are susceptible to environmental moisture such as rainfall and dewfall, a fate shared with foliage[115] and resting insects[116,117]. As samaras turn from green to brown, or in cycles of drought, one would expect their moisture content, and thus mass, to fluctuate. Some nutlets contain a seed while others are empty[118]. It follows, therefore, that samara flight is robust to some range of mass alteration. Our chosen species for mass augmentation are the over- and underweighted species identified in Section 3.1.1, and two additional species for comparison, the largest test species, *A. macrophyllum* and the smallest, *A. buergerianum*. We augment the mass of three specimens per species by dunking the nutlet in melted wax, where the number of dunks controls the amount of mass addition. The addition of wax contributes a $< 5\%$ increase in A (**Fig.A.5** Mass is added in subsequent flight tests until the samaras cannot levitate in our tunnel. We also subtract mass from one specimen per species by shaving mass from the nutlet in a manner similar to that done by Varshney *et al.* (2012)[24]. Mass is reduced in subsequent flight tests until the samaras cannot levitate in our tunnel. We provide movies of weighted and unweighted alongside their unaltered states hovering in our tunnel in Movies **S1** & **S2**, respectively.

We plot reduced velocity V/V_0 vs reduced mass m/m_0 in **Fig.4.1**a up to the point where modified samaras no longer auto-rotate, where V_0 and m_0 are the unmodified descent velocity and mass for each samara on test, respectively. Our largest samara, *A. macrophyllum*, tolerates the least amount of relative mass addition before failure at $m/m_0 \approx 1.3$ but performs best in relative mass reduction down to $m/m_0 \approx 0.3$. The overweighted samaras of *A. saccharum* (largest mass to area ratio **Fig.3.5**a) are the most sensitive to mass addition, $V/V_0 \sim (m/m_0)^{0.23}$, but continue to autorotate up to $m/m_0 \approx 1.5$. Whereas, the underweighted *A. negundo* is least sensitive to changes in mass, $V/V_0 \sim (m/m_0)^{0.06}$, with autorotation for $0.5 \lesssim m/m_0 \lesssim 2.25$. The best-fit scaling for the four augmented species is $V/V_0 \sim (m/m_0)^{0.12}$, $\mathrm{R}^2 = 0.80$. As a comparison, we also plot $V/V_0 \sim (m/m_0)^{0.5}$ with a dashed line from the prediction of Eqs. (1.1) and (3.1) for a constant area and note that the flight performance in response to changes in mass of these specimens is considerably different from what is predicted. Overall, samara descent velocity is remarkably robust to

mass addition and subtraction. It is clear that the starting point of the individual species is important such that the underweighted samara tested here (*A. negundo*) can withstand the most relative mass addition, whereas the overweighted samara (*A. saccharum*) performs slightly better when mass is reduced. Further, the velocity change is remarkably only ±15% of the average velocity for mass changes up to ±70%, revealing their ability to withstand major mass changes and still descend as intended. Mass subtraction, however, does not usher the descent speed retarding benefits predicted by the force balance of Eq. (3.1) (i.e. velocity reduction values are above $(m/m_0)^{0.5}$). Though Varshney *et al.* (2012)[24] does not report their test species, their results are comparable to our largest seeds (**Fig.4.1**a), with a mass reduction at the nutlet producing $V/V_0 = 0.75$ for $m/m_0 = 0.471$.

While mass alteration does little to influence samara descent velocity, the response in angular velocity is considerably more significant. Our *Acer* samaras maintain a relatively stable descent velocity by rotating more rapidly, generating more lift, in response to mass addition. We plot ω/ω_0 vs m/m_0 in **Fig.4.1**b, where all the all trials fit is $\omega/\omega_0 \sim m/m_0^{0.70}$, $R^2 = 0.77$. Weighting the smallest samara, *A. buergerianum*, produces the fastest rotation, $\omega/\omega_0 \approx 2$ for $m/m_0 \approx 1.5$. A greater increase in ω than V_d produces lower angles of attack ϕ for heavier *Acer* samaras (**Fig.A.6**

More rapidly rotating samaras descend with a flatter cone angle shown in **Fig.4.1**c such that $\theta/\theta_0 \sim (m/m_0)^{-0.48}$, $R^2 = 0.71$. We posit that the reduction in coning angle for added nutlet mass is the key to keeping $V_d/V_{\mathrm{d}0}$ lower than what would otherwise be expected from Eq. (3.1). To check this, we plot $\rho V_\mathrm{d}^2 A \cos\theta$ vs mg in **Fig.4.1**d, where black symbols represent unaltered specimens from each species. Color-coded dashed lines represent the linear correlation of Eq. (3.1) using individual species data plotted in **Fig.3.3**a, and their length represents the bounds of the original data. The reduction in coning angle enables samaras to outperform naturally heavier individuals within their own species even with an increase in V_d. The overall fit to all our altered trials (solid line) is nearly identical to the data in **Fig.3.3**a (dashed line). Deviations from the samara solid fit line are expected for overweighted and underweighted species (similar to **Fig.3.3**a). Deviations within species (colored dashed lines) are also expected since we altered the nutlet weight. Our results demonstrate that samaras are wonderfully adapted to carry altered masses up to 70% and even to 120% mass increase for underweighted species. Whether this is a genetically beneficial or necessary trait is worthy of future research.

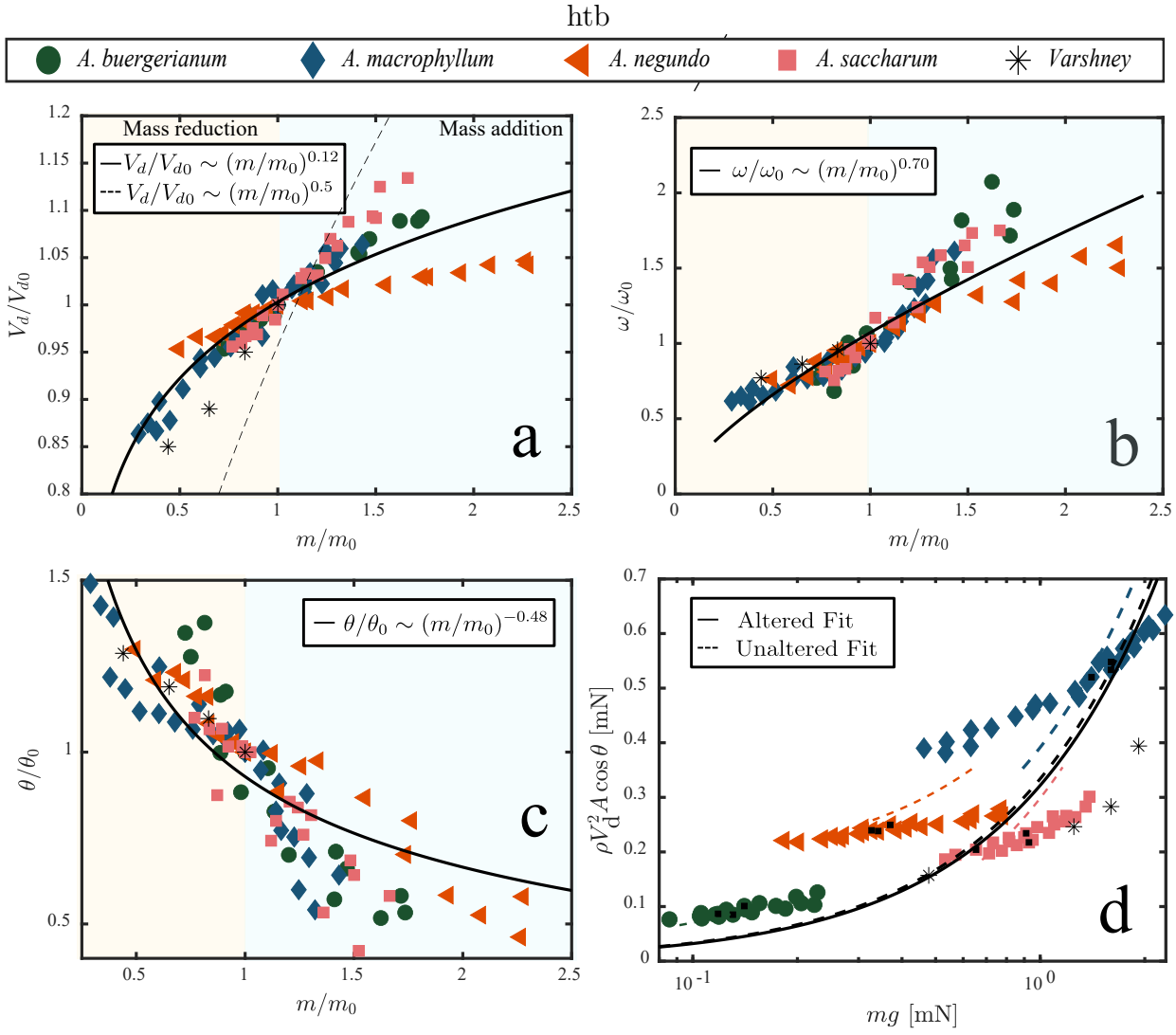

Figure 4.1: Samaras are robust to mass addition. **(a)** Reduced velocity V_d/V_{d0} vs reduced mass m/m_0, **(b)** reduced angular velocity ω/ω_0 vs reduced mass m/m_0, **(c)** reduced cone angle θ/θ_0 vs reduced mass ratio m/m_0 vs , and **(d)** drag force to samara weight mg.

4.1.2 Samaras autorotate with severely damaged wings

The long development time of samaras, approximately four months[118], makes samaras susceptible to herbivores that can damage their wings. Other events such as hail strikes might also induce damage. As with alterations to mass, we can further test Eq. (3.1) by perturbing samara wing area by ablation, similar to that done by Varshney *et al.* (2011)[24]. In so doing, we probe the robustness of samaras to damage to their thin, brittle wings. The addition of wing area is intractable, but the reduction in area of the wing at a location that is least aerodynamically sensitive, the trailing edge, is straightforward (Section 2.2, **Fig.A.1**). Ablation is done by removing strips of the wing from the trailing edge at approximately 25%, 50%, and 75% of the chord and done until the samara can no longer stably autorotate in our wind tunnel near $V_\mathrm{d}/V_\mathrm{d0} \approx 1.3-1.5$, at a reduced area $A/A_0 \approx 0.6-0.8$. Such removal of the thin wing has little effect on mass, $m/m_0 \geq 0.96$. We plot $V_\mathrm{d}/V_\mathrm{d0}$ to A/A_0 in **Fig.4.2**a. Descent velocity $V_\mathrm{d}/V_\mathrm{d0} \sim (A/A_0)^{-0.79}$, $\mathrm{R}^2 = 0.91$ is more sensitive to changes in area than predicted by Eq. (3.1) with all other variables held constant, $V_\mathrm{d}/V_\mathrm{d0} \sim (A/A_0)^{-0.5}$. Angular velocity is nearly unchanged by reduction in area, $\omega/\omega_0 \sim (A/A_0)^{0.03}$, even close to failure, as shown in **Fig.4.2**b. Coning angle θ increases with a reduction in area such that $\theta/\theta_0 \sim (A/A_0)^{-0.38}$, $\mathrm{R}^2 = 0.87$, with no notable standouts, as shown in **Fig.4.2**c. A hovering samara with an ablated wing is shown in Movie **S3**.

We plot drag force to weight for reduced wings in **Fig.4.2**d. Across all species, the linear fit to altered area samaras (solid line) and unaltered data in **Fig.3.3**a are similar. We thus conclude that samaras are robust to wing damage and area reduction on their trailing edge. Since we inflict damage on the trailing edges only, our results suggest that our modifications do little to affect the compact leading edge vortex critical for lift generation[81]. Removing wing area from both the leading and trailing edges has been shown to dramatically increase descent velocity as shown by Varshney *et al.* (2011)[24] and matches the trends in our data shown in **Fig.4.2**.

4.1.3 Altered samaras obey wing loading predictions

We discuss in Section 3.1.1 that a simple drag model, given by Eq. (3.1), is superior to Eq. (1.1) for describing the descent characteristics across samara species when numerous, unaltered maple samaras are used. The data presented in **Fig.3.1**a, is presented again in **Fig.4.3**a with adjusted axes. We observe a weak correlation between V_d^2 and mg/A for unaltered specimens. However, specimens in which mass is added and subtracted well obey $V_\mathrm{d}^2 \sim mg/A$, as shown in **Fig.4.3**b. The comparison of panels (a) and (b) reinforces that maple samaras are robust to changes in mass, but more strikingly, that the performance of

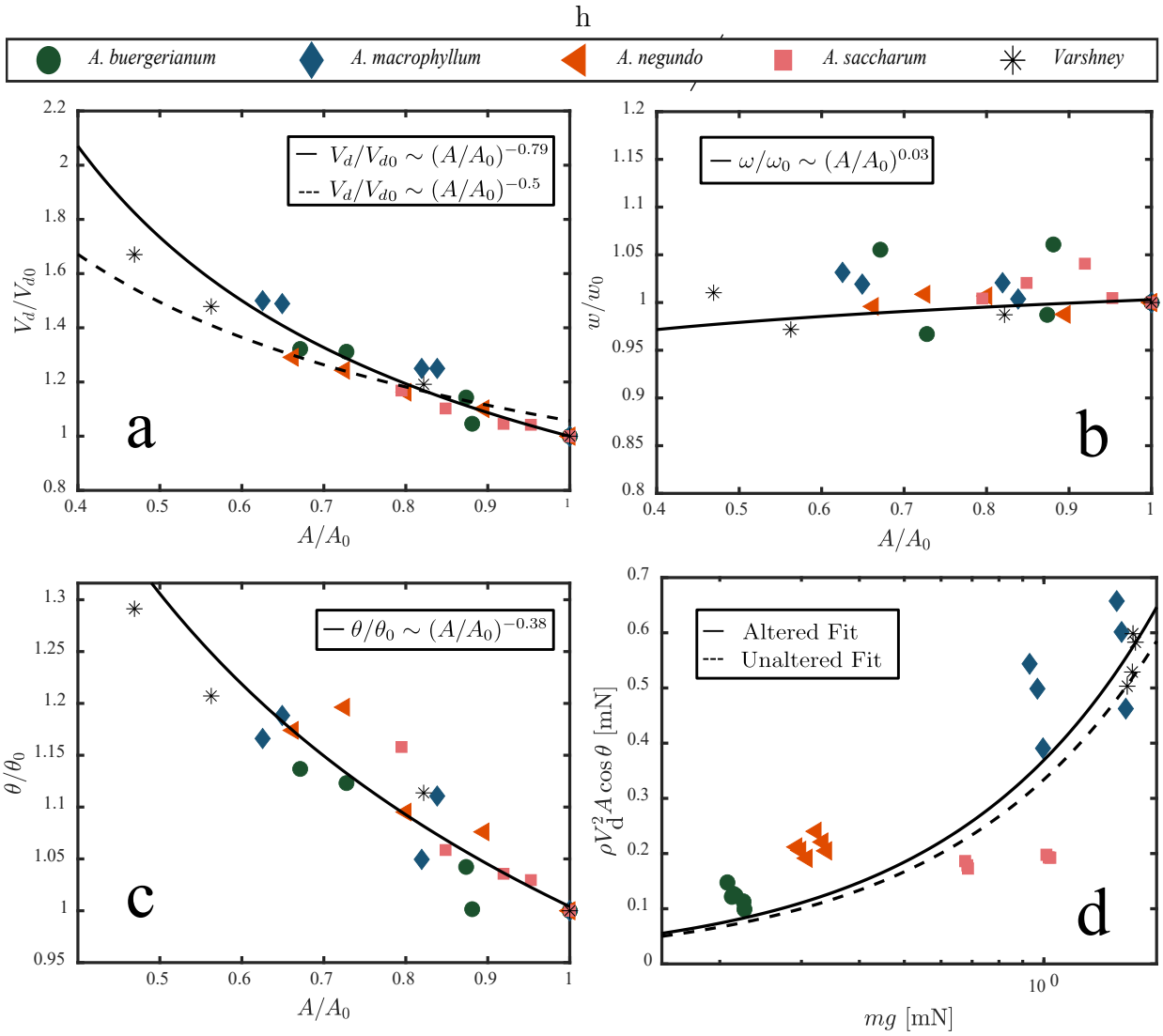

Figure 4.2: Samaras are robust to wing area ablation. **(a)** Area ratio A/A_0 vs velocity ratio V/V_0, **(b)** area ratio A/A_0 vs rotational velocity ratio ω/ω_0, **(c)** area ratio A/A_0 vs angular ratio θ/θ_0, and **(d)** weight mg to drag.

an individual specimen is inherent to the individual and more complex than a bare mg/A value can predict. We posit this is due to the small variations between specimens. Despite how well changes to descent velocity by mass alteration are predicted by wing loading, we observe that drag force and weight are more highly correlated. We plot all our experimental drag force values, altered and unaltered, alongside values from literature[24,27,31] in **Fig.4.3**c. Now, our drag model in Eq. (3.1) achieves an $R^2 = 0.70$, with an average $C_D = 5.68$. The remarkable similarity in the slopes in **Fig.3.3**a and **Fig.4.3**c underscores the robustness of our model. Perhaps the only advantage of Eq. (1.1) over Eq. (3.1) is a quick estimation of velocity change without the need to consider the coning angle.

The relation between drag coefficient C_D and angle of attack ϕ for all our tests is shown in **Fig.4.3**d. The trend between C_D and ϕ seemingly agrees with that reported by Lentink *et al.* (2009); ϕ changes very little, typically within 10°, with a large range of C_D[81]. While C_D increases slightly with mg, ϕ is functionally independent of mg, as shown in **Fig.A.7**.

4.2 Dimensionless Parameters Governing Continuous Spiral Tumbling

We investigate the aerodynamic response of falling paper across four aspect ratios, five scales, and three thicknesses. Each condition is experimentally represented by three replicate trials. In all trials, the paper consistently exhibits continuous spiral tumbling. Detailed kinematic analyses are presented to quantify responses to aspect ratio and thickness by measuring descent speed V, coning angle θ, precessional velocity w_p, rolling velocity w_r, and precessional radius r_p.

4.2.1 Dimensionless Aerodynamic Framework

Both rolling (continuous spiral tumbling) and autorotating samaras have been shown to follow a relationship between effective aerodynamic drag and descent velocity when treated as free-falling blunt bodies[11,119]. The falling paper analogs in the present study revealed a similar relationship, as illustrated in **Fig.4.4**. Following prior work, form drag and any lift generated during descent were combined into a single effective aerodynamic term acting opposite to the direction of motion, expressed as

$$mg \sim \tfrac{1}{2}\rho C_D V^2 A \cos\theta, \tag{4.1}$$

where $g = 9.81\,\mathrm{m\,s^{-2}}$ is gravitational acceleration, C_D is the effective drag coefficient,

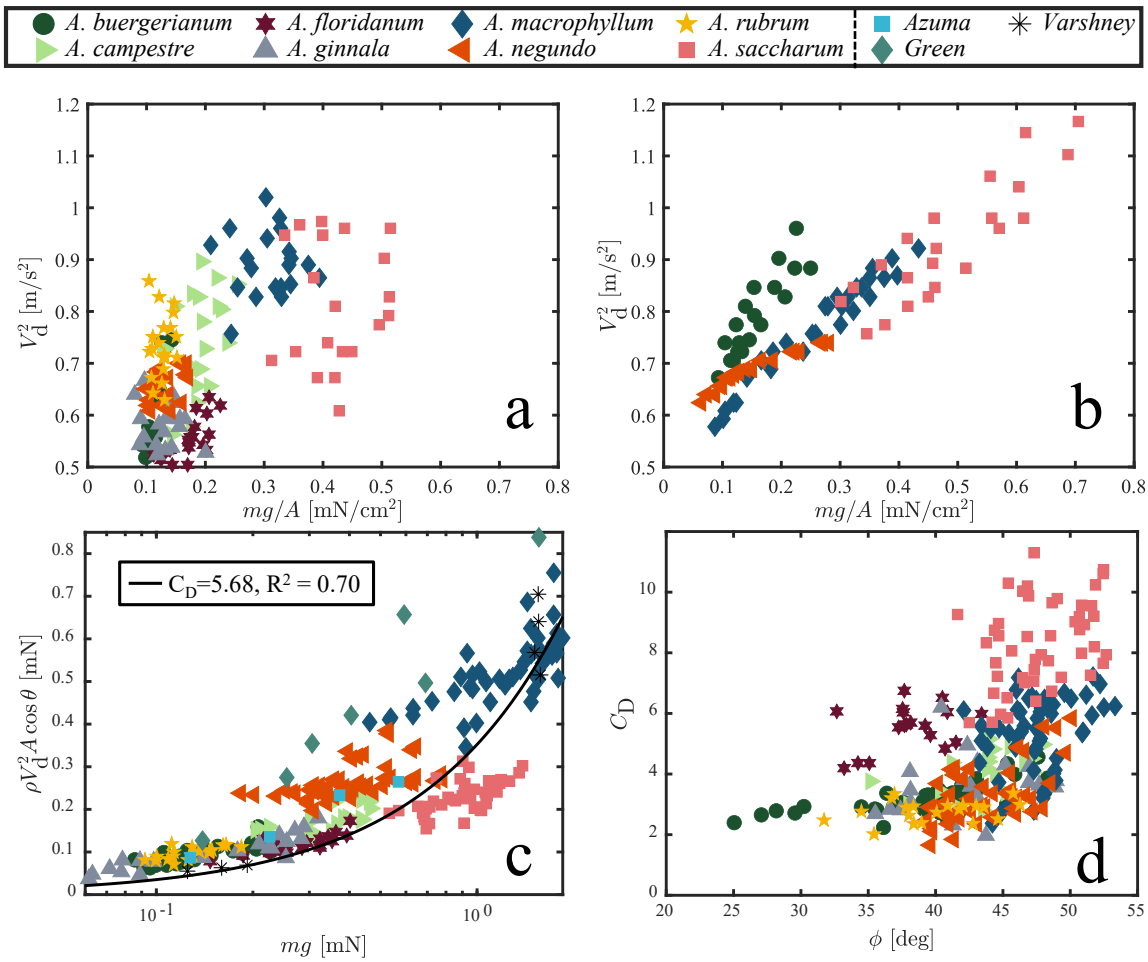

Figure 4.3: Relation between the square of decent velocity and wing loading on **(a)** unaltered (from Fig.3.1a) **(b)** altered samaras. Alterations include mass addition and subtraction. **(c)** Drag coefficient C_D versus samara weight mg for all altered and unaltered specimens in this study. **(d)** Drag force versus mg for all samaras in this study and select data from literature[24,27,31].

$\rho = 1.23\,\mathrm{kg\,m^{-3}}$ is air density, and $A\cos\theta$ is the projected area of the plate in the direction of descent. The slope of the best-fit line in **Fig.4.4**, with a correlation coefficient of $R^2 = 0.81$, yields an effective $C_D = 2.7$ across all paper samples. By comparison, *Acer* samaras exhibit $C_D \approx 1.1$, and rolling samaras yield values of similar magnitude.

The falling paper analogs demonstrate that even geometrically simple plates maintain a consistent drag–weight balance, but at a higher effective coefficient than samaras. Elevated C_D values indicate greater aerodynamic resistance per projected area. Samaras achieve lower effective coefficients through autorotational lift and the formation of a stable leading-edge vortex (LEV), which enhances vertical support while minimizing total drag[120,121]. The paper analogs, in contrast, exhibit unsteady rolling–tumbling kinematics that appear to be

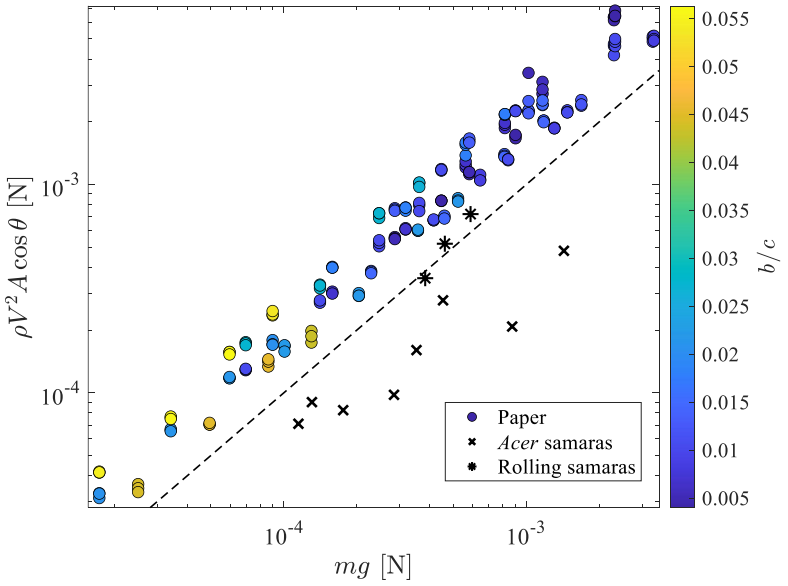

Figure 4.4: Relationship between effective weight mg and aerodynamic force $\rho V^2 A \cos\theta$ for falling paper, *Acer* samaras, and rolling samaras. Circles represent paper analogues. Black × represent *Acer* samaras and black asterisks represent rolling samaras.

dominated by pressure drag, with any LEV contribution likely intermittent or weak, which is consistent with the higher effective coefficients.

A higher C_D for paper does not imply faster descent, as the total aerodynamic force is distributed over a larger effective area and compensated by lower weight. For geometrically similar bodies, area increases with the square of length while mass increases more rapidly with volume, meaning that a larger or thicker plate experiences greater form drag relative to its weight. Consequently, paper analogs descend more slowly despite their larger C_D, because increased drag area offsets the effect of higher coefficients. The force balance plot in **Fig.4.4** therefore provides a unified framework linking engineered plate analogs to natural samaras: both satisfy the same drag–weight equilibrium, yet the aerodynamic mechanisms differ fundamentally. Biological samaras attain efficient autorotational flight with lower C_D through vortex-induced lift, whereas paper analogs require greater drag to maintain equilibrium due to the absence of lift augmentation and stable flow structures.

A long tradition of falling-body studies organizes descent behaviors on a regime map using the chord-based Reynolds number and a geometry-scaled moment of inertia. Following classic work on freely falling plates and disks[122] and the synthesis for plates by Andersen et al.[123] (see also[124]), the Reynolds number is taken as

$$Re = \frac{\rho_f V_d c}{\mu} \tag{4.2}$$

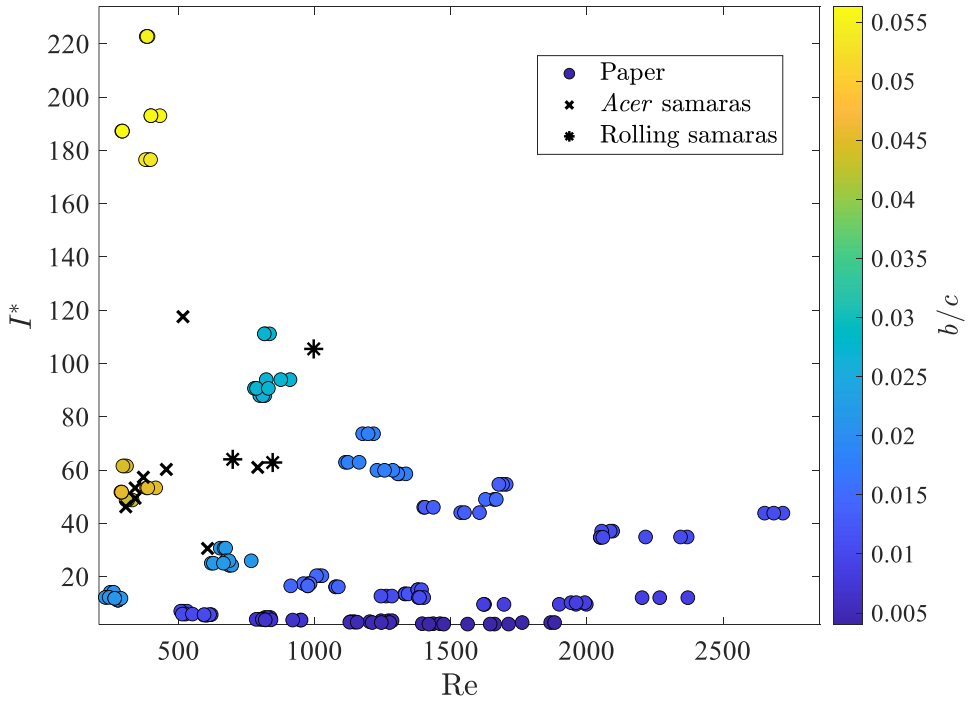

Figure 4.5: Regime placement of falling plates and samaras in Re–I^* space. Circles represent paper analogues. Black x represent *Acer* samaras and black asterisks represent rolling samaras.

where V_d is the mean descent velocity, c is the chord, and ν is the kinematic viscosity of air. The dimensionless moment of inertia is defined as

$$I^* = \frac{I_z}{\rho_f c^3 S^2}, \tag{4.3}$$

where $a = S/2$ is the half-span, $b = c/2$ is the half-chord, and I_z is the mass moment about the spanwise axis. For a thin rectangular plate,

$$I_z \approx \frac{m}{4}(c^2 + S^2). \tag{4.4}$$

Re representing the ratio of fluid inertia to viscosity and I^* representing body inertia normalized by fluid and geometric scales delineate the canonical transitions among steady autorotation, flutter/tumble, and coupled spiral regimes reported in prior experimental and numerical studies[122–124].

Building on the drag–weight balance, we now turn to where the trajectories reside in this canonical regime map defined by the Reynolds number and the dimensionless moment of inertia. As shown in **Fig.4.5**a, the chord-based Reynolds number spans approximately $Re \approx 300$–2600, placing the experiments within the regime where unsteady vortex shed-

ding and coupled lift–drag dynamics govern the motion[122,123]. The dimensionless moment of inertia, I^*, ranges from about 5 to 220, encompassing values that separate steady autorotation, flutter, and tumbling regimes[123,124]. Together, these parameters position the falling paper plates alongside both *Acer* and rolling samaras, enabling a direct comparison of their aerodynamic regimes.

Thicker plates occupy the upper portion of the plot, consistent with increased rotational inertia and reduced susceptibility to purely aerodynamic instabilities, as shown in **Fig.4.5**a. In contrast, thinner geometries cluster at lower I^*, corresponding to faster dynamic response and greater oscillatory amplitude. Subtle geometric modifications—such as those arising from natural variation in samara wing thickness—alter rotational inertia and therefore the coupling between translation and rotation during descent.

All data fall within the region associated with continuous spiral tumbling, with no transitions into steady autorotation or chaotic flutter observed under the tested conditions. The clustering of data points along this band, overlapping previously defined coupled-motion regimes, suggests that increasing thickness adjusts precessional and rolling timescales without moving the motion outside the coupled regime. The close overlap between the paper analogs and natural samaras further supports that both operate within a dynamically stable yet unsteady descent mode driven by a balance between aerodynamic torque and rotational inertia.

The drag–weight balance and the Re–I^* placement provide a consistent framework for interpreting subsequent results. The former establishes that vertical descent remains governed by an effective equilibrium of forces, while the latter situates the experiments in a phase space where geometry and inertia modulate aerodynamic torques. The next section leverages this placement to examine how oscillatory kinematics scale dimensionally through the Froude and Strouhal numbers.

Building on the regime placement in Re–I^* space, nondimensional parameters were used to characterize how inertia sets oscillatory kinematics during descent. The descent was expressed by the Froude number,

$$Fr = \frac{V}{\sqrt{gS}}, \tag{4.5}$$

and a Strouhal measure based on precession frequency,

$$\mathrm{St}_p = \frac{f_p\, S \cos\theta}{V}. \tag{4.6}$$

St_p decreases monotonically with increasing Fr as shown in **Fig.4.6**a. Larger Fr indicates stronger inertial dominance for a given size, so bodies fall faster per unit span, complete fewer precession cycles per unit vertical distance, and therefore display lower St_p. A simple

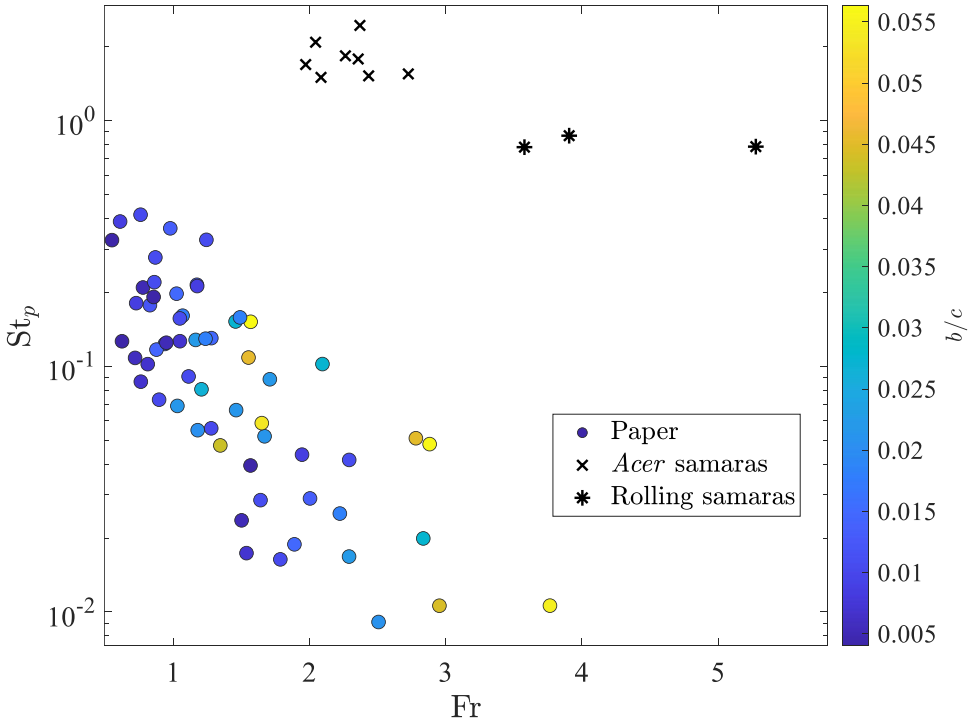

Figure 4.6: Froude–Strouhal regime placement for plates and samaras. Blue circles represent paper plates; black x represent *Acer* samaras; black asterisks represent rolling samaras. Color denotes the thickness-to-chord ratio b/c (see colorbar).

scaling captures the trend. If the precessional timescale is set by a gravitational–geometric clock, $t_g \sim \sqrt{S/g}$, then $f_p \sim \kappa/t_g = \kappa\sqrt{g/S}$, yielding

$$\mathrm{St}_p \sim \kappa \, \frac{\cos\theta}{Fr}, \tag{4.7}$$

an approximate Fr^{-1} decay. Plate data align with this inverse trend reported for freely falling cards and plates, where increased inertial dominance lengthens oscillation periods and broadens trajectories without violating the drag–weight equilibrium that sets V[122–124].

Autorotating seeds maintain elevated vertical force via a stable leading-edge vortex (LEV) at high effective angles of attack[120,121]. For comparable Re, samaras sustain lower V (hence lower Fr) while retaining high rotation rates, which shifts points upward in St_p relative to plates at similar geometry. *Acer* samaras occupy a distinctly higher St_p band at moderate $Fr \sim 2$–2.7, consistent with strong LEV-induced circulation that augments lift and maintains rapid spin. Rolling samaras plot at intermediate St_p despite operating at larger $Fr \sim 3.5$–5, indicating a different torque balance where spanwise roll couples to precession but lacks the same level of LEV augmentation seen in single-axis autorotation.

Color coding by thickness ratio b/c indicates only secondary variation at fixed Fr for plates, consistent with earlier Re–I^* results where thickness primarily shifts rotational inertia rather than the inertia–gravity balance that governs Fr. Residual scatter in St_p at fixed Fr likely reflects modest differences in $\cos\theta$ and frequency estimation rather than a systematic thickness effect.

Implications for dispersal follow naturally. Larger St_p at a given Re implies more frequent sampling of ambient turbulence per unit descent, promoting lateral meander and longer residence times aloft. Seed-dispersal theory links such low-Fr, high-St operating points to greater transport efficiency and broader dispersal kernels[125,126]. The Fr–St_p relationship therefore bridges biological and synthetic flyers. Plates delineate the inertia–gravity control of oscillatory descent, whereas samaras shift upward in St_p through LEV-driven lift that enhances aerodynamic efficiency and dispersal potential.

4.2.2 Helical framework for coupled rolling and precessional motion

Following the helical framework introduced by Schaeffer and Dickerson (2025), the coupled rolling and precessional motion of both the falling paper and the samaras can be represented as a three-dimensional helix that describes the path of the center of mass. Within this geometric description, the descent involves continuous rotation around a central vertical axis while the center of mass translates downward in a steady manner. The motion can be expressed parametrically as

$$\mathbf{r}(t) = \begin{bmatrix} r_p \cos(\omega_p t) \\ r_p \sin(\omega_p t) \\ V_z t \end{bmatrix}, \tag{4.8}$$

where r_p is the precessional radius, ω_p is the precession rate, and V_z is the vertical descent velocity. The helical framework provides a geometric connection between rolling and precession that defines the overall path of descent and establishes a clear link between rotation and translation.

The helical view unifies translational and rotational dynamics, capturing how the center of mass follows a repeating and spatially organized trajectory during descent, as shown in **Fig.4.7**. Variation in aspect ratio, scale, and thickness produces systematic differences in both lateral extent and vertical spacing, as seen in **Fig.4.7**. Larger aspect ratios produce wider helices with greater horizontal displacement, whereas increased thickness leads to more compact trajectories with reduced radial spread, as illustrated in **Fig.4.7**. The organized

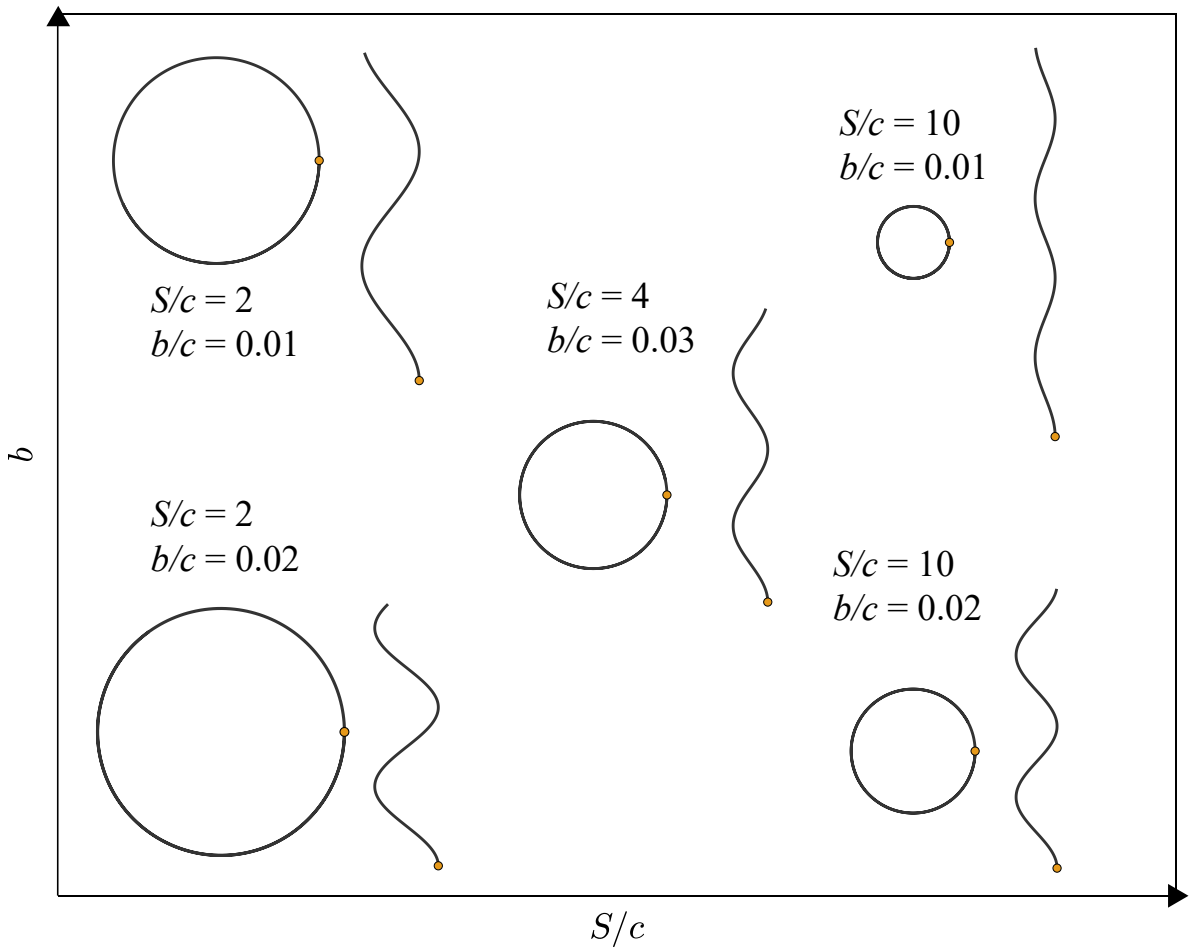

Figure 4.7: Representative helical trajectories of falling paper analogs across a range of aspect ratios (S/c), scales and thicknesses (b/c). The circles represent the precessional path of the fall looking from the x-y plane where as the falling trajectories next to them represent a 2 second fall.

paths reflect the geometric coupling between precession and descent, consistent with the helical motion described for natural samaras[119], as shown in **Fig.4.7**.

The helical framework highlights how morphological geometry dictates the balance between vertical descent and rotational motion during continuous spiral tumbling. A useful analogy for interpreting the relationship between descent speed and lateral motion arises from the concept of stiffness in a spring. The aerodynamic stiffness of the system can be represented by the ratio $V \sim c/r_p$, which describes how vertical velocity scales with the confinement of the helical path. A smaller precessional radius relative to chord implies that the flow is redirected more vertically, yielding higher descent speeds and a stiffer aerodynamic response[37,123]. Increased stiffness reflects a stronger coupling between aerodynamic torque and restoring lift, as the rotating plate resists lateral displacement and drives a concentrated

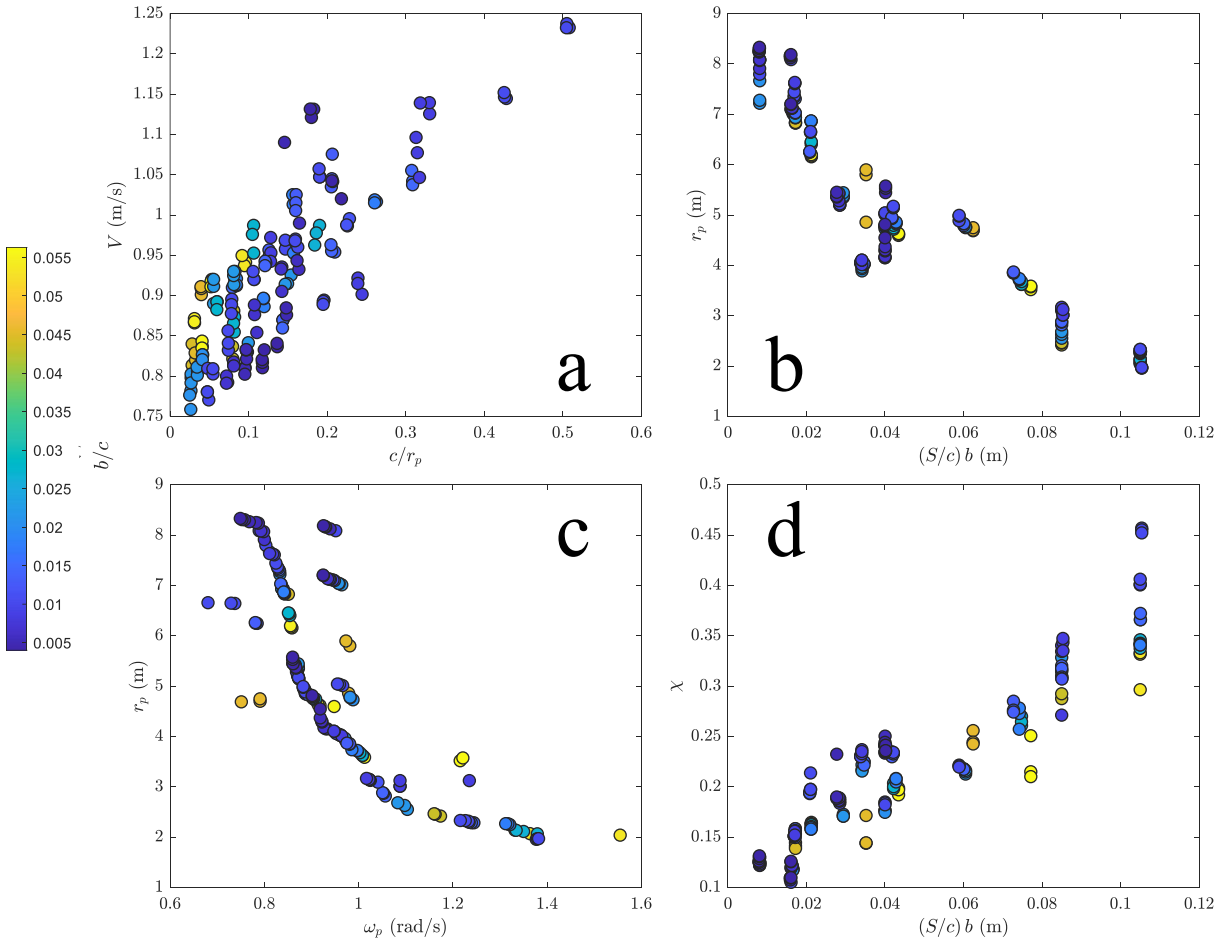

Figure 4.8: Helical and loading scalings for falling paper analogs. (a) V versus cSb with color indicating b/c. (b) $\cos\theta$ versus $1/V^2$. (c) r_p versus $(S/c)\,b$. (d) $\chi = V/(\omega_p r_p)$ versus $(S/c)\,b$. Velocity increases with cSb. The quantity $\cos\theta$ collapses against $1/V^2$. The precessional radius r_p decreases with $(S/c)\,b$. The tightness χ increases with $(S/c)\,b$, which implies a larger pitch angle and a looser winding for geometries with greater span to chord and greater thickness.

downward jet that sustains motion **Fig.4.8**.

The precessional radius r_p varies with the morphological combination $(S/c)b$, which aggregates span, chord, and thickness into an effective geometric loading parameter. Greater span and thickness reduce r_p, constraining the motion to a narrower helical path and concentrating circulation near the central axis. Confinement of the wake produces higher vortex coherence and a more stable leading-edge vortex, consistent with findings for autorotating samaras and tumbling plates[120,121]. Morphologies with smaller r_p therefore generate stronger, more vertically aligned flow structures that enhance the steady aerodynamic support required for prolonged rotation **Fig.4.8**.

A second dynamic coupling emerges between r_p and precession rate ω_p, revealing that increased angular velocity accompanies reduced precessional reach. Faster precession com-

presses the helical path and increases the frequency of vortex shedding, enhancing rotational stability but reducing the lateral sweep of the trajectory. The relationship mirrors the trade-off between angular momentum and radius in mechanical systems where rotational energy is redistributed through spring contraction[127]. Aerodynamically, higher ω_p confines the flow near the body, intensifying tip vortices and narrowing the wake envelope **Fig.4.8**.

The dimensionless tightness parameter χ originates directly from the parametric definition of the helix, where the trajectory of the center of mass is expressed as $\mathbf{r}(t) = [r_p \cos(\omega_p t),\, r_p \sin(\omega_p t),\, Vt]$. The ratio of vertical to azimuthal motion yields

$$\chi = \frac{V}{\omega_p r_p}, \tag{4.9}$$

which can also be interpreted as the cotangent of the helix angle α. The parameter therefore integrates the three principal kinematic quantities—vertical velocity, precession rate, and precessional radius—into a single dimensionless measure of geometric tightness. Large χ corresponds to loose helices that advance farther per revolution, while small χ represents tightly wound trajectories with greater aerodynamic loading. The observed increase of χ with $(S/c)\, b$ suggests that broader and thicker plates form less compact helices with longer vertical spacing per revolution. The trend indicates an aerodynamic trade-off between drag-induced lift and inertial stability[122,123] **Fig.4.8**.

Variation in stiffness and tightness across geometry demonstrates that aerodynamic morphology regulates both the structure of the flow and the efficiency of momentum exchange during descent. Plates with large χ and low stiffness resemble samaras that exploit broad, slowly precessing helices for efficient energy exchange with the air, extending flight time and enhancing dispersal potential. Configurations with high stiffness and small χ generate compact, rapidly rotating helices characterized by stronger pressure-driven lift and greater vortex confinement. The interaction among geometry, stiffness, and tightness defines how continuous spiral tumbling evolves as a stable, repeatable mode of descent that balances aerodynamic torque, vortex organization, and energy dissipation **Fig.4.8**.

Linking these geometric and kinematic results to the earlier drag–weight and Re–I^* relationships reveals a consistent framework. The force balance establishes the vertical equilibrium that fixes the descent speed, while the regime map situates the motion within the range of parameters where unsteady vortex shedding and rotational coupling dominate. The dimensionless variables V/cr_p and $\chi = V/(\omega_p r_p)$ extend this foundation by describing how geometry reorganizes that balance within a three-dimensional helical flow. Morphological variation therefore modifies the stiffness and tightness of the trajectory without altering the fundamental equilibrium of forces, suggesting that continuous spiral tumbling operates

as a dynamically stable mode of descent governed by geometric scaling and fluid–structure interaction.

The helical framework provides more than a geometric description of motion. It establishes a physical basis for connecting shape, rotation, and descent within a unified set of variables that link directly to flow organization. The parameters r_p, ω_p, and χ describe how aerodynamic forces redistribute momentum between vertical and azimuthal directions, revealing how morphological scaling controls the coupling between torque generation and descent stability. Understanding how stiffness and tightness vary with geometry clarifies how rolling seeds maintain steady, repeatable motion despite unsteady flow. Such insight extends beyond seed flight, as it defines a tractable framework for predicting how small, passively rotating bodies interact with their wakes. Continuous spiral tumbling therefore represents not only a biological strategy for efficient dispersal but also a fluid–structure mechanism that demonstrates how geometry alone can stabilize complex three-dimensional motion in unsteady aerodynamic environments.

4.2.3 Comparison to samaras

Area normalization enables direct comparison between the paper analogs and natural rolling samaras. Larger planform area promotes faster descent, consistent with the aerodynamic scaling expected from lift and drag balance during autorotation. Falling paper, however, descends more slowly than samaras with comparable normalized area. The difference arises from the absence of optimized curvature and mass distribution that natural seeds use to generate and sustain coherent leading-edge vortices. Uniform thickness and flat geometry limit the capacity of paper models to redirect flow and maintain steady lift, producing slower descent and reduced aerodynamic efficiency **Fig.4.9**.

Coning angle increases with normalized area, revealing a geometric adjustment to changing aerodynamic loading. Greater area produces larger aerodynamic torque and a higher restoring moment, causing a wider coning motion that stabilizes descent. Similar adjustments occur in natural samaras, where span and chord determine the equilibrium angle of attack and the structure of the attached vortex ring[39,69,128]. Variation in cone angle with area therefore reflects a shared aerodynamic principle across both biological and synthetic forms **Fig.4.9**.

The relationships between velocity, area, and angle follow from the quasi-steady drag balance expressed as

$$mg \sim \tfrac{1}{2}\rho A C_D V^2 \cos\theta. \tag{4.10}$$

Because mass scales approximately with area and thickness as $m \propto Ab$, the velocity relation

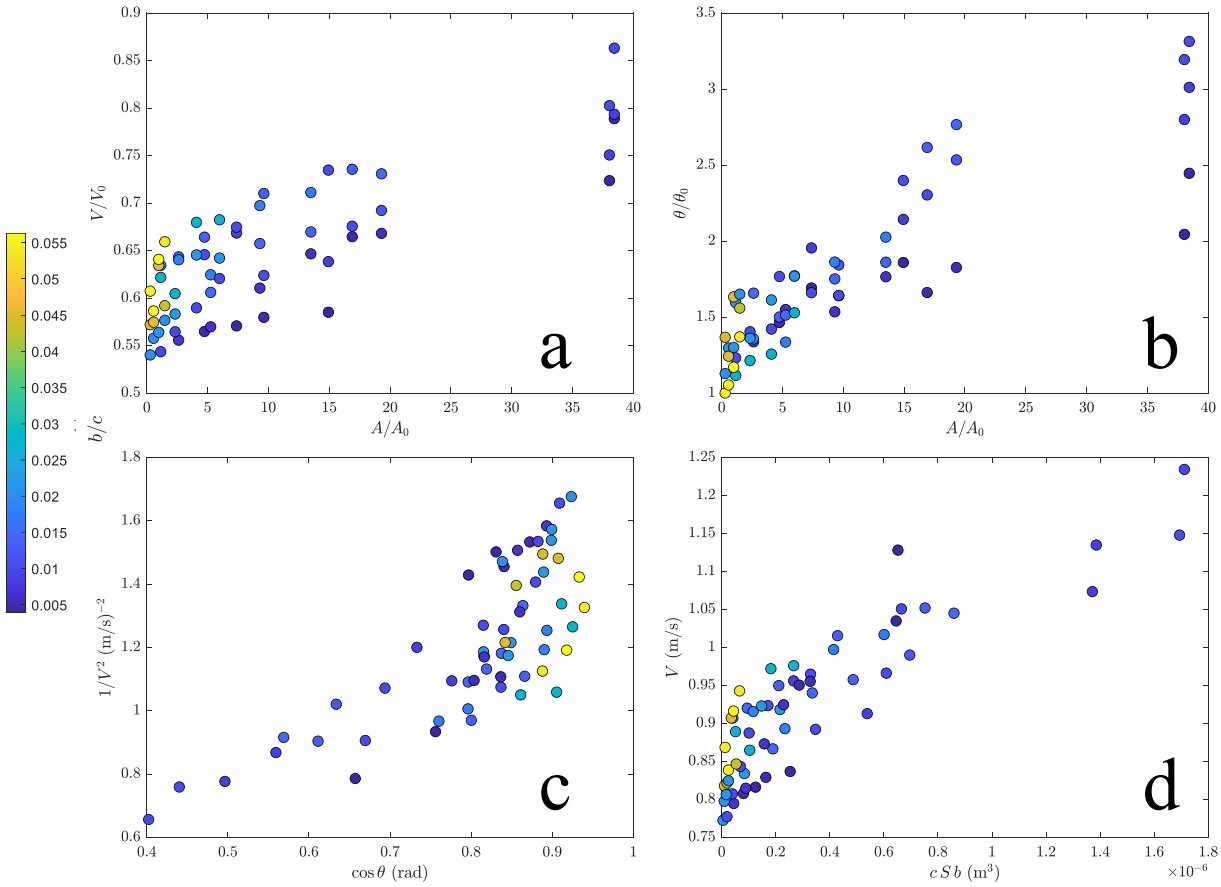

Figure 4.9: Area normalized comparisons with color indicating the group mean thickness-to-chord ratio b/c. (a) V/V_0 versus A/A_0 shows a modest increase in normalized descent speed across a wide range of normalized area. (b) θ/θ_0 versus A/A_0 increases steadily, indicating geometric adjustment of the cone with larger area. (c) $1/V^2$ versus $\cos\theta$ illustrates a near-linear correspondence predicted by quasi-steady drag balance. (d) V versus cSb shows velocity scaling with geometric loading. Points are means over trials for each combination of aspect ratio, scale, and thickness.

simplifies to $V^2 \sim g/(\rho b \cos\theta)$. The inverse dependence between $1/V^2$ and $\cos\theta$ reflects the way aerodynamic loading adjusts to maintain equilibrium between drag and weight, while the trend between V and cSb represents the geometric scaling of descent rate with effective aerodynamic volume **Fig.4.9**. Falling paper thus obeys the same aerodynamic structure as rolling samaras but with slower, more dissipative motion.

Natural samaras maintain consistent size, aspect ratio, and thickness-to-chord ratio that preserve vortex coherence and aerodynamic stability across a wide range of conditions. Morphological tuning enables stable autorotation even when exposed to wind, rain, and impact disturbances[69,129]. Controlled experiments with paper analogs reveal how deviations from this tuned morphology alter coning behavior and reduce aerodynamic support. The comparison highlights the aerodynamic sophistication of natural samaras, whose geometry allows

passive stability and sustained lift that enhance dispersal distance and environmental resilience **Fig.4.9**.

4.3 Synthesis and Implications

Evidence across maple and rolling samaras, together with controlled paper analogs, resolves continuous spiral tumbling as a quasi–steady, passively stable descent mode governed by a simple drag–weight equilibrium and geometry–inertia scaling. A helical state description with $\{r_p,\ \omega_p,\ V\}$ links translation and rotation, and the tightness $\chi = V/(\omega_p r_p)$ condenses how vertical advance trades against azimuthal sweep without requiring additional parameters **Fig.4.8**. Placement in $(Re,\ I^*)$ space shows all bodies operating within the coupled–spiral band, where thickness adjusts rotational timescales via I^* yet leaves the fundamental mode unchanged **Fig.4.5**. Precessional radius contracts with the geometric loading combination $(S/c)b$, while χ grows along the same coordinate, indicating that morphology regulates both lateral reach and pitch of the helix through a single effective knob **Fig.4.8**. Paper plates satisfy the same drag–weight relation as samaras but at higher effective C_D and lower V, consistent with weaker or intermittent leading–edge vortices and a larger contribution of pressure drag to vertical support **Fig.4.4**. Natural seeds achieve lower effective coefficients by sustaining vortex–augmented lift that preserves autorotation across environmental variability, explaining faster descent at comparable area without loss of passive stability **Fig.4.4**. Perturbation tests reinforce this picture: added nutlet mass and trailing–edge ablation elicit compensatory shifts in ω and θ while preserving the helical trajectory, yielding near–linear trends in normalized velocity ratios and demonstrating wide stability margins for rolling species with distributed mass and for maple species that adjust cone angle and spin to maintain equilibrium **Fig.B.1**.

The framework developed here is predictive and portable. Geometry chooses operating points in $(Re,\ I^*)$, fixes stiffness–like behavior through $V/(c\,r_p)$, and sets the helix pitch through χ, enabling quantitative links from shape to residence time aloft and lateral meander under realistic winds **Fig.4.8**. Ecological models of dispersal can absorb these compact variables to connect morphological variation to transport kernels without abandoning mechanistic fidelity, while seed–inspired autorotors can target the spiral–tumbling band and tune $(S/c)b$ to command r_p and θ without sacrificing passive stability **Fig.4.5**. Direct tomographic flow visualization and controlled center–of–mass and planform perturbations constitute the natural next step (see **Appendix D**), resolving the topology of the leading–edge vortex during coupled rolling–precession and mapping stability boundaries under gusts so that kinematic scalings can be tied unambiguously to wake structure.

Chapter 5
Samaras are robust to dynamic perturbations

5.1 Samaras recover after impact with raindrops

5.1.1 Collisions with various samara regions govern impact dynamics

The impact zone onto which a raindrop connects with a samara determines the dynamic response, such as the coning angle θ, and peak post-impact descent velocity $\dot{y}_{\mathrm{m}}$ and rate-of-change of coning angle $\dot{\theta}_{\mathrm{m}}$, thereby influencing recovery distance and the drop shedding mechanism (Section 5.1.2). A lab frame recovery distance y is measured by referencing the location of the nutlet tip at impact $t = 0$ and after recovery. We report 'corrected' values of distance to represent a natural recovery, such that $L = V\tau - y$, where τ is the time from impact to recovery.

We segment the samara into five impact zones, shown in **Fig.5.1**a. Samaras respond to drop impacts on the nutlet by increasing the coning angle, as pictured in **Fig.5.1**b. We plot the vertical displacement y of samaras upon impact, with respect to the laboratory frame, in **Fig.A.10**. Impacts on the nutlet push our samaras downward $y < 10$ cm while increasing $\theta < 25°$. The corresponding corrected recovery distance L is plotted vs $\dot{\theta}_{\mathrm{m}}$ in **Fig.5.2**a. Impacts onto the nutlet region produce the greatest positive peak pitching rate $\bar{\dot{\theta}}_{\mathrm{m}} = 8 \pm 4$ rad/s and slowest observed post-impact descent velocity $\bar{\dot{y}}_{\mathrm{m}} = 31 \pm 18$ cm/s, as seen in **Fig.5.2**b. A low $\dot{y}_{\mathrm{m}}$ ensures the shortest average recovery distance for nutlet impacts of $\bar{L} = 23 \pm 6$ cm. Upon impact the largest second moment of inertia samaras in our study, *A. negundo*, rotate most slowly, and the most massive samaras, *A. floridanum*, exhibit the most gradual change in descent velocity.

Impacts on the root, very near the samara center of mass (COM)[24,91], push the samara downward with relatively little rotation, as pictured in **Fig.5.1**c. The initial rotation can be either an increase or decrease in θ, dependent on which side of the center of mass the drop strikes. The average angular velocity post-impact is $\bar{\dot{\theta}}_{\mathrm{m}} = 1 \pm 12$ rad/s (**Fig.5.2**a), further highlighting the pushing, rather than rotating role the drop plays in this impact region. Despite low initial rotation from stasis, the samara seemingly over-corrects its coning angle after separation from the drop, as shown in the second row of **Fig.A.10**. The root region of the samara is relatively small such that impacts near the leading or trailing edge result in

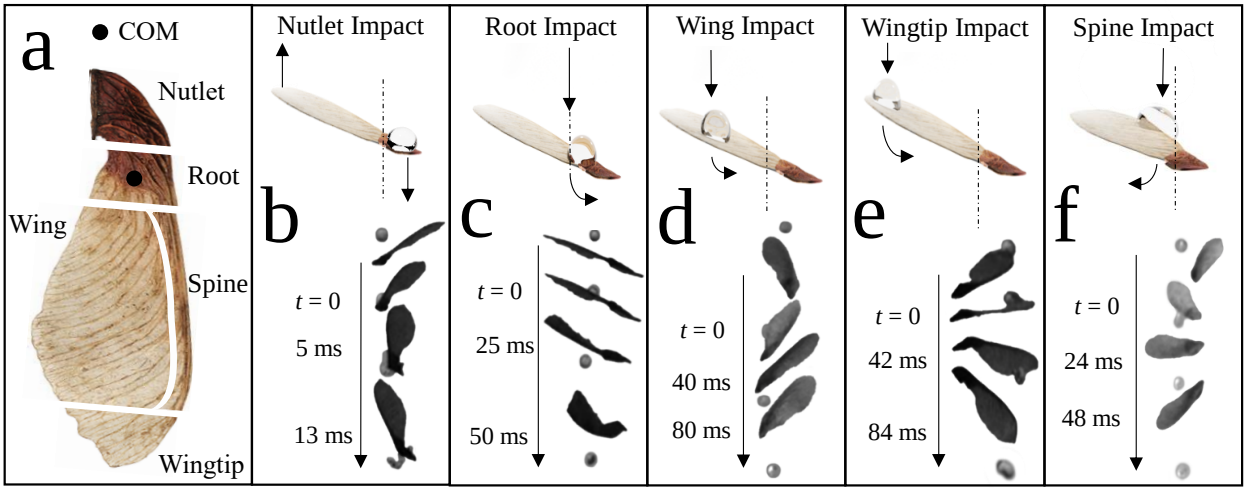

Figure 5.1: Samara impact regions and responses to impacts. (a) Seed regions, center of mass (COM). (b) Nutlet (c) Root (d) Wing (e) Wingtip and (f) Spine. Image sequences correspond to the response after impact with drops.

a rapid roll-off of the drop and small y, whereas more centered impacts cause the drops to splash and push the seeds downward $y \approx 40$ cm in our tunnel. The large range of y for root impacts corresponds to a wide distribution in L and $\dot{y}_\mathrm{m}$, shown in **Fig.5.2**b.

The samara responds to impacts on the wing trailing edge by rolling the samara along its long axis, shown in **Fig.5.1**d. In contrast to other regions, the coning angle change for on-wing impacts is characterized by a more slight change followed by a slower return to an autorotation angle, shown in the third row of **Fig.A.10**. A post-impact value of $\bar{\dot{\theta}}_\mathrm{m} = 3 \pm 8$ rad/s (**Fig.5.2**a) emphasizes that the rolling motion of the samara is less disruptive to the coning angle than impacts onto any other region. The average descent velocity induced by these impacts at $\bar{\dot{y}}_\mathrm{m} = 68 \pm 28$ cm/s, is the second highest among the impact regions, indicating that impacts in this area lead to relatively rapid downward acceleration. A high $\dot{y}_\mathrm{m}$ resulted in samaras being pushed downward $y = 30$ cm in the lab frame, and a corresponding corrected recovery distance $\bar{L} = 50 \pm 16$ cm.

The wingtip, being the farthest point from the center of mass, experiences impacts that cause the samara to undergo the most significant $\dot{\theta}_\mathrm{m}$ and $\dot{y}_\mathrm{m}$. Upon impact, the samara responds by decreasing the coning angle θ, as schematized in **Fig.5.1**e. Impacts in the wingtip region exhibit the largest change in coning angle, as shown in row four of **Fig.A.10**. As a result of the abrupt change in coning angle, the wingtip region exhibits the largest negative angular velocity among the impact regions, averaging $\bar{\dot{\theta}}_\mathrm{m} = -20 \pm 14$ rad/s, seen in **Fig.5.2**a. The large angular velocity $\bar{\dot{\theta}}_\mathrm{m}$ corresponds to a high post-impact descent velocity $\bar{\dot{y}}_\mathrm{m} = 85 \pm 22$ cm/s, shown in **Fig.5.2**b. Both the large angular velocity and high post-impact descent velocity result in the furthest corrected recovery distance of the samara regions at

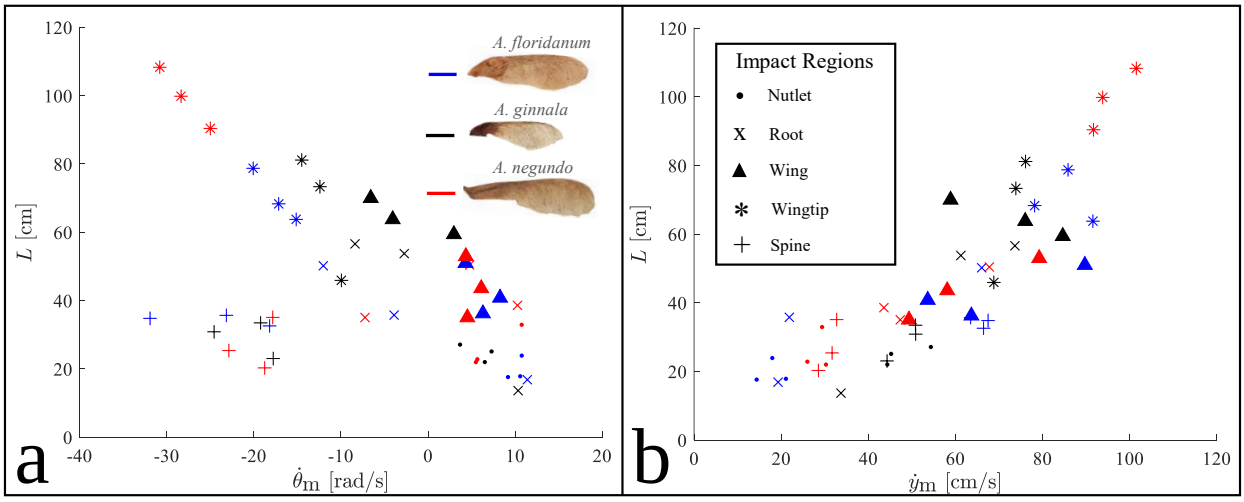

Figure 5.2: Samara velocities post drop impact corresponding to recovery distance L. (a) coning angle velocity $\dot{\theta}$. (b) post-impact descent velocity $\dot{y}_m$. The legends in both panels apply to the entire figure.

$\bar{L} = 79 \pm 26$ cm.

Spine impacts occur when the leading edge of the samara wing intersects the drop during autorotation, much like a fan blade clipping a careless finger, as depicted in **Fig.5.1**e. Spine impacts reduce the coning angle and rapidly slow rotation. The reduction in coning angle is evident in both *A. ginnala* and *A. floridanum*, however, *A. negundo* displays a less dramatic change in coning angle shown in the last row of **Fig.A.10**. Lateral impacts on the spine produced high coning angle rates of change $\bar{\dot{\theta}}_m = -15 \pm 18$ rad/s, but shorter recovery distances compared to other impact regions with similar high coning angle velocities, as shown in **Fig.5.2**a. Despite the relatively high angular velocity, $\bar{\dot{y}}_m = 48 \pm 26$ cm/s is comparable to the root and wing regions (**Fig.5.2**b) and the recovery distance $\bar{L} = 29 \pm 12$ cm remains short. The absence of raindrop adhesion to the spine relieves the samara from the need to shed the drop to resume autorotation and contributes to their rapid recovery.

While raindrops fell at $U+V = 433\pm40$ cm/s, drops can fall faster, sometimes exceeding[130] 900 cm/s. To address the proverbial white elephant presented by this disparity in drop speed, we perform 6 experiments with a greater release height to generate corrected impact speeds of $U + V = 782 \pm 84$ cm/s. These higher-speed impacts demonstrate that samaras do recover autorotation and do so without damage. We plot image sequences of a wingtip and nutlet impact by a high-speed drop in **Fig.A.11**. At $U + V = 820$ cm/s, an impact on a *A. ginnala* wingtip required a recovery distance of $\bar{L} = 39 \pm 21$ cm, a decrease from lower-speed impacts. The high-speed fragmenting impact depicted in **Fig.A.11**b required an $\bar{L} = 21 \pm 7$ cm, similar to those at lower speeds. We rationalize comparable and shorter recovery distances by noting the timescale of impact $\sim D/U$; the shorter contact and samara

disruption times imposed by faster drops balance their higher impact force. As discussed in Section 5.1.2, higher impact speeds are more likely to induce fragmentation, a more favorable outcome for samara recovery than an intact drop that pushes the samara.

5.1.2 Samaras shed drops to return to autorotation

Samaras recover autorotation only after separation from the impacting drop. We observe four principal means of drop shedding that can be singly witnessed or executed in series. We categorize these shedding modes as splashing, roll-off, spin-off, and slicing of the drop. We present shedding modes and their associated impact regions by plotting the recovery distance magnitude (L/S) vs the mass ratio ($m_\mathrm{s}/m_\mathrm{d}$) in **Fig.5.3**. All shedding modes occur across the entire experimental range of $m_\mathrm{d}/m_\mathrm{s}$, indicating that the occurrence of each shedding mode is more dependent on impact dynamics than the intrinsic properties of the samara-drop pair. We also observe that L/S is set by the shedding mode, indicating that the time to shed the drop is critical for a rapid return to autorotation.

We rationalize the trends plotted in **Fig.5.3** considering the momentum of the samara in the lab frame following impact and the drag impulse bringing it back to stable levitation,

$$m_\mathrm{s}\dot{y}_\mathrm{m} \sim \rho_\mathrm{a} C_\mathrm{D} A(\dot{y}_\mathrm{m} + V)^2 \tau. \tag{5.1}$$

The air density ρ_a and drag coefficent[11] C_D are effective constants, and the sum $(\dot{y}_\mathrm{m} + V)$ is representative of the airspeed past the samara as it recovers. The post impact descent velocity $\dot{y}_\mathrm{m} \sim U m_\mathrm{d}/(m_\mathrm{s} + m_\mathrm{d})$ and the recovery time $\tau \sim L/(\dot{y}_\mathrm{m} + V)$, where the shedding mode and subsequent deceleration of the samara set the prefactor for τ. In our experiments, U and V are functionally constant when compared to other impact variables. Our previous work[11] shows samaras obey allometry, such that $m_\mathrm{s} \sim A^{3/2} \sim S^3$. Removing constants and making appropriate substitutions into Eq. (5.1) yields,

$$L/S \sim \left(C\frac{m_\mathrm{s}}{m_\mathrm{d}} + 1 \right)^{-1}, \tag{5.2}$$

where $C \sim (1 + V/U)^{-1}$ is a constant for a particular shedding mode. Eq. (5.2) reveals that the naturally disturbed falling distance of a raindrop-samara is governed by m_d which is related to the terminal raindrop speed[131] (U). We fit Eq. (5.2) per shedding mode in **Fig.5.3** and find good agreement (correlation coefficient, R^2=0.74-0.92) with our data. At the hypothetical extreme of an unnaturally large drop or unnaturally small samara, the prediction in Eq. (5.2) approaches its $O(10)$ scaling prefactor, perhaps presenting a prediction failure. It is unclear if such an unnaturally minuscule samara, or another small, passive mass

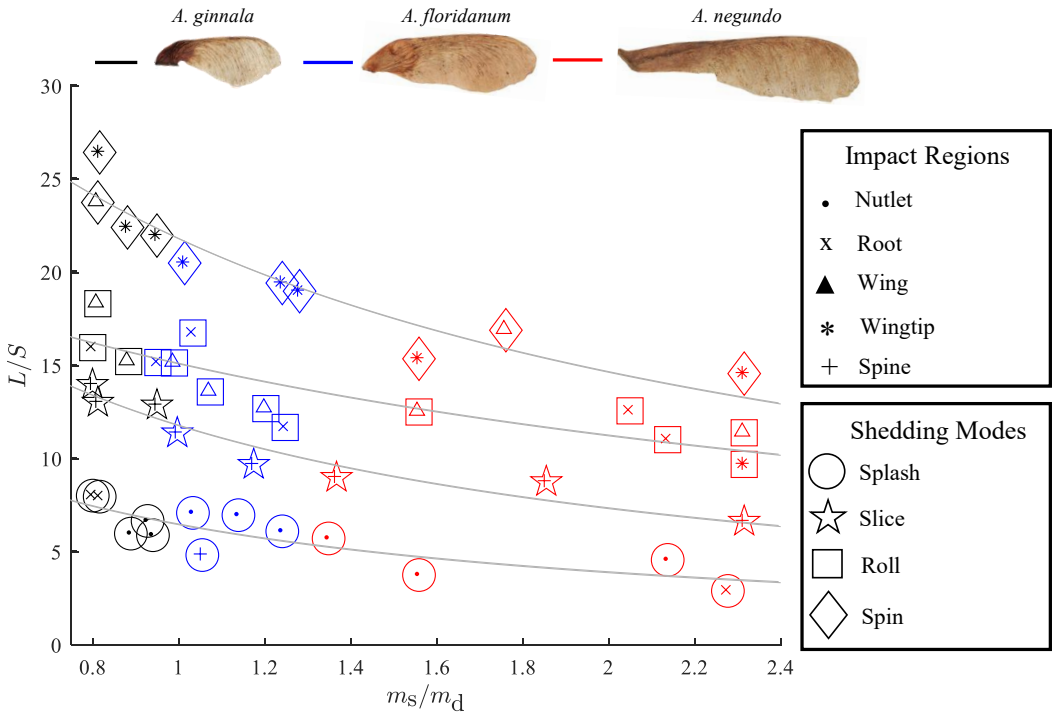

Figure 5.3: The relationship between the recovery ratio L/S and mass ratio m_d/m_s. Each data point is labeled according to the region of impact (inner symbol) and shedding mode (outline). Lines of best fit for each shedding mode are provided for visual reference only.

with a similar water repellency, could generate sufficient aerodynamic drag to separate from the raindrop[54,117,132].

Fragmentation

We define fragmentation as the breakup of the drop mass at impact via splashing or by being sliced by the samara wing. Splashing in our tests occurs only for nutlet and root impacts. In these regions, the samara is least compliant and not readily pitched. Despite the drop losing more kinetic energy during splashing than other shedding modes, L/S for splashing is the shortest, with an average recovery distance $\bar{L} = 20 \pm 10$ cm. We posit the lower L/S is a result of flight disruption that is favorable toward autorotation, namely a larger, rather than lesser, coning angle with minimal long-axis roll. Splashing also ensures a relatively shorter contact time between samara and drop. The stereotypical splashing event pictured in **Fig.5.4**a shows samara-drop contact lasting ∼10 ms. During this contact period, rotation does not stop, a characteristic of this mode seen in **Fig.5.4**b.

The theoretical boundary between pushing and splashing impacts plotted in **Fig.2**c predicts all our experimental samaras will induce raindrop splashing, but the onset of splashing is more complex than energetics can predict. Splashing is a function of drop size and speed,

surface tension σ, surface roughness, and curvature[133–138]. Samara texture, curvature, and impacts that spread beyond the surface of the samara promote fragmentation. Quetzeri-Santiago *et* al(2019) provide a simple relation for predicting the impact velocity at the onset of splashing,

$$\beta \approx \frac{2.22}{\tan\alpha}\frac{\mu_g^{1/2}(\rho D U^5)^{1/6}}{\sigma^{2/3}}, \tag{5.3}$$

where the value of $\beta \approx 0.09$ is chosen based on an initial advancing contact angle of $115 \pm 5.3°$ (Section 2.3), $\alpha = 60°$ from previous studies, and μ_g is the viscosity of air. Eq. (5.3) predicts fragmentation for $U > 268$ cm/s for vertically static samaras in our tunnel, a value that explains our observations of fragmentation. However, drops often do not fragment. Maple samaras can roll and pitch on impact, reducing the effective impact velocity below the fragmentation threshold.

A spinning samara does not always encounter drops from above and like a spinning fan, can slice a passing drop into two or more pieces, as pictured in **Fig.5.4**c. The small contact area of the drop with the samara promotes rapid shedding in 10 ± 6 ms. The collision temporarily halts autorotation, causing the wingtip to dip downward. The samara falls a distance of $\bar{L} = 31 \pm 8$ cm before regaining stable autorotative motion, as illustrated in **Fig.5.4**d. Unlike samaras that cause splashing, those slicing a drop experience a longer disruption and falling distance, which we attribute to the need for aerodynamic forces to reverse the coning angle to a positive value.

Shedding by roll and spin

Impacts onto the samara wing, do not fragment the impacting drop over the range of impact speeds we test. Non-fragmenting drops must be shed by the disparate motion of the drop and samara. Often, these impacts cause the samara to roll about its long axis, thereby yielding to the falling drop and resulting in a short contact time between the two bodies of 9 ± 2 ms. A samara roll is photographed in **Fig.5.4**e. Samaras from all three test species undergoing shedding by roll were observed to fall an average corrected distance of $\bar{L} = 50 \pm 16$ cm. The samara falls at the rolled position until resuming stable autorotation, as seen in **Fig.5.4**f.

If a drop is unable to roll a samara, likely due to impacting too near its long axis, the drop adheres to the samara wing whilst the samara tends back toward autorotation. Samara rotation imparts centrifugal forces onto the drop to break the drop-wing adhesion, an event pictured in **Fig.5.4**g. Despite the acceleration of the samara downward during impact, rotation is not interrupted, as shown in **Fig.5.4**h. These impacts generate relatively longer contact times of 270 ± 18 ms and an average recovery distance of $\bar{L} = 71 \pm 12$ cm. The samara sheds the drop when the centrifugal force exceeds the adhesive force between the

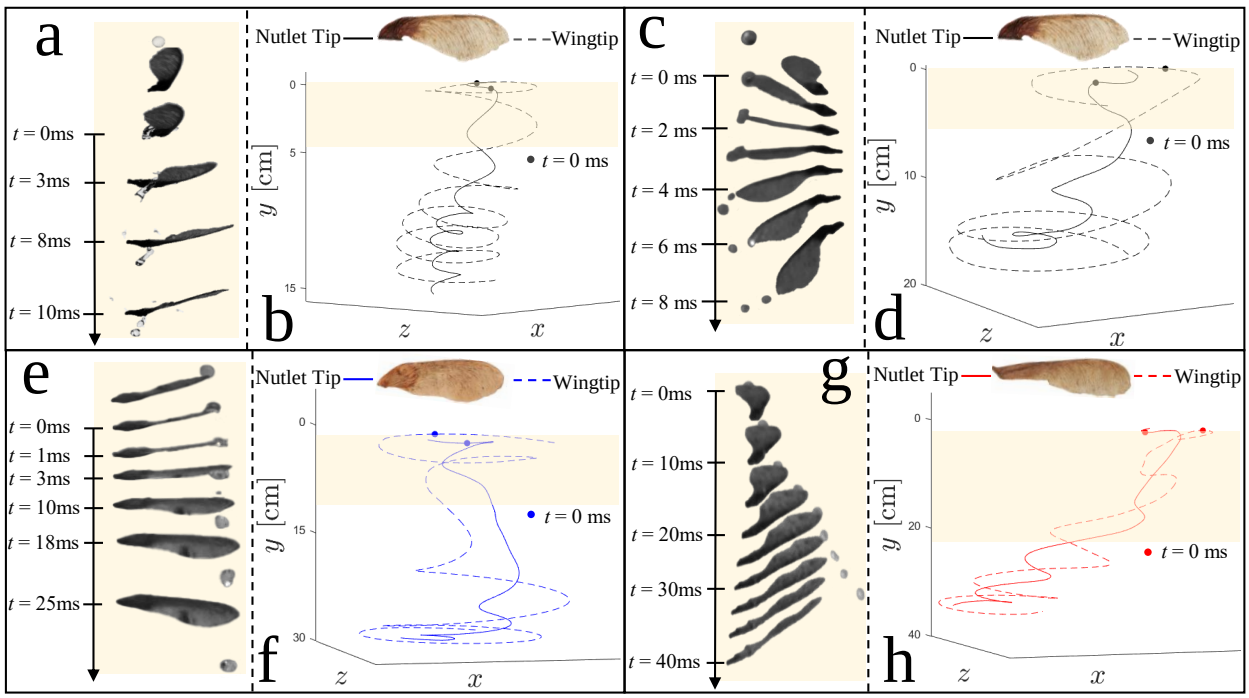

Figure 5.4: Shedding modes. Fragmentation: (a) Aggregated image sequence of an *A. ginnala* exhibiting the splashing shedding mode. (b) Three-dimensional track of the *A. ginnala* depicted in (a). The wingtip draws a larger helical path than the nutlet. Slicing: (c) Aggregated image sequence of an *A. ginnala* slicing a falling drop with the samara spine. (d) Three-dimensional track of the *A. ginnala* depicted in (c). The impact of the wing spine near the wingtip slows the wingtip to invert the samara momentarily. Shedding by samara roll. (e) Aggregated image sequence of an *A. floridanum* exhibiting the samara roll shedding mode. (f) Three-dimensional track of the *A. floridanum* depicted in (e). The raindrop impact flattens the coning angle and slows autorotation. Shedding by samara spin: (g) Aggregated image sequence of an *A negundo* samara shedding a drop via centrifugal acceleration. (h) Three-dimensional track of the *A. negundo* depicted in (g). Shedding the drop centrifugally creates the greatest vertical displacement before drop shedding. The shaded regions in the plots correspond to the image sequences.

drop and the samara,

$$\omega > \sqrt{\frac{15.12\sigma \cos\theta_e}{\rho D^2 S}} \tag{5.4}$$

where ρ is density of water, σ is the surface tension of water , and θ_e is the equilibrium contact angle. If we assume the drop sits a distance $S/2$ from the axis of rotation and the drop atop the is hemispherical, Eq. (5.4) predicts $\omega > 6.3 - 8.4$ rad/s to shed the drop. We measure the rotation rate to expel drops to be $\omega > 7.9 - 12.1$ rad/s.

Sessile drops

Samaras released from their parent tree are subject to environmental moisture such as rain and dewfall before release, much like similarly sized natural flyers[54,116,117,139] and gliders. We recreate this scenario by placing drops onto various parts of the samara—nutlet, root, wing, and wingtip—and releasing the samaras into the wind tunnel. All test samaras are able to shed deposited drops and initiate autorotation. The distance each samara falls before shedding the drop is shown in **Fig.A.12**. Surprisingly, drops placed closest to the axis of rotation are shed most quickly, highlighting the importance of mass distribution on the rotation dynamics in the first moments of flight.

5.1.3 Probability of impact

The influence of rainfall on samara dispersal is incomplete without a notion of how often raindrop impacts on descending samaras occur. Impacts are probabilistic and are informed by rainfall distribution, samara size, and time in flight. Below we present a probability model that is readily adapted to autorotating or otherwise descending seeds of any permutation across a broad range of precipitation conditions. Our model demonstrates that samaras released from the tallest trees in moderate to heavy rainfall are very likely to encounter a falling raindrop.

A raindrop may impact a samara from above or "sliced" by the leading edge of a rotating samara. The total probability of either interaction can be expressed as

$$P = P_1 + P_2 - P_1 P_2, \tag{5.5}$$

where P_1 is the probability of a raindrop impacting the samara from above, and P_2 is the probability of the samara slicing a raindrop.

The plan view impact area $A_{\text{imp},1}$ is the area occupied by the autorotating samara that if the center of mass of a raindrop were to pass an impact would result, shown in **Fig.5.5**a:

$$A_{\text{imp},1} = (A + pD)\cos\theta \approx (A + 2SD)\cos\theta, \tag{5.6}$$

where the samara perimeter $p \approx 2S$. The average time interval between raindrops passing through $A_{\text{imp},1}$ for a given rainfall intensity I is

$$\bar{t}_1 = \frac{V}{I A_{\text{imp},1}}, \tag{5.7}$$

where $V = \pi D^3/6$ is the volume of the average raindrop with an associated I. The ratio of

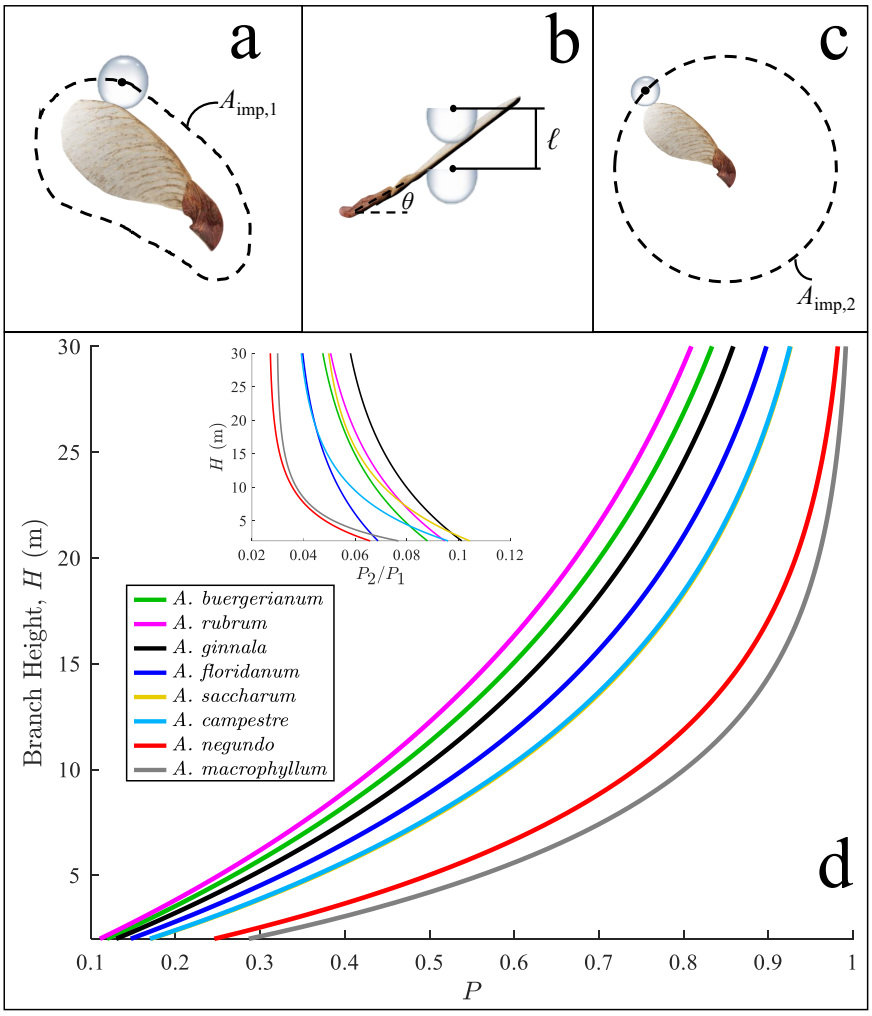

Figure 5.5: Samara impact regions for (a) impacts from above (b) l for determining τ (c) slice impacts. (d) Probability of raindrop impact onto a samara for increasing branch heights with fixed $I = 7.5$ mm/hr and $D = 3.88$mm. (inset) Probability ratio $P2/P1$ for increasing heights H.

flight times between raindrop and samara $\bar{t}$ provided a rate parameter,

$$\lambda_1 = \frac{H}{V\bar{t}_1}. \tag{5.8}$$

From Poisson's equation, the probability of at least one impact from above is given by

$$P_1 = 1 - e^{-\lambda_1}. \tag{5.9}$$

Drops sliced by the samara must occupy a volume that can be impacted by the rotating wing. To simplify the calculation of P_2, we assume no lateral drift of the samara and define the relative velocity between falling drop and samara as $\breve{V} = U - V$. We assume that only

the bottom of the drop can be struck, as once the drop passes its halfway point, it will no longer occupy a volume that can be intersected by the rotating wing–as it falls away too quickly. The time the samara resides in the slice zone is

$$\psi = l/\breve{V} = \frac{D(\tan\theta + 1)}{2\breve{V}}, \tag{5.10}$$

where ℓ is depicted in **Fig.5.5**b. The samara slices through the slice zone every $T = 2\pi\omega^{-1}$ s, where ω is the angular velocity of the samara. The probability a drop will fall in reach of a slicing samara is defined similarly to P_1, but with a modified impact area shown in **Fig.5.5**c,

$$A_{\text{imp},2} = \pi\left(S\cos\theta + \frac{D}{2}\right)^2. \tag{5.11}$$

Thus, a rate parameter for a slice is $\lambda_2 = H/(V\bar{t}_2)$, where $\bar{t}_2 = \breve{V}/(IA_{\text{imp},2})$. The probability of a slice is

$$P_2 = \frac{\psi}{T}\left(1 - e^{-\lambda_2}\right). \tag{5.12}$$

We plot P versus H in **Fig.5.5**d, with a fixed $D = 3.8$ mm, $U = 50$ cm/s, and $I = 7.5$ mm/hr and samara characteristic values A, S, θ, and V_{d} taken from literature[11]. While rain has a vast array of intensities and drop size distributions,[140] our model demonstrates that samaras dispersing in heavy storms are not unlikely to be struck by rain. There are no intersecting curves in **Fig.5.5**c, indicating that the sorting of probability curves at any H is set by A, and to a lesser degree, V. As branch height increases, the variation in P between the smallest and largest samaras widens. As branch height increases beyond what natural trees exhibit, all probability curves asymptotically approach unity. For the rainfall conditions assumed in **Fig.5.5**c, the branch height that produces the most discrepancy across samara size is 9.92 m. While impact probability increases with H, our probability model indicates that morphological characteristics of samaras at they relate to raindrop impacts become less critical for the tallest trees. The ratio of $P_2/P_1 = 0.04 - 0.11$ indicates that the probability of impact from above is higher than a slice, seen in **Fig.5.5**e. Species with higher ratios[11] like *A. floridanum*, *A. negundo*, and *A. macrophyllum* are significantly more likely to experience overhead impacts compared to slice impacts, a direct correlation to their larger wing structures.

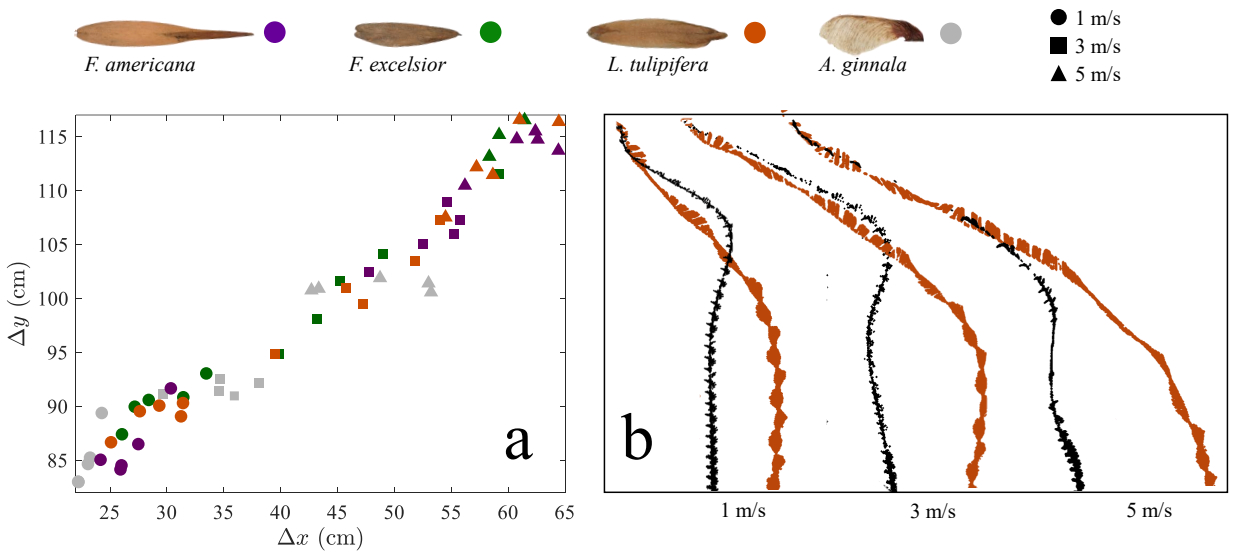

Figure 5.6: **(a)** Lateral displacement Δx versus vertical displacement Δy for all samaras at wind speeds of 1 m/s, 3 m/s, and 5 m/s. **(b)** Representative tracked movement paths of samaras at each wind speed, illustrating increased lateral drift and reduced vertical fall with stronger crossflow. *A. ginnala* samaras are in black while *L. tulipifera* samaras in orange.

5.2 Rolling samara response to a concentrated crosswind

The present study investigates kinematic and aerodynamic responses of rolling samaras falling through lateral gusts. We quantify crosswind-driven changes in rolling-samara kinematics and transport, integrate empirical measurements into dispersal distributions, and compare outcomes with autorotating *Acer* samaras. Controlled experiments at crosswind speeds $U = 1, 3, 5\ \mathrm{m\,s^{-1}}$ observed with high-speed tracking yield detailed measures of lateral and vertical motion, trajectory tilt, projected area, and drag characteristics during flight.

We investigate the aerodynamic response of rolling samaras from three species—*F. americana*, *F. excelsior*, and *L. tulipifera*—to concentrated lateral wind disturbances. Each species is experimentally represented by 10 samaras, with three replicate flights recorded under both still-air and crosswind conditions. In still air, all specimens roll about their spanwise axis[69] while helically processing downward, maintaining steady descent characterized by periodic oscillations in wing orientation and angle of attack. When exposed to crosswind, samaras experience transient aerodynamic perturbations, leading to changes in trajectory, roll frequency, and lateral displacement. We present detailed kinematic and morphological analyses to quantify crosswind-induced responses across species by measuring lateral displacement, drift angle, and the time and distance required for re-stabilization of the descent trajectory.

We track the position of five rolling samaras from *F. americana*, *F. excelsior*, and *T. tulipifera*, and five non-rolling samaras from *A. ginnala*, exposed to a steady, laminar crosswind. All samaras exhibit stable autorotation prior to crosswind exposure. We define stable descent as motion during which the vertical velocity varies by less than 5% over a 0.5-second interval, and the rotational axis remains within $\pm 10^\circ$ of the mean coning angle for a duration spanning at least three full revolutions. Our laboratory crosswind pushes samaras laterally Δx, measured by averaging the x-positions of the nutlet and wingtip before entering and after exiting the lateral jet.To operationally define the onset of lateral drift, we identify the interval during which the center-of-mass trajectory shows a net lateral displacement exceeding $3S/4$, where S is the wingspan of the samara. Using this threshold provides a consistent reference point for measuring displacement, even without precise knowledge of the horizontal extent of the crosswind jet. The threshold is selected to surpass the typical processional oscillations, thereby indicating a sustained drift rather than oscillatory motion. The endpoint of Δx is defined as the point where lateral drift falls below $3S/4$, marking the return to stable, vertical autorotation.

We plot Δx versus Δy, the vertical distance traveled while exposed to the lateral jet, for all samaras released into three different jet speeds in **Fig.5.6**a. At a jet speed U of 1 m/s, *A. ginnala* samaras exhibit horizontal displacements of $\Delta x \approx 20$–$25\,\text{cm}$ with vertical descent distances of $\Delta y < 90\,\text{cm}$. In contrast, rolling samaras descend to $\Delta y \approx 85$–$90\,\text{cm}$ while reaching $\Delta x \approx 25$–$35\,\text{cm}$. *A. ginnala* samaras descend along trajectories tilted more than 10° from vertical and exhibit minimal lateral drift ($\Delta x < 25\,\text{cm}$), whereas rolling samaras follow arcing center-of-mass trajectories that gradually deviate laterally, reaching displacements of up to $\Delta x > 40\,\text{cm}$, as shown in **Fig.5.6**b.

As crosswind speed increases to 3 m/s, horizontal displacement increases across all species to $\Delta x \approx 35$–$55\,\text{cm}$, while vertical descent distances remain similar, $\Delta y \approx 90$–$110\,\text{cm}$. *A. ginnala* samaras exhibit horizontal displacements of $\Delta x \approx 30$–$40\,\text{cm}$ and vertical descent distances of $\Delta y \approx 90$–$95\,\text{cm}$. Rolling samaras exhibit horizontal displacements of $\Delta x \approx 35$–$50\,\text{cm}$ and vertical descent distances of $\Delta y \approx 95$–$110\,\text{cm}$. Interspecific differences in descent response become more pronounced at this crosswind speed. *A. ginnala* samaras descend only slightly farther than they do at 1 m/s, resulting in modest increases in both lateral and vertical displacement. In contrast, rolling samaras continue to travel laterally while descending more steeply, following arcing trajectories, as illustrated in **Fig.5.6**b.

At a crosswind speed of 5 m/s, horizontal displacement increases across all species, with rolling samaras reaching $\Delta x \approx 55$–$65\,\text{cm}$. Vertical descent distances also increase for rolling samaras, ranging from $\Delta y \approx 112$–$128\,\text{cm}$. Interspecific differences are most pronounced at this wind speed. *A. ginnala* samaras exhibit shallower vertical descent, with $\Delta y \approx 105 \pm 5\,\text{cm}$,

and reach lower horizontal displacements of $\Delta x \approx 40$–$55\,\mathrm{cm}$. Under higher wind speeds, *Acer* samaras exhibit slightly increased vertical travel distances $\Delta y \approx 90\,\mathrm{cm}$ but maintain relatively straight and vertical trajectories, with tilt angles less than 10° and lateral-to-vertical displacement ratios $\Delta x/\Delta y < 0.35$. In contrast, rolling samaras continue to drift laterally as they descend, following more arcing trajectories characterized by larger tilt angles (up to 25°) and higher displacement ratios ($\Delta x/\Delta y > 0.45$), as shown in **Fig.5.6**b.

We adopt the dimensionless ratio U/v_{tip} to classify aerodynamic regimes, where U is the crosswind velocity and $v_{\mathrm{tip}} = \omega_p S \cos\theta$ represents the axial tip speed of the samara wing—defined as the linear velocity of the wingtip. The formulation builds on the framework introduced by Niu et al.[14]. Experimental wind speeds of 1, 3, and 5 m/s are selected to span the inertia-dominated regime ($U/v_{\mathrm{tip}} < 1$), transitional regime ($U/v_{\mathrm{tip}} \approx 1$), and crosswind-dominated regime ($U/v_{\mathrm{tip}} > 1$).

The relationship between U/v_{tip} and the displacement ratio $\Delta x/\Delta y$ for all samaras is shown in **Fig.5.7**a. The displacement ratio $\Delta x/\Delta y$ describes the net trajectory slope in the x–y plane, expressing lateral displacement relative to vertical fall distance. The relationship between the dimensionless tip speed ratio U/v_{tip} and the lateral-to-vertical displacement ratio $\Delta x/\Delta y$ is shown in **Fig.5.7**a. The displacement ratio does not exceed unity. In the inertia-dominated regime, defined by $v_{\mathrm{tip}} \gg U$, samaras maintain displacement ratios $\Delta x/\Delta y \approx 0.30$. All samaras under 1-m/s crosswind and *A. ginnala* experiencing 3-m/s lie within the inertial regime.

When the crosswind exceeds the tip velocity ($U/v_{\mathrm{tip}} > 1$), the combined flow experienced by the samara becomes increasingly oblique, tilting away from vertical. The lift vector adjusts accordingly, increasing its lateral component and enhancing crosswind-induced drift. Within the intermediate range $1 < U/v_{\mathrm{tip}} < 2$, the displacement ratio increases to $\Delta x/\Delta y \approx 0.40$–$0.50$ across species. Under these conditions, samaras from *A. ginnala* at 5 m/s and rolling samaras at 3 m/s exhibit lateral-to-vertical displacement ratios within the observed range of $\Delta x/\Delta y \approx 0.40$–$0.50$. When the crosswind exceeds twice the tip velocity ($U/v_{\mathrm{tip}} > 2$), lateral forces dominate, producing the highest observed displacement ratios of $\Delta x/\Delta y > 0.5$, particularly in rolling samaras. Previous experiments on *Acer* samaras subjected to concentrated gusts reported significant drift, stalling, and tumbling behaviors[14]. Such instabilities primarily occurred when $U/v_{\mathrm{tip}} > 1.6$, where crosswind loading overwhelms autorotation and inhibits passive recovery. In contrast, rolling samaras in our experiments exhibited large lateral excursions under high wind speeds while maintaining coherent rotation.

Rolling samaras autorotate while also undergoing spanwise rotation along their longitudinal axis[33]. We define the edge velocity v_{edge} as the combined effect of autorotation and

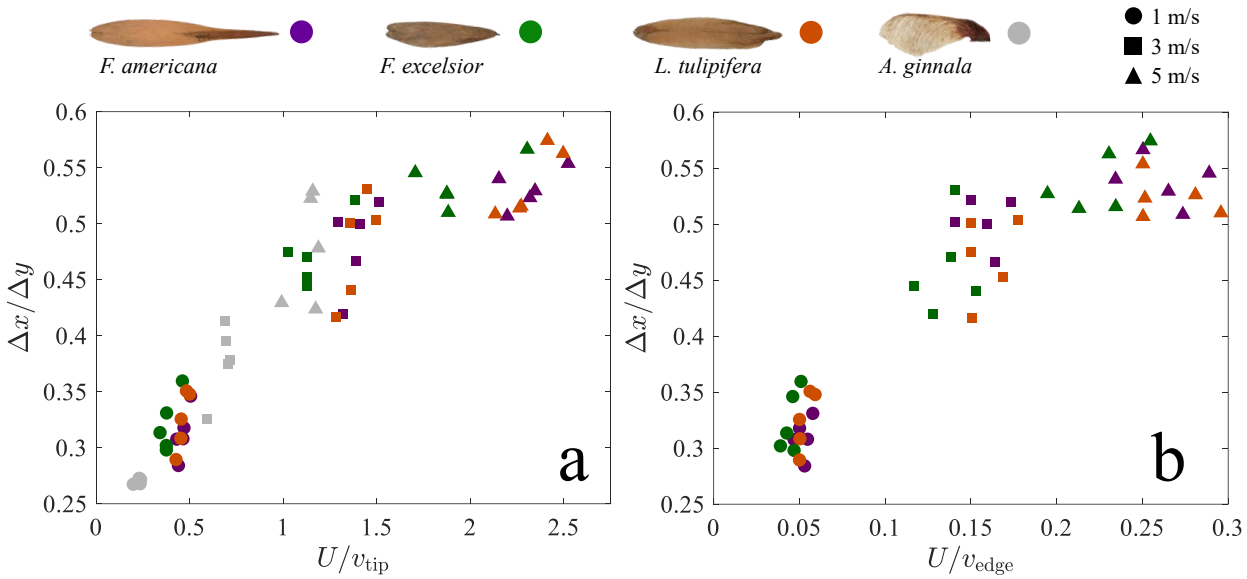

Figure 5.7: $\Delta x/\Delta y$ vs the tip-speed-normalized crosswind velocity. In **(a)** tip speed v_{tip} is based on precessional rotation, and in **(b)** tip speed v_{edge} is based on rolling rotation.

rolling motion, given by $v_{\text{edge}} = \omega_p S \cos\theta + \omega_r c/2$ where S is the span, c is the chord length, and θ is the coning angle. The first term represents the tip speed from autorotation, while the second accounts for edge motion induced by rolling about the spanwise axis.

The relationship between this rolling-based edge velocity and crosswind forcing is shown in **Fig.5.7**b. When v_{edge} is used in place of autorotational tip speed, all samaras remain within the inertia-dominated regime $U/v_{\text{edge}} < 1$ across all tested wind speeds. Extrapolation indicates that wind speeds exceeding 10 m/s would be required to reach transitional aerodynamic behavior, and speeds above 20 m/s would be needed to enter a crosswind-dominated regime. Even at the maximum wind speed tested in our tunnel 22 m/s, no drop mode or autorotational breakdown is observed in rolling samaras (see Supplemental M1).

5.2.1 Crosswind tilts and stretches the helical samara path

Rolling samaras descend through a combination of spanwise rotation and azimuthal precession. The center of mass follows an approximately helical path, similar to that of freely falling parallelograms[37] and *Acer* samaras. In still air, the axis of precession aligns with gravity, producing a vertically oriented helix described by

$$\vec{r}(t) = \begin{bmatrix} \alpha S \sin(\theta)\cos(\omega_p t) \\ \alpha S \sin(\theta)\sin(\omega_p t) \\ V_y t \end{bmatrix}, \tag{5.13}$$

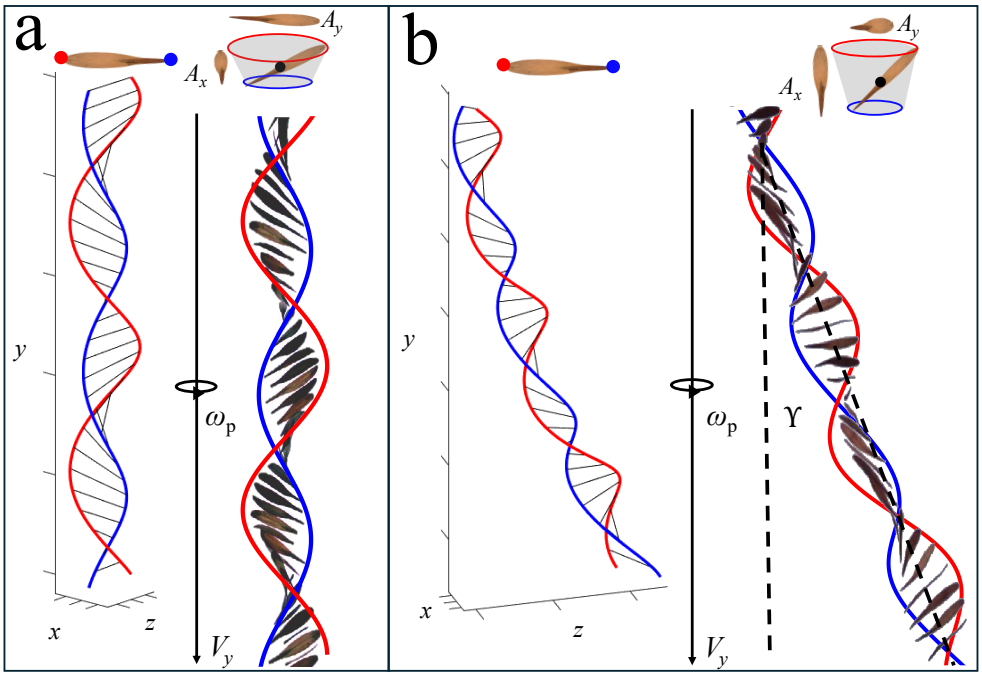

Figure 5.8: Comparison of helical trajectories for rolling samaras in still air and under crosswind. **(a)** In still air, the center of mass follows a vertically oriented helix with consistent lateral amplitude R, precession rate ω_p, and descent velocity V_y. **(b)** Under crosswind, the helix tilts by an angle γ, increasing lateral drift while modifying precession symmetry. Blue and red curves mark tracked spanwise extremities. Insets show top and side views of the samara and the tracked endpoints.

where ω_p is the precession frequency, V_y is the vertical descent velocity, S is the wing span, and θ is the coning angle[11]. The parameter α denotes the spanwise location of the center of rotation from the nutlet, typically between 0.3 and 0.5 depending on species-specific morphology[33,141]. A representative vertical helical trajectory is shown in **Fig.5.8**a.

In the presence of crosswind, the precession axis tilts away from vertical by an angle γ, resulting in lateral drift of the center of mass. The tilt angle is estimated from trajectory data as

$$\gamma = \tan^{-1}\left(\frac{\Delta x}{\Delta y}\right). \tag{5.14}$$

To account for crosswind-induced reorientation, the helical model is modified by rotating the trajectory about the x-axis by γ. The resulting path becomes

$$\vec{r}_U(t) = \begin{bmatrix} \alpha S \sin(\theta_U)\cos(\omega_{p,U}t) \\ \alpha S \sin(\theta_U)\sin(\omega_{p,U}t)\cos(\gamma) - V_{y,U}t\sin(\gamma) \\ \alpha S \sin(\theta_U)\sin(\omega_{p,U}t)\sin(\gamma) + V_{y,U}t\cos(\gamma) \end{bmatrix}, \tag{5.15}$$

where θ_U, $\omega_{p,U}$, and $V_{y,U}$ denote the coning angle, precession frequency, and descent speed under crosswind conditions. A representative crosswind trajectory is shown in **Fig.5.8**b.

The reorientation of the descent trajectory under crosswind modifies the structure of the helical path by stretching it and changing key kinematic quantities. Vertical descent speed V_y increases, precession frequency ω_p decreases, and coning angle θ widens. Kinematic variables measured under crosswind are denoted with subscript U. A lateral Reynolds number is defined as $Re_U = \rho US/\mu$, where ρ is the air density and μ is the dynamic viscosity of air. The tilt angle γ increases systematically with Re_U, rising from roughly 0.25–0.4 rad at $Re_U \approx 2{,}000$ to nearly 1 rad at $Re_U \approx 10{,}000$, as shown in **Fig.5.9**a. Low Re_U values correspond to minimal reorientation, intermediate values (4,000–8,000) show steady growth in tilt, and the largest values suggest a plateau that may be limited by geometric stability or the balance between lateral and vertical drag. Because Re_U scales directly with crosswind speed, the observed trend confirms that stronger crosswinds tilt the descent axis, producing arcing trajectories, greater lateral displacement, and faster descent.

The ratio θ_U/θ increases with tilt γ, showing a tightening of the helical cone as the path reorients away from vertical, as shown in **Fig.5.9**b. An analogous response occurs in parachutes, where partially restricting the lower edge of the canopy during flight draws the perimeter inward, steepens the cone, and reduces the effective flare radius[142,143]. Supersonic parachute studies further show that the angle of the inflated cone and its projected area decrease as flow intensity increases, and partial collapses often initiate at the lower edge[142], both behaviors consistent with a cone that tightens under greater lateral forces. Computational fluid–structure interaction simulations confirm that the geometry of the inflated cone is highly sensitive to the degree of restriction at the lower edge[143], providing a direct physical analogy for the observed rise in θ_U/θ at larger γ.

The ratio $\omega_{p,U}/\omega_p$ decreases with increasing γ, showing that precessional motion slows as the trajectory becomes more tilted, as shown in **Fig.5.9**c. At low tilt, precession remains relatively stable, but beyond $\gamma \approx 0.4$ a marked reduction occurs, particularly for trials with the largest tilts. Similar to the mass-alteration experiments in[11], where more rapidly rotating samaras descended with a flatter cone angle, the reduced precessional velocity here corresponds to a tightening of the helical cone as shown in **Fig.5.9**b. In both cases, changes in angular motion alter the coning geometry in a way that influences descent stability and aerodynamic performance. The slowdown in precession at high tilt not only compresses the cone but also suppresses the azimuthal sweeping motion, reducing the stabilizing effects of precession.

Samaras descend more rapidly under crosswind and with increasing tilt angle γ, as shown in **Fig.5.9**d. The increase in vertical speed is consistent with the geometric tightening of the cone as shown in **Fig.5.9**b. The reduction in precessional velocity, both of which limit the ability of the wing to maintain a large vertical drag area as shown in **Fig.5.9**c. Tilting

the cone reorients the lift vector away from opposing gravity.

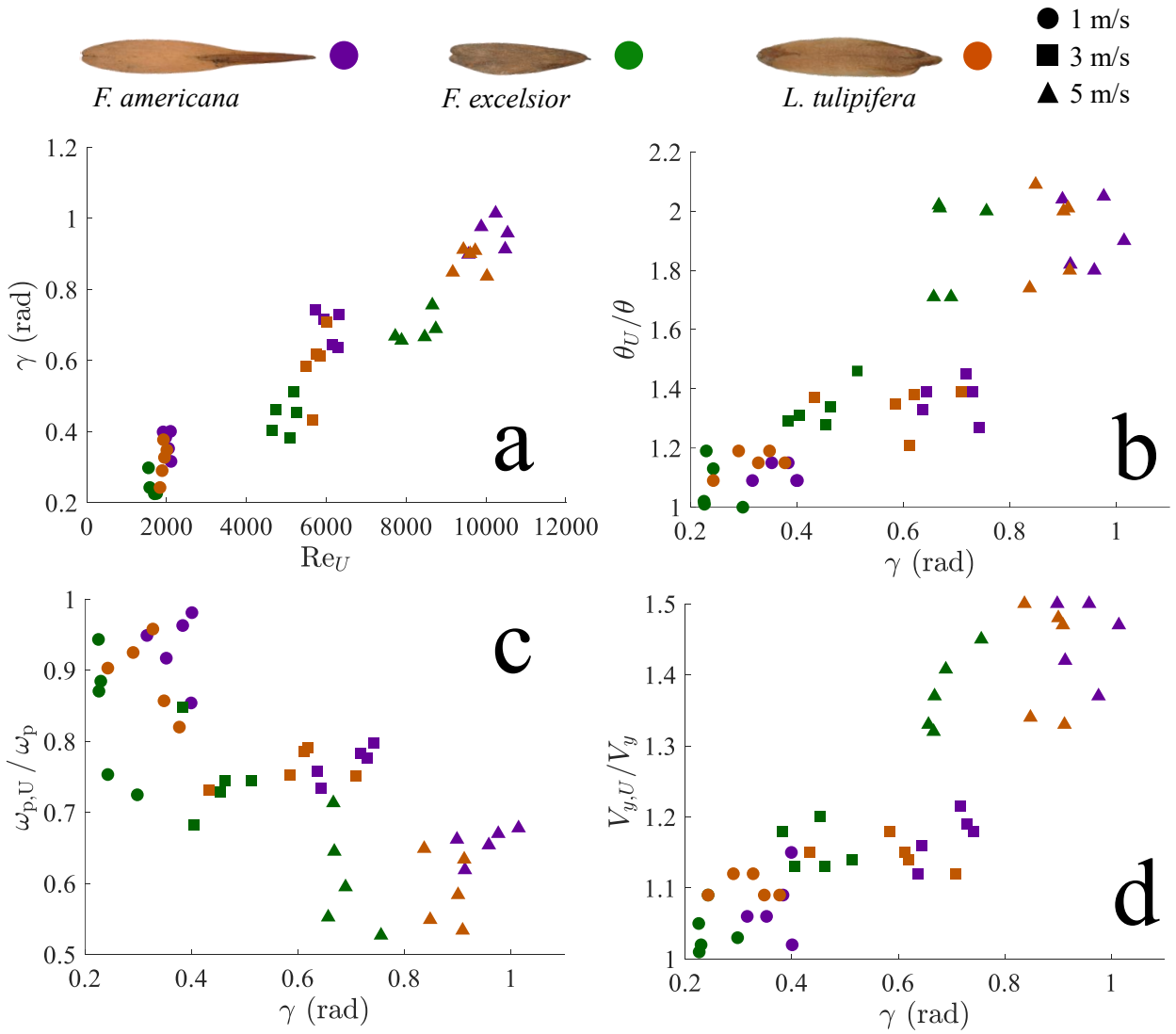

Figure 5.9: Crosswind-induced tilt and its influence on samara descent kinematics across species and wind speeds. (a) Crosswind-based Reynolds number Re_U versus tilt angle γ. (b) Coning angle ratio θ_U/θ versus tilt angle γ. (c) Precession frequency ratio $\omega_{p,U}/\omega_\mathrm{p}$ versus tilt angle γ. (d) Vertical descent velocity ratio $V_{y,U}/V_y$ versus tilt angle γ.

Helix geometry determines both the balance of vertical and lateral center of mass velocity components and the magnitude of spanwise rolling. Rolling samaras act as passive energy converters, transforming gravitational potential energy into translational motion of the center of mass and spanwise rotation about the longitudinal axis. The relative partitioning between these modes is set by the helix geometry and further influenced by crosswind through its effects on descent speed, precession rate, and cone angle. Expressing the motion in terms of kinetic energy provides a quantitative framework for assessing how crosswind alters the

fraction of gravitational energy retained in mechanical motion versus dissipated through aerodynamic interactions.

The total kinetic energy per unit mass in steady descent is given by

$$ke = \frac{1}{2}\left(\left\|\frac{d\vec{r}}{dt}\right\|^2 + \frac{I\omega_r^2}{m}\right), \tag{5.16}$$

where $\frac{d\vec{r}}{dt}$ is the instantaneous velocity of the center of mass derived from the helical trajectory, I is the moment of inertia about the spanwise axis as defined in Schaeffer et al.[69], and ω_r. The helical path $\vec{r}(t)$ captures only the center of mass motion and does not account for rolling energy, necessitating the inclusion of the $I\omega_r^2/2$ term. Total kinetic energy per unit mass of samaras decreases with increasing Reynolds number based on crosswind velocity, indicating that despite greater lateral forcing, the energy retained in translational and rotational motion becomes increasingly constrained at high Re_U values as shown in **Fig.5.10**a.

The difference between a hypothetical maximum energy, defined as the sum of still air kinetic energy and the translational energy the samara would adopt if it were traveling at the crosswind speed, and the observed kinetic energy during crosswind descent is given by

$$\Delta ke = \underbrace{\frac{1}{2}\left(\left\|\frac{d\vec{r}}{dt}\right\|^2 + \frac{I\omega_r^2}{m}\right) + \frac{U^2}{2}}_{\text{Theoretical Maximum}} - \underbrace{\frac{1}{2}\left(\left\|\frac{d\vec{r_U}}{dt}\right\|^2 + \frac{I\omega_{r,U}^2}{m}\right)}_{\text{Measured}}. \tag{5.17}$$

We plot the difference Δke against Re_U in **Fig.5.10**b. The gap between the theoretical maximum and actual energy grows substantially with Reynolds number, revealing that samaras extract a diminishing fraction of available energy under strong crosswind.

Although the center of mass trajectory $\vec{r}(t)$ captures geometric features of the descent, it does not encode information about the surface area A, which governs aerodynamic drag. Crossflow reorients the surfaces exposed to aerodynamic forces. To approximate the projected areas that modulate lateral and vertical forces, analytical expressions are used. The lateral projected area, normal to the crosswind direction and averaged over a full precessional cycle, is given by

$$A_x = \frac{A\sin(\theta_U)}{2}\cos(\gamma) + \frac{A\cos(\theta_U)}{2}\sin(\gamma), \tag{5.18}$$

and the vertical projected area becomes

$$A_y = \frac{A\cos(\theta_U)}{2}\cos(\gamma) + \frac{A\sin(\theta_U)}{2}\sin(\gamma). \tag{5.19}$$

The expressions depend on the coning angle θ and crosswind-induced tilt γ, but must be

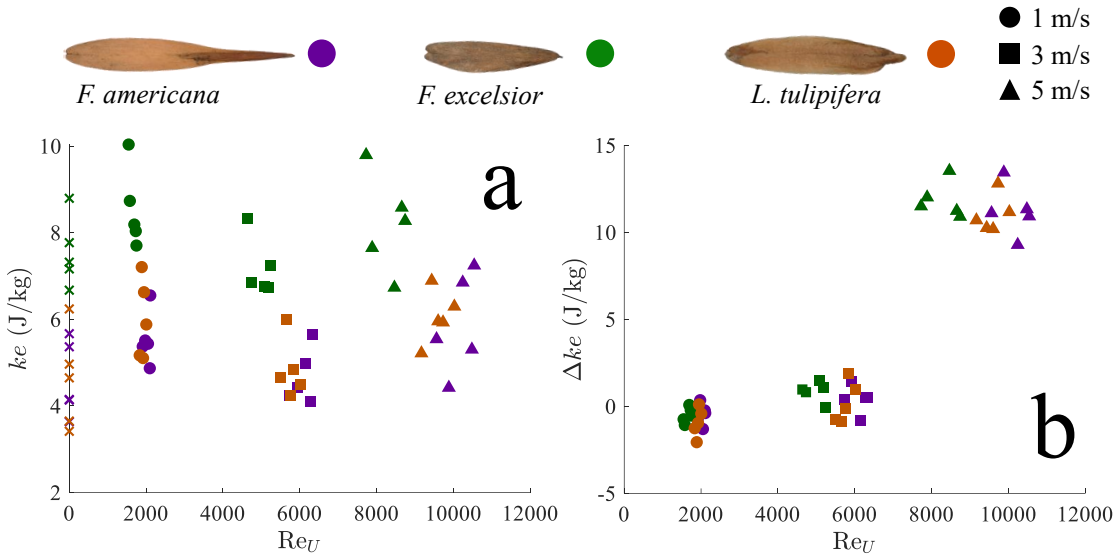

Figure 5.10: Total kinetic energy potential of samaras across crosswind conditions. (a) Kinetic energy per unit mass ke, and (b) the difference between a theoretical maximum and observed kinetic energy Δke versus Re_U.

specified independently of $\vec{r}(t)$, since $\vec{r}(t)$ is agnostic of surface orientation.

The projected areas are used to estimate the aerodynamic drag coefficients in the vertical and lateral directions. The vertical drag coefficient under crosswind is expressed as

$$C_{D,y} = \frac{2mg}{\rho V_y^2 A_y}, \tag{5.20}$$

where V_y is the vertical descent velocity, ρ is air density, and A_y is the vertically projected area. The lateral drag coefficient is computed from observed lateral displacement Δx as

$$C_{D,x} = \frac{2m\Delta x}{\rho U^2 A_x \tau^2}, \tag{5.21}$$

where U is the crosswind speed and $\tau = L/V_y$ is the descent time over jet thickness L.

Aerodynamic drag has been discussed in previous studies of seed descent, where *Acer* samaras are often modeled as blunt bodies to characterize their terminal velocity and lift production[11,34,39]. Revisiting this framework for rolling samaras enables direct comparison of vertical drag performance between rolling and *Acer* samaras. Experimental measurements of rolling samaras under still-air conditions support the formulation of a vertical drag coefficient $C_{D,y} \approx 7.02$, with a coefficient of determination $R^2 = 0.77$, as shown in **Fig.5.11**a. *Acer* samaras, included for comparison using data from[11], fall below the rolling trendline, consistent with their lower mean drag coefficient $C_{D,y} \approx 5.99$.

Building on these still-air measurements, we examine how vertical and lateral drag coefficients evolve with crosswind-induced changes in descent behavior. Vertical drag coefficients $C_{D,y}$ decline sharply with increasing Reynolds number, dropping from values above 4 at low Re_U to below 2 at high Re_U as shown in **Fig.5.11**b. Lateral drag coefficients $C_{D,x}$, computed from lateral displacement data, exhibit a similar decline with Reynolds number. Although lateral drag remains consistently lower than its vertical counterpart, the reduction in $C_{D,x}$ reflects the shrinking projected area normal to the wind as tilt increases **Fig.5.11**c. The ratio $C_{D,x}/C_{D,y}$ provides a clearer view of this aerodynamic reorientation as shown in **Fig.5.11**d. At low Re_U, samaras experience relatively balanced lateral and vertical forces, with drag coefficient ratios near unity. The ability to take advantage of crosswind diminishes as crosswind speed increases, and the necessity for such advantage becomes less critical since higher wind speeds inherently can carry samaras further from the parent tree. Further, high winds are also associated with updrafts that keep samaras aloft[144].

Rolling samaras exhibit a remarkable ability to maintain steady rotation at crosswind speeds that cause drop-out of *Acer* samaras. Sustained rotation under these conditions may take precedence over achieving maximum lateral displacement, particularly at high Re_U where unsteady motion could induce tumbling. The reduction in energy capture from crosswind at high speeds suggests that rolling samaras are tuned less for exploiting extreme gusts and more for consistent performance in variable flow environments. Although crosswind tilting increases lateral displacement, that advantage is offset by faster descent caused by cone tightening and reduced precession, which produces diminishing returns in dispersal distance at high Re_U. Consequently, dispersal distance likely peaks at intermediate wind speeds, creating a non-linear relationship between dispersal range and wind speed similar to predictions from micrometeorological models of wind dispersal[146]. Aerodynamic adjustments under crosswind also reshape the dispersal shadow, as increased tilt streamlines the vertical profile of descent and concentrates seeds nearer the parent tree, while turbulence increases variance in dispersal distance[147]. In contrast to samaras, plumed or parachute seeds such as dandelions that cannot do not autorotate exploit strong crosswinds by maximizing uplift[148]. Ballooning spiders and gliding insects provide another example, dispersing aerially by passively riding turbulent updrafts[149,150]. Rolling samaras instead adopt a strategy centered on maintaining reliable rotation[9].

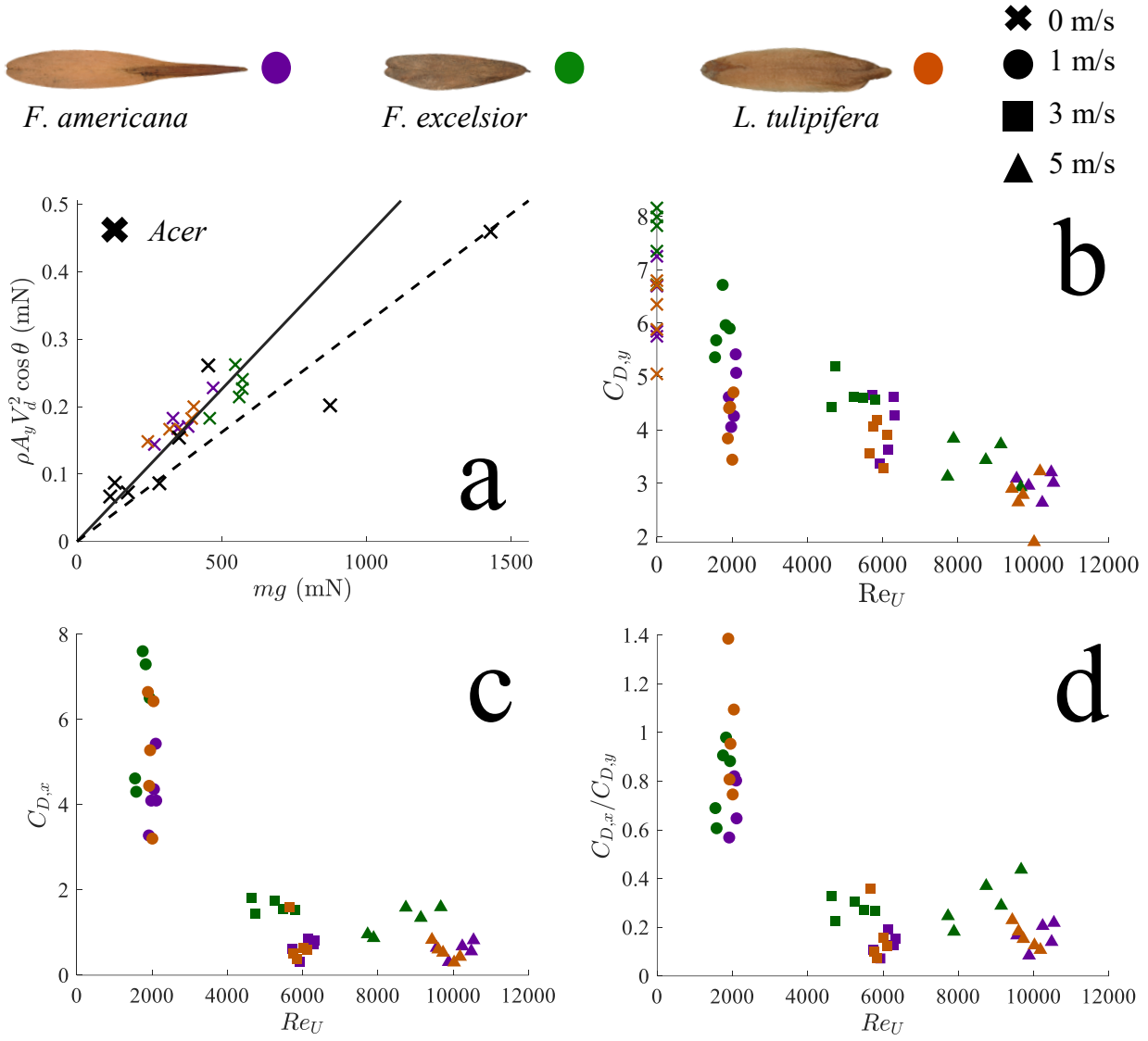

Figure 5.11: Aerodynamic drag coefficients for rolling samaras in still air and under crosswind conditions. (a) Vertical drag $C_{D,y}$ scales linearly with weight under still-air conditions, with *Acer* samaras from[11] included for comparison. (b) Vertical drag $C_{D,y}$ decreases with Re_U, indicating more streamlined vertical flow at higher wind speeds. (c) Lateral drag $C_{D,x}$ also declines with Re_U due to reductions in projected area as tilt increases. (d) The ratio $C_{D,x}/C_{D,y}$ versus Re_U.

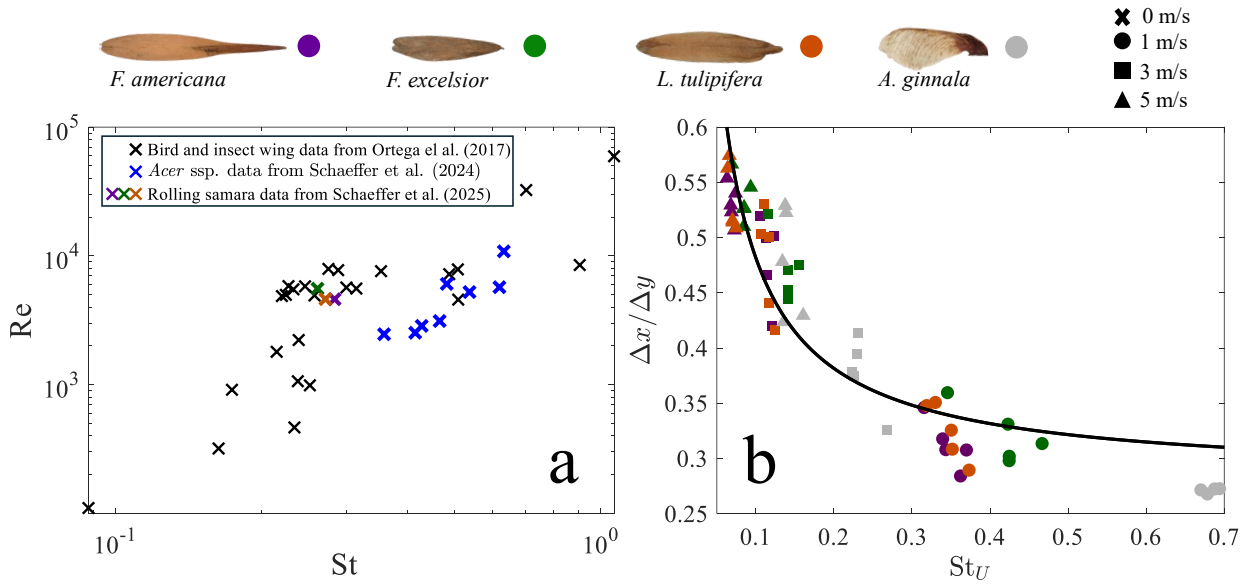

Figure 5.12: Strouhal–based scaling of samara dispersal under crosswind. (a) Still-air map of Reynolds number versus Strouhal number. Acer data is taken from Schaeffer *et al.* (2024)[11]. Rolling samara data is taken from Schaeffer *et al.* (2025)[69]. Other points represent data taken from Ortega *et al.* (2017)[145] (b) $\Delta x/\Delta y$ versus St_U. Solid line in (b) indicates the inverse trend $\Delta x/\Delta y \sim \mathrm{St}_U^{-1}$, with $R^2 = 0.84$.

5.2.2 Crosswind dispersal distance is scaled by the Strouhal number

Strouhal and Reynolds numbers provide a common framework for comparing locomotor performance across biological flyers and seeds[145,151,152]. The breadth of this framework is illustrated by studies showing that wings not primarily adapted for autorotation, such as those excised from insects and hummingbirds, can achieve stable autorotation with descent speeds comparable to samaras[145]. For autorotators, Strouhal number is expressed in terms of the rotational frequency ω_p, the projected cone radius $S\cos\theta$, and the descent velocity V_y,

$$\mathrm{St} = \frac{\omega_p S \cos\theta}{V_y}. \tag{5.22}$$

Both rolling and *Acer* samaras fall within a Strouhal range comparable to the bird and insect wing values reported by Ortega *et al.* (2017)[145]. Rolling samaras average $\mathrm{St} \approx 0.26 \pm 0.02$, whereas *Acer* samaras reach larger values of $\mathrm{St} \approx 0.85 \pm 0.06$. The higher Strouhal values of *Acer* samaras reflect their lower descent velocity and higher rotational velocity compared to rolling samaras. Strouhal values near $0.2 - 0.4$ are often linked with stable leading-edge vortices and efficient momentum exchange in locomotion, suggesting that rollers operate within a flow regime consistent with efficient lift generation[81,151]. To place these

Strouhal values in their flow-regime context, the Strouhal number can be compared with the Reynolds number Re we define following Ortega-Jiménez et al.[145] as

$$\mathrm{Re} = \frac{\rho\omega_p(Scos\theta)^2}{\mu}, \tag{5.23}$$

with ρ and μ denoting the density and viscosity of air. For our samaras, values fall in the range $\mathrm{Re} = 10^3$–10^4, overlapping the regime of many insect flyers[153]. The Strouhal–Reynolds map separates rolling samaras and *Acer* samaras, with rollers occupying lower values and *Acer* samaras remaining elevated as shown in **Fig.5.12**a. Comparison with animal and insect wings shows that, although not adapted for seed-like rotation, they occupy the same parameter space.

Still-air Strouhal characterizes quiescent kinematics, not response to crosswind. We consider the lateral and vertical velocities $V_{x,U} = \Delta x/\Delta t$ and $V_{y,U} = \Delta y/\Delta t$ in a coordinate frame moving with the rotating samara, analogous to a parcel of air encountering a fan blade that is carried by the precessional rotation. The lateral velocity is set by the ambient crosswind, $V_{x,U} \sim U$ (best fit, $V_{x,U} = 0.86U^{0.94}$, R^2=0.92). The vertical velocity accumulated over one precession cycle is controlled by the edge speed that samples the flow, $V_{y,U} \sim \omega_p S\cos\theta$. Solving for $\Delta x/\Delta y$ over one precession period the distance ratio scales as

$$\frac{\Delta x}{\Delta y} \sim \frac{V_{x,U}}{V_{y,U}} \sim \frac{U}{\omega_p S\cos\theta} = \frac{1}{\mathrm{St}_U}. \tag{5.24}$$

We plot $\Delta x/\Delta y$ vs the crosswind Strouhal St_U in **Fig.5.12**b. The inverse relation predicted by Eq. (5.24) provides an $\mathrm{R}^2 = 0.84$. Lateral transport is governed primarily by how effectively the edge samples the ambient flow relative to the imposed wind U, rather than by species-specific morphology.

Adopting the environmental velocity U in place of the still-air normalization $V_{y,U}$ captures the coherence of crosswind forcing over a precession cycle and yields a predictive, performance-based metric for $\Delta x/\Delta y$. Ecologically, the resulting inverse scaling implies proportional gains in lateral spread with increasing wind, subject to geometric or stability limits as cones tighten and ω_p adjusts with U. As a complementary view, we examined the tip-speed ratio U/v_{tip} (**Fig.5.7**a), which is the inverse of a crosswind-based Strouhal formed with the tip speed for *Acer* samaras.

5.2.3 Crosswind responsive kinematics best predict lateral spread

We are not the first to model wind-driven seed dispersal. Classic frameworks have long linked wind statistics to transport, relating wind strength to travel distance while accounting for

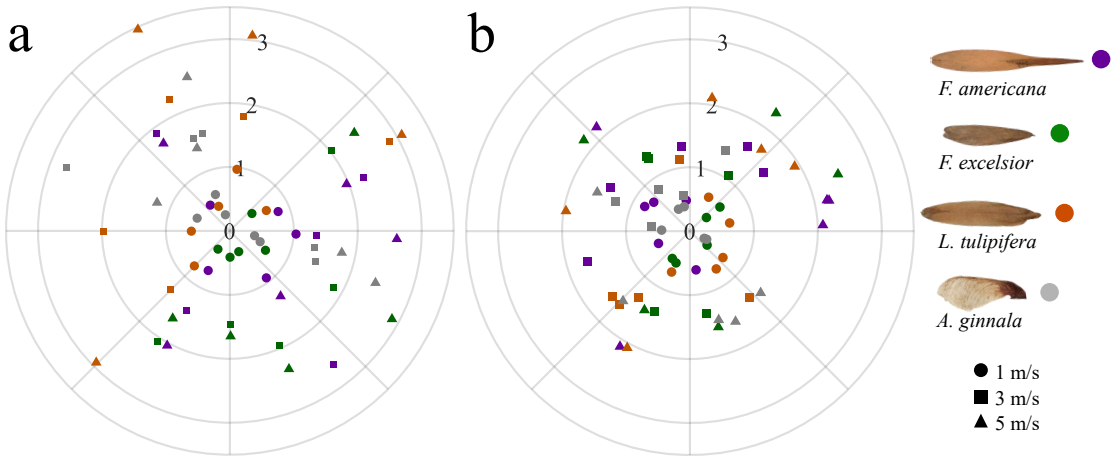

Figure 5.13: Lateral nondimensional dispersal. (a) Dispersal model including log-normal wind distribution and measured $V_{y,U}$. (b) Model including measured $V_{x,U}/V_{y,U}$.

terminal descent and turbulence[65,154,155]. The resulting models form the basis of dispersal predictions, but they can yield biased estimates of lateral displacement because anisotropic drag and tilt-induced reorientation are not represented explicitly.

The simplest dispersal equation arises from a ballistic argument[156], $X = HU/V_y$, where X is dispersal distance, H is the release height, U is the crosswind speed, and V_y is the still-air terminal descent velocity. The form has been widely applied to compare dispersal capacity among wind dispersed plants[71,157–160]. Assumptions include constant V_y and uniform U throughout descent. *A. ginnala* samaras disperse farther than rolling samaras in this model because of their lower descent velocity, but the formulation cannot capture behaviors such as drop-out, which we observed to occur with *A. ginnala* samaras consistently when $U/V_{tip} > 1.6$.

Several extensions of the ballistic argument incorporate aerodynamic interactions such as drag coefficients[141,148]. Using measured values of $V_{y,U}$ under crosswind, the modified relation becomes $X = HU/V_{y,U}$. Average dispersal distances dropped markedly relative to the ballistic model, reflecting the impact of crosswind-induced acceleration of descent. However, this substitution still neglects the influence of horizontal drag on the samaras and the variability of the wind profile.

A further limitation of the ballistic model is its assumption of constant wind. In reality, wind speed varies with height[161,162], and height-dependent profiles $U(z)$ have long been used to account for this[163–167]. Following this approach, we let wind speed vary with height and model the horizontal wind $U(z)$ as lognormal, with the mean set by the vertical profile and the log-space standard deviation fixed at $\sigma_{\ln} = 0.3$. The parameter $\sigma_{\ln}$ specifies the variability of wind speeds about the mean profile by treating instantaneous values of $U(z)$ as

lognormally distributed. At each height z, the mean of the distribution is given by the vertical wind profile, while $\sigma_{\ln}$ defines the spread in log-space. Larger $\sigma_{\ln}$ values produce broader fluctuations of $U(z)$ around its mean, whereas smaller $\sigma_{\ln}$ concentrate $U(z)$ more tightly about the profile. We use $\sigma_{\ln} = 0.3$, consistent with values reported in the literature[65,155] for canopy-layer winds and representing roughly a 30% coefficient of variation for U. Given species-specific settling speeds $V_{y,U}$, the ballistic distance is

$$X = \frac{H\,U(z)}{V_{y,U}}. \tag{5.25}$$

Using the measured $V_{y,U}$ for each species, radial plots of dimensionless dispersal distance X/H are shown in **Fig.5.13**a.

Direct treatment of samara aerodynamics is possible using the present dataset. Expressing dispersal distance in terms of the measured velocity ratio yields

$$X = \frac{V_{x,U}}{V_{y,U}}\,H, \tag{5.26}$$

which emphasizes the role of tilt-induced lateral velocity. Rolling samaras achieve higher $V_{x,U}/V_{y,U}$ and therefore greater dispersal than *Acer* samaras as shown in **Fig.5.13**b. Average lateral-to-vertical ratios increased, showing how crosswind responsiveness rather than low descent velocity governs dispersal potential.

The three tiers of models highlight a progression. The constant wind ballistic form offers a transparent benchmark but tends to overestimate distances when real aerodynamics are ignored. Incorporating $V_{y,U}$ reduces means and narrows spread, capturing the descent speed acceleration induced by crosswind. Allowing $U(z)$ to fluctuate broadens X/H around the mean profile and shifts mass toward larger radii, yet very long tails only arise when vertical velocity fluctuations are explicitly modeled. Consequently, average displacement ratios decrease systematically from ballistic to drag-modified to height-varying wind cases. The overall progression aligns with mechanistic accounts that identify vertical turbulence as the key process for true long distance dispersal[155,168]. Although the rolling samaras descend faster than their *Acer* counterparts, their greater cross-wind responsiveness provides a graphical and mechanistic confirmation that rolling enhances dispersal potential. Despite their higher settling velocity, the roll mechanism ultimately promotes more effective lateral transport.

5.3 Synthesis and Implications

Our study highlights the remarkable resilience of samaras to environmental perturbations, particularly their ability to recover swiftly from raindrop collisions. The impact location plays a crucial role in determining the dynamic response of the samara to the impact force. Collisions near the nutlet—close to the samara center of mass—cause minimal disruption, whereas wingtip impacts significantly alter coning angles and post-impact descent velocities, leading to longer recovery trajectories. Samaras utilize a range of water-shedding strategies to remove raindrops in less than 50 ms and return to autorotation. The "choice" of shedding mode is innately connected to impact location and dynamics and is the most critical factor governing recovery distance. Their robustness to both static[11] and dynamic perturbations underscores their evolutionary optimization for dispersal. Despite the transient disruptions caused by raindrops, the reduction in flight time is less than 10%, resulting in a minor reduction in dispersal distance. These findings emphasize the robustness of samaras in maintaining their dispersal efficiency under adverse weather conditions.

The proportion of successful recoveries to autorotation following impact within our wind tunnel, 71%, would be greater with a deeper and wider tunnel cross-section. Most non-recoverable impacts are the result of collisions with the tunnel floor, while a significantly smaller fraction of impacts result in collisions with the tunnel walls. While these wall collisions demonstrate a limitation in our 15-cm square tunnel, their relative rarity highlights the subtlety of lateral movement caused by raindrop collisions. Future experiments could consider the effects of crosswinds[14] during impacts, requiring a more elaborate experiment.

Maples are economically and commercially significant hardwoods, prized for their syrup, flooring timber, and their role as cornerstone species in the Eastern United States[169]. The proliferation of maple species in rapidly changing climates is their ability to disperse their seeds beyond the canopy of their parent tree[8]. Maples are not alone in employing autorotation to disperse seeds. Our recovery results are immediately applicable to *Pinus spp.* samaras, another genus of large economic importance[170]. The rolling samaras of the tulip poplar (*Liriodendron tulipifera*) and ash (*Fraxinus spp.*) trees will likely exhibit similar shedding modes to the ones we describe. Our results provide context to studies focused on wind transport of non-rotating seeds, including those that travel hundreds of miles[171–173]. Beyond seeds, other biological gliders including gliding ants (*Cephalotes atratus*)[174], juvenile draco lizards (*Draco spp.*)[175], and nymphal stick insects (*Extatosoma tiaratum*)[176], may also encounter raindrops during descent. Our results and methods may inform future flight perturbation studies considering a vast array of autorotators and gliders. In this study, we subject three species of rolling samaras and one species of *Acer* samaras to a concen-

trated crosswind during their otherwise passive descent. When compared to *Acer* samaras, rolling samaras achieve greater lateral displacement, longer arcing trajectories, and higher tilt-induced drift angles while maintaining coherent autorotation under strong crossflows. The ratio U/v_{tip} distinguishes inertia-dominated motion, where rotation controls the trajectory, from crosswind-dominated motion, where ambient flow governs the response. *Acer* samaras approach a transitional–unstable range near $U/v_{\text{tip}} \approx 1.6$, whereas rollers remain inertia-dominated with $U/v_{\text{edge}} < 1$ across all tested winds.

The descent path of samaras in quiescent air is well-described by a simple helix. Crosswind tilts and stretches the samara helical path, increasing the coning angle, slowing precession, and accelerating vertical descent. Greater tilt angles away from the vertical increase lateral drift but shorten flight time, which suggests a maximum dispersal range at intermediate wind strengths. Definition of a tilted, stretched helix permits the determination of kinetic energy. Kinetic energy per unit mass decreases as the strength of the crosswind grows. Vertical and lateral drag coefficients decline with crossing strength as the area of the wing facing the flow becomes smaller, reducing the ability of the wind to push the samara laterally as crosswind speed increases.

The Strouhal number, a common dimensionless group used to describe unsteady flows, incorporates samara kinematics and windage into a single measure of transport. Across species, $\Delta x/\Delta y$ decreases with increasing crosswind Strouhal number, following an approximate inverse relation $\Delta x/\Delta y \sim \text{St}_U^{-1}$. Lateral transport depends primarily on how effectively the wing edge samples the ambient flow relative to the imposed crosswind.

While scaling laws highlight broad patterns of crosswind transport, predictive dispersal models require direct incorporation of measured kinematic responses. Incorporating crosswind-responsive kinematics into dispersal models, through measured $V_{y,U}$ and the velocity ratio $V_{x,U}/V_{y,U}$, reduces bias relative to ballistic estimates and captures the broader spread produced under realistic windage. Rolling samaras achieve greater lateral transport despite higher settling speeds because crosswind responsiveness increases $V_{x,U}/V_{y,U}$ relative to still-air ballistic expectations.

Chapter 6
Conclusion

Job 12: 7-10 – *But ask the animals, and they will teach you, or the birds in the sky, and they will tell you; or speak to the earth, and it will teach you, or let the fish in the sea inform you. Which of all these does not know that the hand of the Lord has done this? In his hand is the life of every creature and the breath of all mankind.*

6.1 Samaras are robust to perturbations

Across the course of this dissertation, samaras—both rolling and autorotating—emerge as remarkably robust and resilient. Aerodynamic strategies endure despite substantial morphological perturbations. Seeds can withstand more than double their own weight, continue to autorotate even with broken or damaged wings, and maintain stable descent in the face of irregularities that would destabilize many engineered flyers.

Resilience extends beyond morphology to dynamic perturbations. Seeds recover within milliseconds after raindrop impacts, regaining autorotation and continuing descent as if uninterrupted. In crosswinds, they do more than simply endure; they harness the ambient flow to travel farther outward, tilting and drifting in ways that increase dispersal potential. Such responses are achieved without any active control systems, relying solely on the elegant interplay of form, mass distribution, and aerodynamic forces.

The strength of samaras lies in simplicity. By relying on intrinsic stability and passive aerodynamic mechanisms, seeds achieve a robustness that allows them to fulfill their purpose—carrying life beyond the parent tree—despite the uncertainties of their environment.

Taken together, the study of samaras reveals not only the physics of flight but also the elegance of natural design. Rolling and non-rolling samaras alike demonstrate that robustness and adaptability are central to survival and dispersal. Resilience in the face of perturbation demonstrates the enduring principle that form and function, when unified by purpose, can thrive in even the most challenging conditions.

6.2 Significance Statement

The study of samaras, the winged seeds of certain trees, provides a unique opportunity to examine the intersection of biology, ecology, and fluid dynamics. Evolved adaptations enable

these natural passive flyers to disperse effectively under various environmental conditions, including rain and turbulent winds. Aerodynamic resilience is explored by comparing the differences between maple and rolling samaras, building on natural dispersal mechanisms. Maple samaras exhibit a well-studied autorotative descent, whereas rolling samaras introduce additional complexity through coupled rolling and autorotative motion. Investigating these distinct seed types reveals the advantages and trade-offs inherent in their morphology and kinematics.

The ecological significance of this work lies in its contribution to understanding seed dispersal mechanisms, which are vital for the survival and proliferation of tree species that provide essential ecological services. Trees such as maples and ash play foundational roles in ecosystems, offering habitat, food, and other resources for a wide range of organisms. Furthermore, their economic importance extends to timber production, maple syrup harvesting, and contributions to global carbon sequestration efforts.

From an engineering perspective, samaras serve as a model for designing robust micro-airborne vehicles (MAVs) and bio-inspired aerial systems. By exploring how samaras respond to morphological perturbations, such as changes in mass or wing structure, and environmental challenges, such as raindrop impacts and turbulent gusts, this study provides key insights for developing technologies capable of stable flight in adverse conditions. Understanding these interactions also offers potential applications in conservation, where insights into dispersal strategies can inform reforestation and ecosystem restoration efforts, particularly under changing climatic conditions.

Expanding the understanding of evolutionary strategies that enable samaras to adapt and thrive in complex environments provides valuable insights into both ecological and engineering applications. Investigating how morphological characteristics and environmental interactions shape flight dynamics emphasizes the interconnectedness of natural and technological systems. Nature-inspired advancements informed by these findings have the potential to drive innovation in both scientific research and practical applications.

6.3 Broader Impacts

A mechanics-first framework for passive aerial locomotion emerges by uniting maple samara descent with a classic drag balance and revealing a simple thickness law that governs rolling-samara kinematics (e.g., $V_d \sim 1/b$). Resulting design rules translate directly to low-power, fault-tolerant flyers—micro air vehicles, passive sensor packages, and seed-inspired deployables—that rely on geometry rather than active control to remain stable in gusts, crosswinds, and even raindrop impacts. Projected area and coning angle collapse performance across

maple species, while thickness sets rolling and precessional rates; together these scalings let engineers size wings, target descent rates, and tune robustness without added mass or complexity. Such principles can lower energy budgets for environmental monitoring, precision agriculture, or post-disaster communications where passive recovery from perturbations is valuable. The work also supports accessible education at the biology–aerodynamics–robotics interface: open measurements and simple analogue models (e.g., falling plates) are well suited for classroom laboratories, outreach demonstrations, and interdisciplinary capstones that link ecological function to engineered form. In sum, the synthesis strengthens feedback between basic ecology and bio-inspired design, enabling systems that are efficient, resilient, and environmentally aligned.

6.4 Ecological Impacts

Wind-dispersed seeds underpin forest regeneration, biodiversity, carbon storage, hydrologic regulation, and regional economies tied to maple, poplar, and ash. By identifying when descent is set primarily by projected area and coning (autorotators) versus when it is thickness-controlled (rollers), this work improves parameterization of seed-dispersal models that forecast spread, recruitment, and gene flow under variable weather. Explicit tests of perturbations—crosswind exposure and raindrop impacts—clarify why many diaspores remain stable and recover quickly in realistic canopy conditions, supporting more reliable predictions of dispersal kernels during storms or wet periods. Such predictions matter for restoration planning (e.g., choosing seed sources and stand structures that maximize natural regeneration), for managing fragmented habitats (maintaining connectivity via dispersal distance), and for anticipating climate-driven range shifts where mechanistic kernels replace ad-hoc assumptions. By linking measurable traits (area, coning angle, thickness) to dispersal performance across species and conditions, the dissertation provides a tractable bridge from seed form to population and landscape processes that conservation practitioners and foresters can apply in practice.

6.5 Wonder in Creation and Creator

Studying the flight of maple seeds has taught me much more than physics and aerodynamics. The small, unassuming samaras embody both purpose and resilience. No matter their imperfections or perturbations, they are designed to journey outward, carrying life to new places. In many ways, their persistence in flight has mirrored my own pursuit of knowledge during these years—reminding me that endurance, adaptability, and trust in purpose are

essential for growth.

My doctoral journey has also unfolded alongside profound personal change. I have moved homes, found new communities, and entered into marriage—each transition shaping me just as deeply as the challenges of research. Growth often comes through disruption, and beauty can emerge in unexpected ways.

Most of all, the process of inquiry has deepened my awe for God and His creation. Every seed in flight is a testimony to His wisdom, creativity, and provision. Science has not separated me from faith but has instead invited me into greater wonder at the One who made all things. In the pursuit of knowledge, I have been reminded that "the fear of the Lord is the beginning of wisdom" (Proverbs 9:10), and that true understanding ultimately points back to Him.

In closing, I pray that this work, like the samaras I have studied, may serve a purpose beyond itself—carrying forward seeds of curiosity, inspiration, and truth. As Isaiah writes: "As the rain and the snow come down from heaven, and do not return to it without watering the earth and making it bud and flourish, so that it yields seed for the sower and bread for the eater, so is my word that goes out from my mouth: It will not return to me empty, but will accomplish what I desire and achieve the purpose for which I sent it" (Isaiah 55:10–11).

Bibliography

[1] Jack Hollingum. Military look to flying insect robots. *Industrial Robot: An International Journal*, 25(2):124–128, 1998.

[2] David Lentink. Flying like a fly. *Nature*, 498(7454):306–307, 2013.

[3] Kevin Y Ma, Pakpong Chirarattananon, Sawyer B Fuller, and Robert J Wood. Controlled flight of a biologically inspired, insect-scale robot. *Science*, 340(6132):603–607, 2013.

[4] Andrew Nahum. The imitation of nature? flapping flight and animal forms as models for human flight. *History and Technology, an International Journal*, 12(3):225–260, 1995.

[5] Huichao Deng, Shengjie Xiao, Binxiao Huang, Lili Yang, Xinyi Xiang, and Xilun Ding. Design optimization and experimental study of a novel mechanism for a hover-able bionic flapping-wing micro air vehicle. *Bioinspiration & Biomimetics*, 16(2):026005, 2020.

[6] Aditya A Paranjape, Michael R Dorothy, Soon-Jo Chung, and Ki-D Lee. A flight mechanics-centric review of bird-scale flapping flight. *International Journal of Aeronautical and Space Sciences*, 13(3):267–281, 2012.

[7] David F Greene and Edward A Johnson. Seed mass and dispersal capacity in wind-dispersed diaspores. *Oikos*, pages 69–74, 1993.

[8] Raymond P Guries and Erik V Nordheim. Flight characteristics and dispersal potential of maple samaras. *Forest Science*, 30(2):434–440, 1984.

[9] Ran Nathan, Gabriel G. Katul, Henry S. Horn, Suvi M. Thomas, Ram Oren, Roni Avissar, Stephen W. Pacala, and Simon A. Levin. Mechanisms of long-distance dispersal of seeds by wind. *Nature*, 2002. doi: 10.1038/nature00844.

[10] Akira Azuma and Yoshinori Okuno. Flight of a samara, alsomitra macrocarpa. *Journal of Theoretical Biology*, 129(3):263–274, 1987.

[11] Breanna M Schaeffer, Spencer S Truman, Tadd T Truscott, and Andrew K Dickerson. Maple samara flight is robust to morphological perturbation and united by a classic drag model. *Communications Biology*, 7(1):248, 2024.

[12] Kunio Yasuda and Akira Azuma. The autorotation boundary in the flight of samaras. *Journal of Theoretical Biology*, 185(3):313–320, 1997. ISSN 0022-5193. doi: https://doi.org/10.1006/jtbi.1996.0299. URL `https://www.sciencedirect.com/science/article/pii/S0022519396902994`.

[13] R Åke Norberg. Autorotation, self-stability, and structure of single-winged fruits and seeds (samaras) with comparative remarks on animal flight. *Biological Reviews*, 48(4): 561–596, 1973.

[14] Pei Xing Niu, Michael D Atkins, Yan Yan Liu, Tian Jian Lu, and Tongbeum Kim. Kinematic responses of an autorotating samara to concentrated crosswind. *Physics of Fluids*, 34(11), 2022.

[15] Breanna M. Schaeffer, Tadd T. Truscott, and Andrew K. Dickerson. Maple samaras recover autorotation following raindrop collisions. *Proceedings of the National Academy of Sciences*, 122(7):e2422641122, 2025. doi: 10.1073/pnas.2422641122. URL `https://www.pnas.org/doi/abs/10.1073/pnas.2422641122`.

[16] Andrew P Smith and David Lindenmayer. Tree hollow requirements of leadbeater's possum and other possums and gliders in timber production ash forests of the victorian central highlands. *Wildlife Research*, 15(4):347–362, 1988.

[17] Kaitano Dube. A comprehensive review of climatic threats and adaptation of marine biodiversity. *Journal of Marine Science and Engineering*, 12(2):344, 2024.

[18] Aaron M Ellison, Michael S Bank, Barton D Clinton, Elizabeth A Colburn, Katherine Elliott, Chelcy R Ford, David R Foster, Brian D Kloeppel, Jennifer D Knoepp, Gary M Lovett, et al. Loss of foundation species: consequences for the structure and dynamics of forested ecosystems. *Frontiers in Ecology and the Environment*, 3(9):479–486, 2005.

[19] Robert W Malmsheimer, Patrick Heffernan, Steve Brink, Douglas Crandall, Fred Deneke, Christopher Galik, Edmund Gee, John A Helms, Nathan McClure, Michael Mortimer, et al. Forest management solutions for mitigating climate change in the united states. *Journal of Forestry*, 106(3):115–173, 2008.

[20] Richard Shine, Gregory P Brown, and Benjamin L Phillips. An evolutionary process that assembles phenotypes through space rather than through time. *Proceedings of the National Academy of Sciences*, 108(14):5708–5711, 2011.

[21] Hanne De Kort, Jérôme G Prunier, Simon Ducatez, Olivier Honnay, Michel Baguette,

Virginie Marie Stevens, and Simon Blanchet. Life history, climate and biogeography interactively affect worldwide genetic diversity of plant and animal populations. *Nature communications*, 12(1):516, 2021.

[22] Tomás A Carlo, Daniel García, Daniel Martínez, Jason M Gleditsch, and Juan M Morales. Where do seeds go when they go far? distance and directionality of avian seed dispersal in heterogeneous landscapes. *Ecology*, 94(2):301–307, 2013.

[23] Ran Nathan, Gabriel G Katul, Gil Bohrer, Anna Kuparinen, Merel B Soons, Sally E Thompson, Ana Trakhtenbrot, and Henry S Horn. Mechanistic models of seed dispersal by wind. *Theoretical Ecology*, 4:113–132, 2011.

[24] Kapil Varshney, Song Chang, and Z. Wang. The kinematics of falling maple seeds and the initial transition to a helical motion. *Nonlinearity*, 25:C1, 12 2011. doi: 10.1088/0951-7715/25/1/C1.

[25] Victor Manuel Ortega-Jimenez, Antonio Martín-Alcántara, Ramon Fernandez-Feria, and Robert Dudley. On the autorotation of animal wings. *Journal of The Royal Society Interface*, 14(126):20160870, 2017.

[26] Michael H Dickinson, Fritz-Olaf Lehmann, and Sanjay P Sane. Wing rotation and the aerodynamic basis of insect flight. *Science*, 284(5422):1954–1960, 1999.

[27] Douglas S Green. The terminal velocity and dispersal of spinning samaras. *American Journal of Botany*, 67(8):1218–1224, 1980.

[28] Fiona J Thomson, Angela T Moles, Tony D Auld, and Richard T Kingsford. Seed dispersal distance is more strongly correlated with plant height than with seed mass. *Journal of ecology*, 99(6):1299–1307, 2011.

[29] Timothy W Sipe and Amy R Linnerooth. Intraspecific variation in samara morphology and flight behavior in acer saccharinum (aceraceae). *American Journal of Botany*, 82 (11):1412–1419, 1995.

[30] Sarah V Wyse and Philip E Hulme. Limited evidence for a consistent seed mass-dispersal trade-off in wind-dispersed pines. *Journal of Ecology*, 109(1):284–293, 2021.

[31] Akira Azuma and Kunio Yasuda. Flight performance of rotary seeds. *Journal of Theoretical Biology*, 138(1):23–53, 1989. ISSN 0022-5193. doi: https://doi.org/10.1016/S0022-5193(89)80176-6.

[32] Henry S Horn, RAN Nathan, and Sarah R Kaplan. Long-distance dispersal of tree seeds by wind. *Ecological research*, 16:877–885, 2001.

[33] CW McCutchen. The spinning rotation of ash and tulip tree samaras. *Science*, 197 (4304):691–692, 1977.

[34] Douglas S Green. The terminal velocity and dispersal of spinning samaras. *American Journal of Botany*, 67(8):1218–1224, 1980.

[35] Andrew Belmonte, Hagai Eisenberg, and Elisha Moses. From flutter to tumble: inertial drag and froude similarity in falling paper. *Physical Review Letters*, 81(2):345, 1998.

[36] WB Wang, RF Hu, SJ Xu, and ZN Wu. Influence of aspect ratio on tumbling plates. *Journal of fluid mechanics*, 733:650–679, 2013.

[37] Kapil Varshney, Song Chang, and Z Jane Wang. Unsteady aerodynamic forces and torques on falling parallelograms in coupled tumbling-helical motions. *Physical Review E—Statistical, Nonlinear, and Soft Matter Physics*, 87(5):053021, 2013.

[38] Anders Andersen, Umberto Pesavento, and Z Jane Wang. Unsteady aerodynamics of fluttering and tumbling plates. *Journal of Fluid Mechanics*, 541:65–90, 2005.

[39] David Lentink and Michael H Dickinson. Rotating wings: stability and design optimization. *Journal of Experimental Biology*, 212(14):2143–2150, 2009.

[40] Eui-Jae Lee and Sang-Joon Lee. Autorotation characteristics of maple seeds with different initial attitudes. *Journal of Mechanical Science and Technology*, 30:1475–1483, 2016. doi: 10.1007/s12206-016-0129-2.

[41] Rui Fang, Yanlai Zhang, and Yanpeng Liu. Aerodynamics and flight dynamics of free-falling ash seeds. *World Journal of Engineering and Technology*, 5(4):105–116, 2017.

[42] Charles P. Ellington. The aerodynamics of insect flight ii. morphological parameters. *Philosophical Transactions of the Royal Society of London. Series B: Biological Sciences*, 305(1122):17–40, 1996.

[43] Henry F Howe and Judith Smallwood. Ecology of seed dispersal. *Annual review of ecology and systematics*, 13:201–228, 1982.

[44] S Joseph Wright, Ana Trakhtenbrot, Gil Bohrer, Matteo Detto, Gabriel G Katul, Nir Horvitz, Helene C Muller-Landau, Frank A Jones, and Ran Nathan. Understanding

strategies for seed dispersal by wind under contrasting atmospheric conditions. *Proceedings of the National Academy of Sciences*, 105(49):19084–19089, 2008.

[45] Henry S. Horn, Ran Nathan, and Sarah Kaplan. Long-distance dispersal of tree seeds by wind. *Ecological Research*, 2001. doi: 10.1046/j.1440-1703.2001.00456.x.

[46] K. D. Maurer, G. Bohrer, D. Medvigy, and S. J. Wright. The timing of abscission affects dispersal distance in a wind-dispersed tropical tree. *Functional Ecology*, 27: 208–218, 2012. doi: 10.1111/1365-2435.12028.

[47] D. F. Greene and E. A. Johnson. Seed mass and dispersal capacity in wind-dispersed diaspores. *Oikos*, 67(1):69–74, 1993. ISSN 00301299, 16000706. URL `http://www.jstor.org/stable/3545096`.

[48] Craig W Benkman. Wind dispersal capacity of pine seeds and the evolution of different seed dispersal modes in pines. *Oikos*, pages 221–224, 1995.

[49] Merel B Soons, Gerrit W Heil, Ran Nathan, and Gabriel G Katul. Determinants of long-distance seed dispersal by wind in grasslands. *Ecology*, 85(11):3056–3068, 2004.

[50] G. Bohrer, G. G. Katul, R. Nathan, R. L. Walko, and R. Avissar. Effects of canopy heterogeneity, seed abscission and inertia on wind-driven dispersal kernels of tree seeds. *Journal of Ecology*, 96:569–580, 2008. doi: 10.1111/j.1365-2745.2008.01368.x.

[51] T. Wan and S.W. Wu. Aerodynamic analysis under influence of heavy rain. *Journal of Aeronautics, Astronautics, and Aviation*, pages 173–180, 2004.

[52] Jr. Hastings, E. C. and G. S. Manuel. Scale-model tests of airfoils in simulated heavy rain. *Journal of Aircraft*, 22(6):536–540, 1985. doi: 10.2514/3.45161.

[53] C.C. Voigt, K. Schneeberger, S.L. Voigt-Heucke, and D. Lewanzik. Rain increases the energy cost of bat flight. *Biology letters*, 7(5):793–795, 2011.

[54] Andrew K. Dickerson, Peter G. Shankles, Nihar M. Madhavan, and David L. Hu. Mosquitoes survive raindrop collisions by virtue of their low mass. *Proceedings of the National Academy of Sciences*, 109(25):9822–9827, 2012.

[55] Andrew K Dickerson, Peter G Shankles, and David L Hu. Raindrops push and splash flying insects. *Physics of Fluids*, 26(2):027104, 2014.

[56] T. Engels, D. Kolomenskiy, K. Schneider, F. Lehmann, and J. Sesterhenn. Bumble-

bee flight in heavy turbulence. *Physical Review Letters*, 116, 2016. doi: 10.1103/physrevlett.116.028103.

[57] Ali Tokay, Walter A. Petersen, Patrick Gatlin, and Matthew Wingo. Comparison of raindrop size distribution measurements by collocated disdrometers. *Journal of Atmospheric and Oceanic Technology*, 30(8):1672–1690, 2013. doi: 10.1175/JTECH-D-12-00163.1.

[58] Torkel Weis-Fogh. Quick estimates of flight fitness in hovering animals, including novel mechanisms for lift production. *Journal of experimental Biology*, 59(1):169–230, 1973.

[59] Y. Bhosale, E. Esmaili, K. Bhar, and S. Jung. Bending, twisting and flapping leaf upon raindrop impact. *Bioinspiration & Biomimetics*, 15:036007, 2020. doi: 10.1088/1748-3190/ab68a8.

[60] Zixuan Wu, Saikat Basu, Seungho Kim, Mark Sorrells, Francisco J Beron-Vera, and Sunghwan Jung. Coherent spore dispersion via drop-leaf interaction. *Science advances*, 10(5):eadj8092, 2024.

[61] Guillermo J Amador, Yasukuni Yamada, Matthew McCurley, and David L Hu. Splash-cup plants accelerate raindrops to disperse seeds. *Journal of The Royal Society Interface*, 10(79), 2013.

[62] D. A. Watson, M. R. Thornton, H. A. Khan, R. C. Diamco, D. Yilmaz-Aydin, and A. K. Dickerson. Water striders are impervious to raindrop collision forces and submerged by collapsing craters. *Proceedings of the National Academy of Sciences*, 121, 2024. doi: 10.1073/pnas.2315667121.

[63] Shizuka Minami and Akira Azuma. Various flying modes of wind-dispersal seeds. *Journal of Theoretical Biology*, 225(1):1–14, 2003. doi: 10.1016/S0022-5193(03)00216-9.

[64] F. M. Burrows. Wind-borne seed and fruit movement. *New Phytologist*, 75(2):405–418, 1975.

[65] D. F. Greene and E. A. Johnson. A model of wind dispersal of winged or plumed seeds. *Ecology*, 70(2):339–347, 1989.

[66] Henry S. Horn, Ran Nathan, and Sarah R. Kaplan. Long-distance dispersal of tree seeds by wind. *Ecological Research*, 16(5):877–885, 2001.

[67] Akira Azuma and Kunio Yasuda. Flight performance of rotary seeds. *Journal of Theoretical Biology*, 138(1):23–53, 1989. doi: 10.1016/S0022-5193(89)80176-6.

[68] David F. Greene and Edward A. Johnson. A model of wind dispersal of winged or plumed seeds. *Ecology*, 70(2):339–347, 1989. doi: 10.2307/1937538.

[69] Breanna M Schaeffer and Andrew K Dickerson. Precession dynamics and morphology of rolling samaras. *Royal Society*, 2(2):163–166, 2025. doi: 10.1098/rsbl.2005.0427.

[70] Anders Andersen, Umberto Pesavento, and Z Jane Wang. Unsteady aerodynamics of fluttering and tumbling plates. *Journal of Fluid Mechanics*, 541:65–90, 2005. doi: 10.1017/S002211200500594X.

[71] Carol K. Augspurger. Morphology and dispersal potential of wind-dispersed diaspores of neotropical trees. *American Journal of Botany*, 73(3):353–363, 1986. doi: 10.2307/2444294.

[72] David F. Greene and Mark A. Johnson. The dispersal of seeds by wind. *Ecology*, 76 (5):1529–1536, 1995. doi: 10.2307/1938148.

[73] David Lentink and Michael H. Dickinson. Rotational accelerations stabilize leading edge vortices on revolving fly wings. *Journal of Experimental Biology*, 212(16):2705–2719, 2009. doi: 10.1242/jeb.022269. URL `https://doi.org/10.1242/jeb.022269`.

[74] Akira Azuma and Kazuo Yasuda. Various flying modes of wind-dispersal seeds. *Journal of Theoretical Biology*, 138(1):23–53, 1989. doi: 10.1016/S0022-5193(89)80110-2.

[75] W. Willmarth, W. E. Hawk, N. and L. Harvey, R.˙Steady and unsteady motions and wakes of freely falling disks. *Physics of Fluids*, 7:197–208, 1964.

[76] B. Field, Stuart M. Klaus, G. Moore, M. and Franco Nori. Chaotic dynamics of falling disks. *Nature*, 388(6639):252–254, 1997. doi: 10.1038/40817.

[77] A. Andersen, U. Pesavento, and J. Wang, Z.˙Analysis of transitions between fluttering, tumbling and steady descent of falling cards. *Journal of Fluid Mechanics*, 541:91–104, 2005. doi: 10.1017/S002211200500594X.

[78] Yifan Li and Z. Jane Wang. Shape optimization and center-of-mass control of tumbling wings. *Physical Review Fluids*, 7(5):054702, 2022. doi: 10.1103/PhysRevFluids.7.054702.

[79] Ravi Datt Mehta and Peter Bradshaw. Design rules for small low speed wind tunnels. *The Aeronautical Journal*, 83(827):443–453, 1979.

[80] Tyson L Hedrick. Software techniques for two-and three-dimensional kinematic measurements of biological and biomimetic systems. *Bioinspiration & biomimetics*, 3(3): 034001, 2008.

[81] David Lentink, William B Dickson, Johan L Van Leeuwen, and Michael H Dickinson. Leading-edge vortices elevate lift of autorotating plant seeds. *Science*, 324(5933):1438–1440, 2009.

[82] Gonzalo Arranz, Manuel Moriche, Markus Uhlmann, Oscar Flores, and Manuel García-Villalba. Kinematics and dynamics of the auto-rotation of a model winged seed. *Bioinspiration & biomimetics*, 13(3):036011, 2018.

[83] FE Fish. Wing design and scaling of flying fish with regard to flight performance. *Journal of Zoology*, 221(3):391–403, 1990.

[84] Hao Li, Shijun Guo, YL Zhang, C Zhou, and JH Wu. Unsteady aerodynamic and optimal kinematic analysis of a micro flapping wing rotor. *Aerospace Science and Technology*, 63:167–178, 2017.

[85] Eugene W Schupp, Rafal Zwolak, Landon R Jones, Rebecca S Snell, Noelle G Beckman, Clare Aslan, Brittany R Cavazos, Edu Effiom, Evan C Fricke, Flavia Montaño-Centellas, et al. Intrinsic and extrinsic drivers of intraspecific variation in seed dispersal are diverse and pervasive. *AoB Plants*, 11(6):plz067, 2019.

[86] Bin JW Chen, Xinyu Wang, Yuting Dong, Heinjo J During, Xia Xu, and Niels PR Anten. Maternal environmental light conditions affect the morphological allometry and dispersal potential of acer palmatum samaras. *Forests*, 12(10):1313, 2021.

[87] Stacey L Halpern. Sources and consequences of seed size variation in lupinus perennis (fabaceae): adaptive and non-adaptive hypotheses. *American Journal of Botany*, 92 (2):205–213, 2005.

[88] Lorena Gómez-Aparicio, Jose M. Gómez, and Regino Zamora. Spatiotemporal patterns of seed dispersal in a wind-dispersed mediterranean tree (acer opalus subsp. granatense): implications for regeneration. *Ecography*, 30(1):13–22, 2007.

[89] Lin Jiang, Ying Hong Pheh, Shane Kyi Hla Win, Yuyong Tang, Yongliang Yang, and

Shaohui Foong. Mass distribution affects the circle or hypotrochoid trajectory of the maple seed. *Physics of Fluids*, 37(4), 2025.

[90] Sanghun Kwon and Min H. Sohn. Experimental study into the effects of pitch and coning angles on the flight performance of autorotating samaras. *Royal Society Open Science*, 10(6):240758, 2023. doi: 10.1098/rsos.240758. URL https://royalsocietypublishing.org/doi/10.1098/rsos.240758.

[91] Sang Joon Lee, Eui Jae Lee, and Myong Hwan Sohn. Mechanism of autorotation flight of maple samaras (acer palmatum). *Experiments in fluids*, 55:1–9, 2014.

[92] T. Maxworthy. Experiments on the weis-fogh mechanism of lift generation by insects in hovering flight. part 1. dynamics of the 'fling'. *Journal of Fluid Mechanics*, 93 (1):47–63, 1979. doi: 10.1017/S0022112079001774. URL https://doi.org/10.1017/S0022112079001774.

[93] R. Dudley and C. P. Ellington. Mechanics of forward flight in bumblebees: I. kinematics and morphology. *Journal of Experimental Biology*, 148(1):19–52, 01 1990. ISSN 0022-0949. doi: 10.1242/jeb.148.1.19. URL https://doi.org/10.1242/jeb.148.1.19.

[94] J. M. Wakeling and C. P. Ellington. Dragonfly flight : Ii. velocities, accelerations and kinematics of flapping flight. *Journal of Experimental Biology*, 200(3):557–582, 02 1997. ISSN 0022-0949. doi: 10.1242/jeb.200.3.557. URL https://doi.org/10.1242/jeb.200.3.557.

[95] Jana Goyens, Sam Van Wassenbergh, Joris Dirckx, and Peter Aerts. Cost of flight and the evolution of stag beetle weaponry. *Journal of the Royal Society Interface*, 12 (20150222), 2015. doi: 10.1098/rsif.2015.0222. URL http://dx.doi.org/10.1098/rsif.2015.0222.

[96] C. P. Ellington. The novel aerodynamics of insect flight: Applications to micro-air vehicles. *The Journal of Experimental Biology*, 202(23):3439–3448, 1999. doi: 10.1242/jeb.202.23.3439. URL https://doi.org/10.1242/jeb.202.23.3439.

[97] Richard J. Bomphrey, Toshiyuki Nakata, Nathan Phillips, and Simon M. Walker. Smart wing rotation and trailing-edge vortices enable high frequency mosquito flight. *Nature*, 544(7648):92–95, 2017. doi: 10.1038/nature21727. URL http://dx.doi.org/10.1038/nature21727.

[98] F. T. Bonner and T. E. Russell. Liriodendron tulipifera l. In *Silvics of North America: Volume 2. Hardwoods*. USDA Forest Service, 1974.

[99] William M. Elliott et al. Riparian and valley-margin hardwood species of pre-colonial piedmont forests: A preliminary study of subfossil leaves from white clay creek, southeastern pennsylvania, usa. *Palaeontologia Electronica*, 19(2), 2016. doi: 10.26879/589.

[100] Ivana Karapandža, Ivana Bjedov, and Saša Orlović. Morphometric variability of narrow-leaved ash samaras at the test-tree level. *Archives of Biological Sciences*, 75 (1):101–110, 2023. doi: 10.2298/ABS220826002K.

[101] Karl J Niklas. Plant allometry: the scaling of form and process. *University of Chicago Press*, 1994.

[102] R. Å. Norberg. Autorotation, self-stability and structure of single-winged fruits and seeds (samaras) with comparative remarks on animal flight. *Biological Reviews*, 48(4): 561–596, 1973.

[103] Hadrien Canet, Pietro Bortolotti, and Carlo L. Bottasso. On the scaling of wind turbine rotors. *Wind Energy Science*, 6:601–626, 2021. doi: 10.5194/wes-6-601-2021.

[104] I.-C. Ardelean, D. Usov, A. Filippone, B. Parslew, and P. Hollingsworth. Unmanned wingless rotorcraft scaling, 2023. URL `https://www.researchgate.net/publication/372359200_Unmanned_Wingless_Rotorcraft_Scaling`. Accessed via ResearchGate.

[105] Ralph D. Lorenz. Flight power scaling of airplanes, airships, and helicopters: Application to planetary exploration, 2001. URL `https://www.researchgate.net/publication/242600268_Flight_Power_Scaling_of_Airplanes_Airships_and_Helicopters_Application_to_Planetary_Exploration`. Accessed via ResearchGate.

[106] David Lentink and Michael H Dickinson. Scaling laws for inertial and aerodynamic force production in flapping flight. *Journal of Experimental Biology*, 212(16):2691–2704, 2009.

[107] Ulla M. Norberg. *Vertebrate Flight: Mechanics, Physiology, Morphology, Ecology and Evolution*. Springer-Verlag, 1994.

[108] J. T. Cantrell, B. W. LaCroix, and P. Ifju. Passive roll compensation on micro air

vehicles with perimeter reinforced membrane wings. *International Journal of Micro Air Vehicles*, 5:163–177, 2013. doi: 10.1260/1756-8293.5.3.163.

[109] D. Eijkelhof, G. Buendía, and R. Schmehl. Low- and high-fidelity aerodynamic simulations of box wing kites for airborne wind energy applications. *Energies*, 16:3008, 2023. doi: 10.3390/en16073008.

[110] L. Liu, H. Li, A. Hai-song, and T. Xiao. Numerical investigation of flexible flapping wings using computational fluid dynamics/computational structural dynamics method. *Proceedings of the Institution of Mechanical Engineers, Part G: Journal of Aerospace Engineering*, 232:85–95, 2016. doi: 10.1177/0954410016671343.

[111] David F. Greene and Edward A. Johnson. The aerodynamics of plumed seeds. *Ecology*, 71(6):1836–1849, 1990. doi: 10.2307/1937589.

[112] E. M. Lau, W.-X. Huang, and C.-X. Xu. Progression of heavy plates from stable falling to tumbling flight. *Journal of Fluid Mechanics*, 850:1009–1031, 2018. doi: 10.1017/jfm.2018.506.

[113] David F. Greene. *The aerodynamics and dispersal of ash, tuliptree, and maple samaras.* Ph.d. dissertation, Princeton University, 1980.

[114] Glenn R. Matlack. Diaspore size, shape, and fall behavior in wind-dispersed plant species. *American Journal of Botany*, 74(8):1150–1160, 1987. doi: 10.1002/j.1537-2197.1987.tb08705.x.

[115] Cynthia Gerlein-Safdi, Michael C Koohafkan, Michaella Chung, Fulton E Rockwell, Sally Thompson, and Kelly K Caylor. Dew deposition suppresses transpiration and carbon uptake in leaves. *Agricultural and Forest Meteorology*, 259:305–316, 2018.

[116] Andrew K Dickerson, Xing Liu, Ting Zhu, and David L Hu. Fog spontaneously folds mosquito wings. *Physics of Fluids*, 27(2):021901, 2015.

[117] Andrew K Dickerson and David L Hu. Mosquitoes actively remove drops deposited by fog and dew. *Integrative and Comparative Biology*, pages 1–6, 2014.

[118] Richard M Godman, Harry W Yawney, and Carl H Tubbs. Acer saccharum marsh. sugar maple. *Silvics of North America*, 2(654):78, 1990.

[119] B. M. Schaeffer et al. Precession dynamics and morphology of rolling samaras. *Journal*

of the Royal Society Interface, 22(217):20250391, 2025. doi: 10.1098/rsif.2025.0391. URL https://www.ncbi.nlm.nih.gov/pmc/articles/PMC12457913/.

[120] David Lentink, Floris T. Muijres, Eize J. Stamhuis, Remco De Kat, William L. Dickinson, and Johan L. van Leeuwen. How do maple seeds (samaras) generate lift? leading-edge vortices elevate lift of autorotating real maple seeds. *Science*, 324(5933):1438–1440, 2009. doi: 10.1126/science.1168431.

[121] Sang-Joon Lee, Hyeong-Bin Park, and Jin-Hyung Kim. Leading-edge vortices of autorotating plant seeds. *Experimental Fluids*, 55(10):1837, 2014. doi: 10.1007/s00348-014-1757-5.

[122] W. W. Willmarth, N. E. Hawk, and R. L. Harvey. Steady and unsteady motions and wakes of freely falling disks. *Physics of Fluids*, 7(2):197–208, 1964. doi: 10.1063/1.1711107.

[123] A. Andersen, U. Pesavento, and Z. Jane Wang. Unsteady aerodynamics of freely falling, tumbling plates. *Journal of Fluid Mechanics*, 541:65–90, 2005. doi: 10.1017/S0022112005005303.

[124] G. K. K. Lau, M. Keennon, and R. J. Wood. Flying papers and falling leaves. *Journal of Fluid Mechanics*, 855:R4, 2018. doi: 10.1017/jfm.2018.633.

[125] David F. Greene and Ernesto A. Johnson. Seed dispersal in wind: a mechanistic and quantitative review. *Oikos*, 68(2):211–225, 1993. doi: 10.2307/3545320.

[126] Ran Nathan, G. G. Katul, H. S. Horn, S. M. Thomas, R. Oren, R. Avissar, S. W. Pacala, and S. A. Levin. Mechanisms of long-distance dispersal of seeds by wind. *Nature*, 418:409–413, 2002. doi: 10.1038/nature00844.

[127] Andrew Belmonte, H. Eisenberg, and E. Moses. From flutter to tumble: inertial drag and Froude similarity in falling paper. *Physical Review Letters*, 81(2):345–348, 1998. doi: 10.1103/PhysRevLett.81.345.

[128] Z. Jane Wang. The role of drag in insect flight and seed dispersal. *Annual Review of Fluid Mechanics*, 36:155–184, 2004. doi: 10.1146/annurev.fluid.36.050802.122033.

[129] Andrew Schaeffer, Breanna; Dickerson. *under review* rolling samara response to a concentrated crosswind. *Journal of the Royal Society B*, 2025.

[130] BP LeClair, AE Hamielec, HR Pruppacher, and WD Hall. A theoretical and experi-

mental study of the internal circulation in water drops falling at terminal velocity in air. *J. atmos. Sci*, 29(2):728–740, 1972.

[131] R. Gunn and G.D. Kinzer. The terminal velocity of fall for water droplets in stagnant air. *Journal of Meteorology*, 6:243–248, 1949.

[132] Nathan B Speirs, Jesse L Belden, and Aren M Hellum. The capture of airborne particulates by rain. *Journal of Fluid Mechanics*, 958:A40, 2023.

[133] Paula García-Geijo, Enrique Jesús Sánchez Quintero, Guillaume Riboux, and José Manuel Gordillo. Spreading and splashing of drops impacting rough substrates. *Journal of Fluid Mechanics*, 917:A50, 2021. doi: 10.1017/jfm.2021.313.

[134] M. A. Quetzeri-Santiago, A. A. Castrejón-Pita, J. R. Castrejón-Pita, and K. Yokoi. The effect of surface roughness on the contact line and splashing dynamics of impacting droplets. *Scientific Reports*, 9(15030), 2019. doi: 10.1038/s41598-019-51201-4.

[135] M. A. Quetzeri-Santiago, A. A. Castrejón-Pita, J. R. Castrejón-Pita, and K. Yokoi. Role of the dynamic contact angle on droplet splashing. *Physical Review Letters*, 122: 228001, 2019. doi: 10.1103/PhysRevLett.122.228001.

[136] M. S. Sykes, H. Chang, D. Lee, X. Xu, and J. C. Bird. Droplet splashing on curved substrates. *Soft Matter*, 18:6376–6385, 2022.

[137] Christophe Josserand and Sigurdur T Thoroddsen. Drop impact on a solid surface. *Annual Review of Fluid Mechanics*, 48:365–391, 2016.

[138] Yahua Liu, Michael Andrew, Jue Li, Julia M. Yeomans, and Zuankai Wang. Symmetry-breaking in drop bouncing on curved surfaces. *Nature Communications*, 6:10034, 2015. doi: 10.1038/ncomms10034.

[139] Andrew K Dickerson, Peter G Shankles, Bruce E Berry, and David L Hu. Fog and dense gas disrupt mosquito flight due to increased aerodynamic drag on halteres. *Journal of Fluids and Structures*, 55:451–462, 2015.

[140] VN Bringi, V. Chandrasekar, J. Hubbert, E. Gorgucci, WL Randeu, and M. Schoenhuber. Raindrop size distribution in different climatic regimes from disdrometer and dual-polarized radar analysis. *Journal of the Atmospheric Sciences*, 60(2):354–365, 2003.

[141] D. F. Greene and E. A. Johnson. The aerodynamics of plumed seeds. *Functional Ecology*, 4(1):117–125, 1990.

[142] Y. Fan, H. Dong, J. Zhou, and Y. Zhao. Detached-eddy simulation of supersonic disk-gap-band parachute flows. *Aerospace Science and Technology*, 122:107377, 2022. doi: 10.1016/j.ast.2021.107377.

[143] Feng Gao, Ming Zhang, and Jie Chen. Fluid–structure interaction simulation of supersonic disk-gap-band parachute. *Advances in Space Research*, 57(3):929–939, 2016. doi: 10.1016/j.asr.2015.12.005.

[144] Carol K. Augspurger. Morphology and dispersal potential of wind-dispersed diaspores of neotropical trees. *American Journal of Botany*, 73(3):353–363, 1986. doi: 10.1002/j.1537-2197.1986.tb12048.x.

[145] Victor Manuel Ortega-Jiménez, Robert Dudley, and Z Jane Wang. On the autorotation of animal wings. *Proceedings of the Royal Society B: Biological Sciences*, 284(1868): 20162320, 2017. doi: 10.1098/rspb.2016.2320.

[146] Akira Okubo and Simon A. Levin. A theoretical framework for data analysis of wind dispersal of seeds and pollen. *Ecology*, 70(2):329–338, 1989.

[147] Craig W. Benkman. Wind dispersal capacity of pine seeds and the evolution of different seed dispersal modes in pines. *Oikos*, 73(2):221–224, 1995. doi: 10.2307/3545911.

[148] F. M. Burrows. Wind-borne seed and fruit movement. *New Phytologist*, 75(2):405–418, 1975. doi: 10.1111/j.1469-8137.1975.tb01404.x.

[149] Andy M. Reynolds, David A. Bohan, and James R. Bell. Ballooning dispersal in arthropod taxa: conditions at take-off. *Biology Letters*, 2(2):163–166, 2006. doi: 10.1098/rsbl.2005.0427.

[150] Robert Dudley. *The Biomechanics of Insect Flight: Form, Function, Evolution*. Princeton University Press, Princeton, NJ, 2000.

[151] Christophe Eloy. Optimal strouhal number for swimming animals. *Journal of Fluids and Structures*, 30:205–218, 2012. doi: 10.1016/j.jfluidstructs.2012.03.002.

[152] Robert L. Nudds, Graham K. Taylor, and Adrian L. R. Thomas. Tuning of strouhal number for high propulsive efficiency accurately predicts how wingbeat frequency and stroke amplitude relate and scale with size and flight speed in birds. *Proceedings of the*

Royal Society B: Biological Sciences, 271(1552):2071–2076, 2004. doi: 10.1098/rspb.2004.2838.

[153] Arvind Santhanakrishnan and Laura A. Miller. Vortex formation and force generation of revolving wings at low reynolds numbers. *Physics of Fluids*, 15(2):402–414, 2003. doi: 10.1063/1.1533159.

[154] Akira Okubo and Simon A. Levin. A theoretical framework for data analysis of wind dispersal of seeds and pollen. *Ecology*, 70(2):329–338, 1989.

[155] Ran Nathan, Gabriel G. Katul, Gil Bohrer, Anna Kuparinen, Merel B. Soons, Sally E. Thompson, Ana Trakhtenbrot, and Henry S. Horn. Mechanistic models of seed dispersal by wind. *Theoretical Ecology*, 4(2):113–132, 2011. doi: 10.1007/s12080-011-0115-3.

[156] Johannes Schmidt. Seed dispersal by wind. *Botanisk Tidsskrift*, 36:141–157, 1918. No DOI available.

[157] K. W. Cremer. Dispersal of seed from eucalyptus regnans. *Australian Forestry*, 35(2):119–130, 1971. doi: 10.1080/00049158.1971.10675643.

[158] K. W. Cremer. Distance of seed dispersal in eucalypts estimated from seed weights. *Australian Forest Research*, 7:225–228, 1977. doi: 10.1007/BF02459218.

[159] Glenn R. Matlack. Diaspore size, shape, and fall behavior in wind-dispersed plant species. *American Journal of Botany*, 74(8):1150–1160, 1987. doi: 10.1002/j.1537-2197.1987.tb08728.x.

[160] W. H. O. Ernst, C. M. Veenendaal, and H. Kebakile. Fruit and seed production in a savanna and a woodland site in botswana. *Vegetatio*, 103:101–111, 1992. doi: 10.1007/BF00033419.

[161] I. Hoven. A study of the atmospheric boundary layer near the ground. *Journal of Meteorology*, 14(4):361–365, 1957. No DOI available.

[162] Roland B. Stull. *An Introduction to Boundary Layer Meteorology.* Kluwer Academic Publishers, Dordrecht, 1988. ISBN 978-90-277-2769-5. doi: 10.1007/978-94-009-3027-8.

[163] M. J. Fields. Wind profiles and seed dispersal in forests. *Journal of Applied Ecology*, 17(3):865–871, 1980. No DOI available.

[164] E. A. Johnson. Seed dispersal by wind in conifer forests of alberta. *Canadian Journal of Botany*, 59(12):2384–2399, 1981. doi: 10.1139/b81-285.

[165] D. M. Sharpe and M. J. Fields. Wind dispersal of seeds in natural plant communities. *Ecology*, 63(3):685–689, 1982. No DOI available.

[166] Ran Nathan, Henry S. Horn, and Sarah M. Chazdon. Mechanisms of long-distance dispersal of seeds by wind. *Nature*, 418:409–413, 2002. doi: 10.1038/nature00844.

[167] D. F. Greene and E. A. Johnson. A model of wind dispersal of winged or plumed seeds. *Ecology*, 70(2):339–347, 1989. doi: 10.2307/1937538.

[168] G. G. Katul, A. Porporato, R. Nathan, M. Siqueira, M. B. Soons, D. Poggi, H. S. Horn, and S. A. Levin. Mechanistic analytical models for long-distance seed dispersal by wind. *American Naturalist*, 166(3):368–381, 2005. doi: 10.1086/432589.

[169] Michael L Farrell. The economics of managing maple trees for syrup or sawtimber production. *Northern Journal of Applied Forestry*, 29(4):165–172, 2012.

[170] James L. Howard and Shaobo Liang. U.s. timber production, trade, consumption, and price statistics, 1965–2017. Technical Report FPL-RP-701, U.S. Department of Agriculture, Forest Service, Forest Products Laboratory, Madison, WI, 2019.

[171] Xiaolei Qin and others. Plant canopy plays a role in promoting seed dispersal. *Ecology and Evolution*, 12(3):e8505, 2022. doi: 10.1002/ece3.8505.

[172] Quan-Lai Zhou, Bing Liu, Zhong-Jian Yang, Gui-Yun Zhang, and Qing-Lin Guan. Relationship between seed morphological traits and wind dispersal trajectory. *Functional Plant Biology*, 46(12):1092–1100, 2019. doi: 10.1071/FP19087.

[173] Oliver Tackenberg. Modeling long-distance dispersal of plant diaspores by wind. *Ecological Monographs*, 73(2):173–189, 2003. doi: 10.1890/0012-9615(2003)073[0173:MLDOPD]2.0.CO;2.

[174] Stephen P Yanoviak and R Dudley. The role of visual cues in directed aerial descent of cephalotes atratus workers (Hymenoptera: Formicidae). *Journal of Experimental Biology*, 209(9):1777–1783, 2006.

[175] Jimmy A McGuire and Robert Dudley. The biology of gliding in flying lizards (genus draco) and their fossil and extant analogs. *Integrative and Comparative Biology*, 51(6):983–990, 2011.

[176] Yu Zeng, Sofia W Chang, Janelle Y Williams, Lynn Y-Nhi Nguyen, Jia Tang, Grisanu Naing, Chandni Kazi, and Robert Dudley. Canopy parkour: movement ecology of post-hatch dispersal in a gliding nymphal stick insect, Extatosoma tiaratum. *Journal of Experimental Biology*, 223(19):jeb226266, 2020.

[177] Sang-Joon Lee, Hyeong-Bin Park, and Jin-Hyung Kim. Leading-edge vortices of autorotating plant seeds. *Experimental Fluids*, 55(10):1837, 2014. doi: 10.1007/s00348-014-1757-5.

Appendices

Appendix A
Supplementary Figures

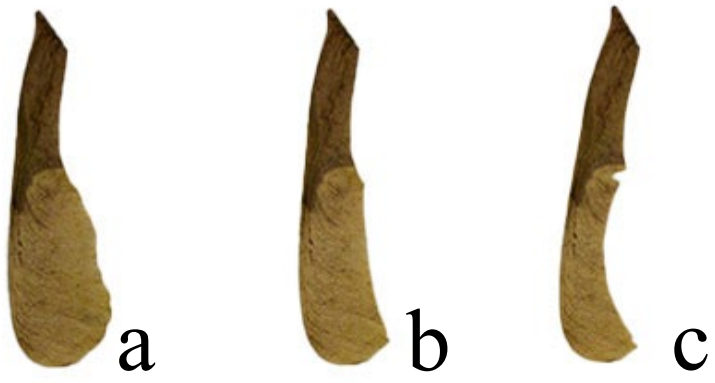

Figure A.1: A series of area reductions from an *A. Negundo* samara. (a) unaltered, (b) cut once, and (c) cut again.

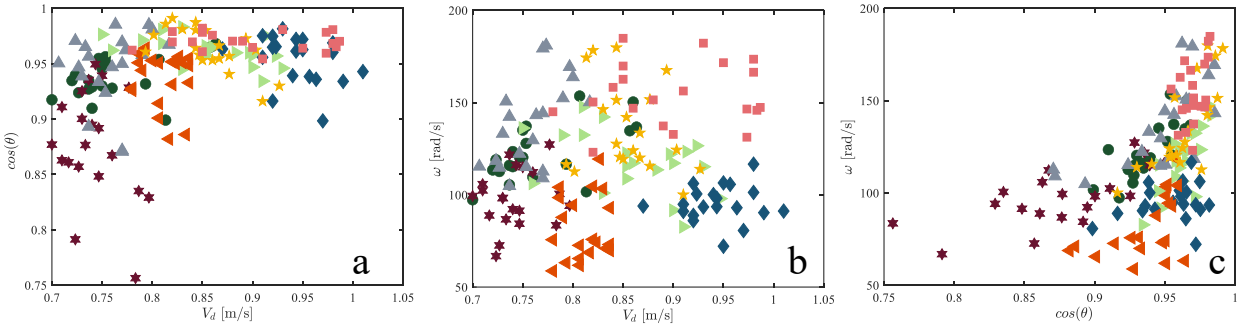

Figure A.2: Relationships between dynamic variables (a) V_d vs $cos(\theta)$, (b) V_d vs ω (c) $cos(\theta)$ vs ω

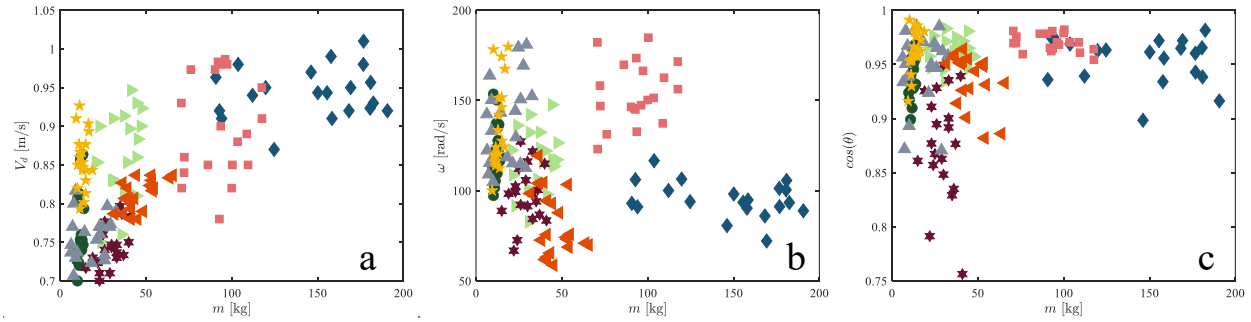

Figure A.3: Relationships between mass and dynamic variables (a) m vs V_d, (b) m vs ω (c) m vs $cos(\theta)$

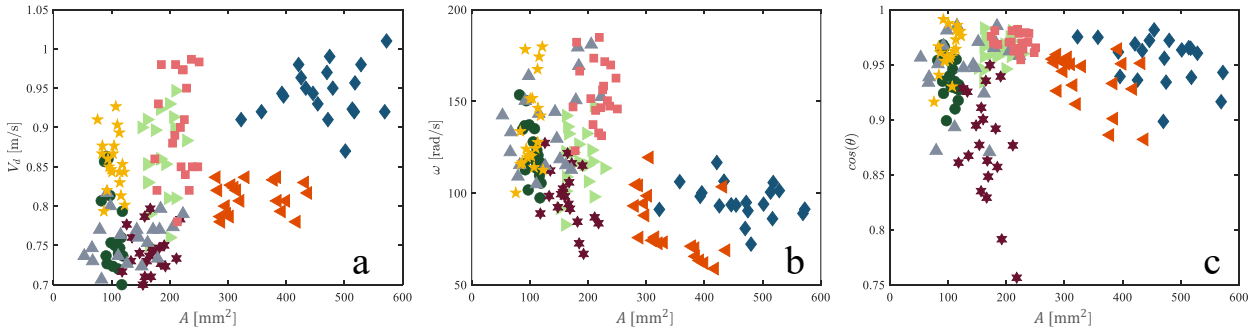

Figure A.4: Relationships between area and dynamic variables (a) A vs V_d, (b) A vs ω (c) A vs $cos(\theta)$

Species	*Percent Change*		
A. negundo	+ 1.3	+1.4	+1.9
A. ginnala	+3.5	+3.6	+3.2
A. saccharum	+3.1	+3.2	+3.6
A. macrophyllum	+4.8	+3.5	+2.7

Figure A.5: Increased mass on samara seeds. The images showcase the seeds before and after the mass augmentation process. The table presents the corresponding percentage changes in area for each seed.

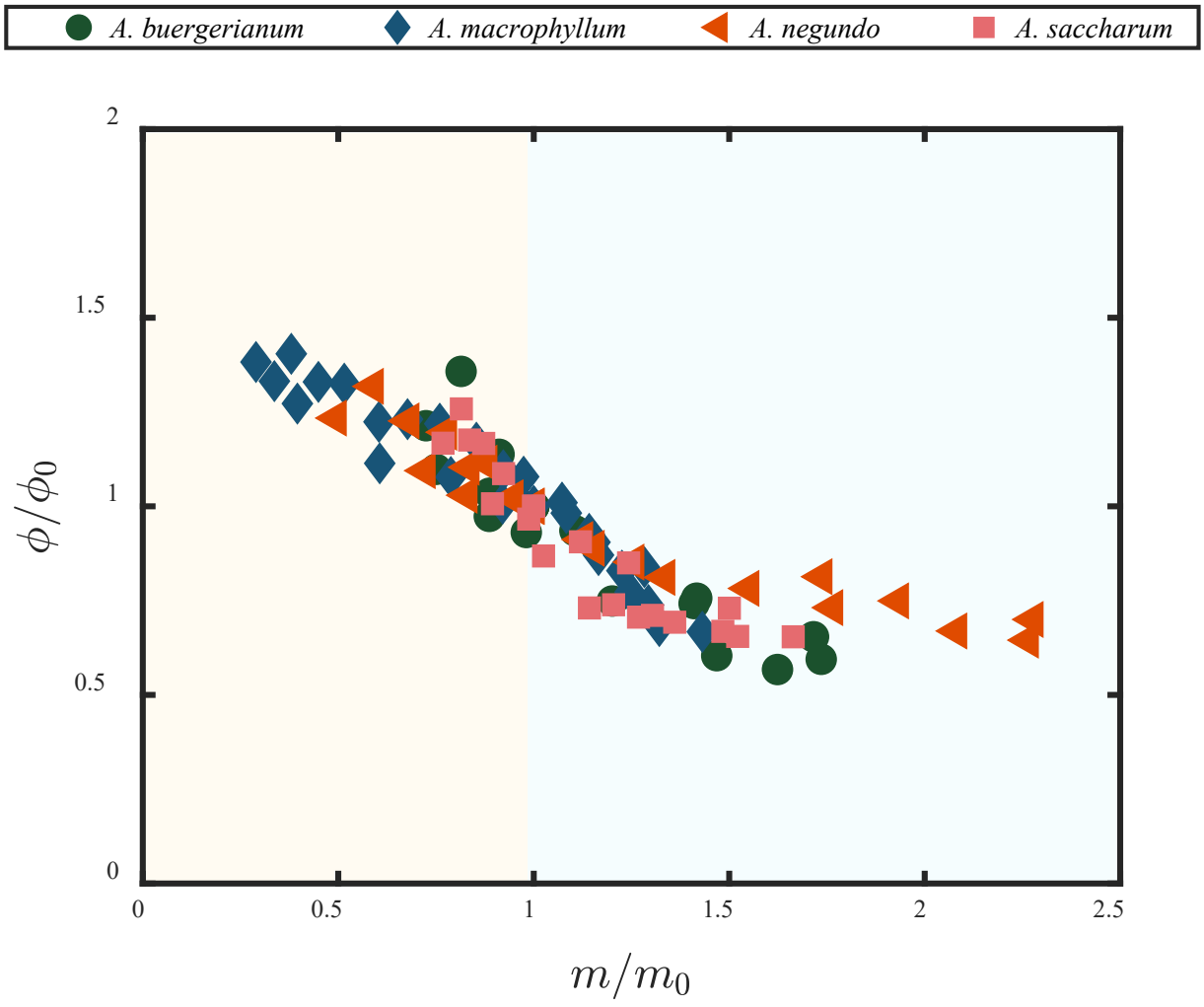

Figure A.6: Reduced angle of attack ϕ/ϕ_0 vs reduced mass m/m_0

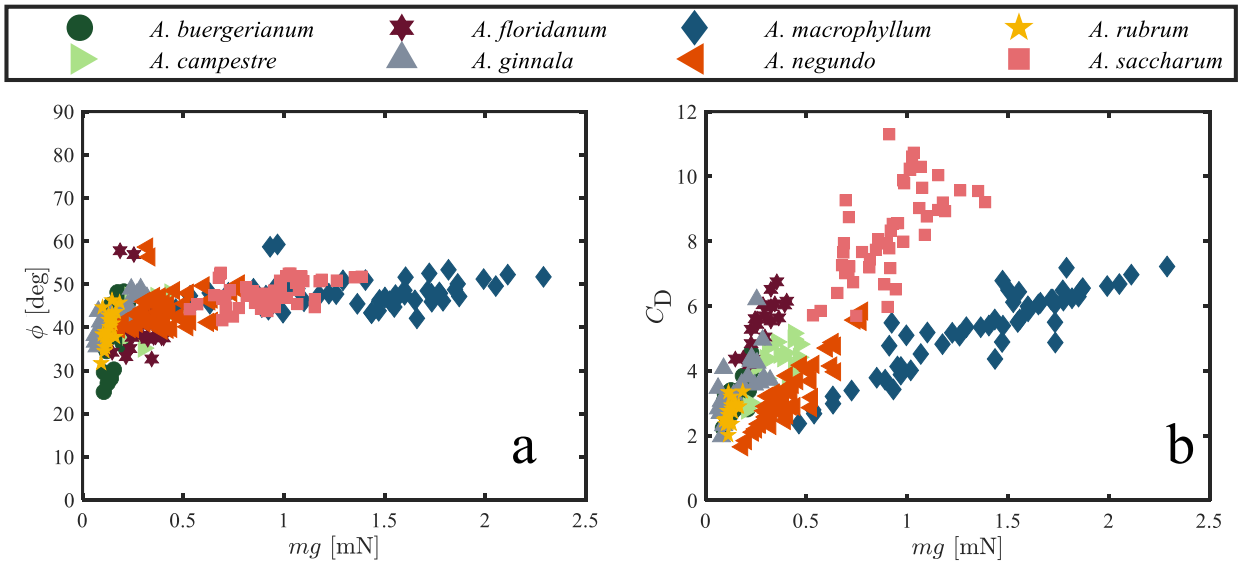

Figure A.7: Relationship between weight mg and angle of attack ϕ **(a)** Relationship between weight mg and C_D

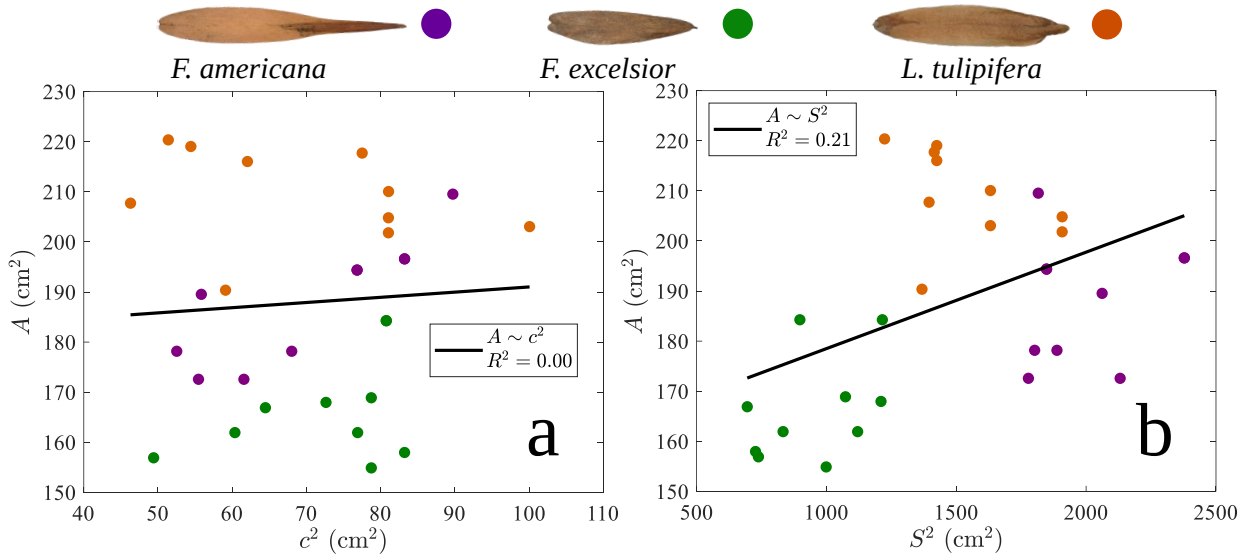

Figure A.8: Scaling relationships between wing geometry and planform area across species. (a) A vs c^2 ($R^2 = 0.00$). (b) A vs S^2

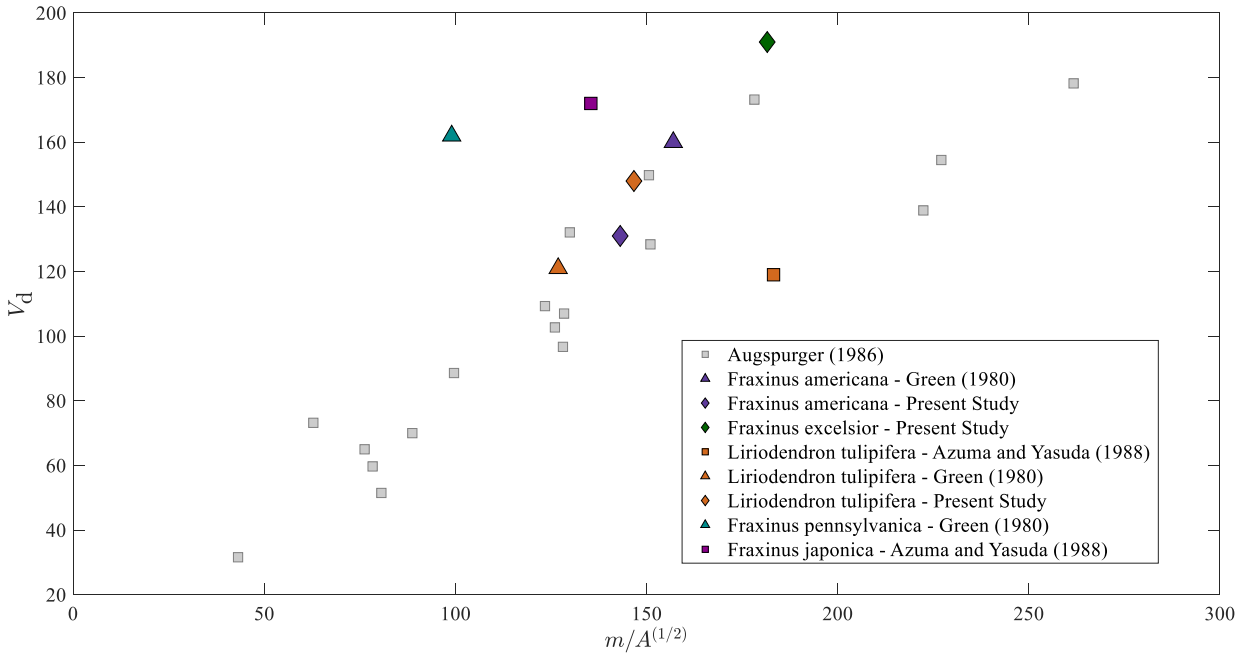

Figure A.9: Comparison of descent velocity V_d versus wing loading $m/A^{1/2}$ for five samara species across four sources. Gray markers denote data from Augspurger (1986), while colored markers distinguish species and source. Results from the present study are plotted alongside previously published data from Greene (1990), Azuma and Yasuda (1988), and Augspurger (1986). Each marker shape corresponds to a unique source, and each species is shown in a distinct color.

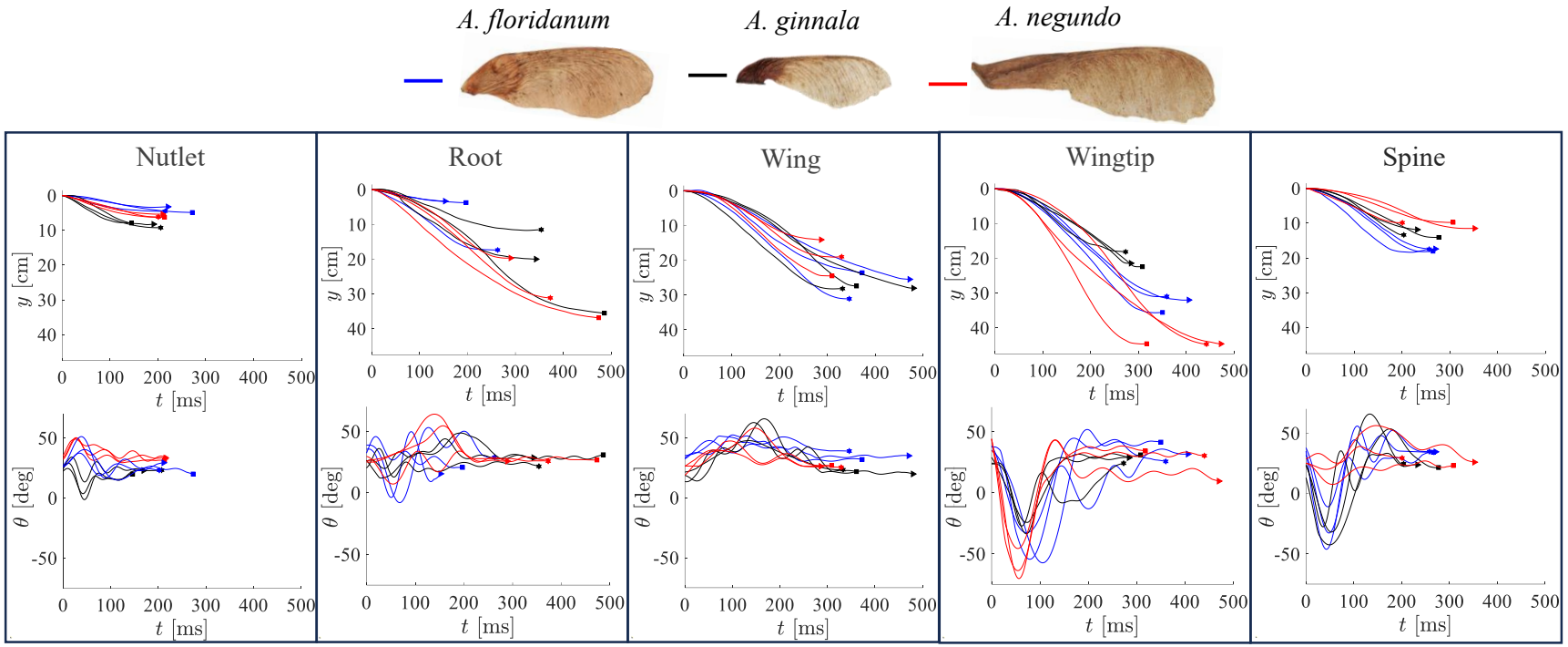

Measurement	Nutlet	Root	Wing	Wingtip	Spine
L (cm)	23 ± 3	30±8	50±8	79±6	29±6
$\dot{\theta}_{\mathrm{m}}$ (°)	8 ± 2	1 ± 9	-3 ± 4	-20 ± 7	-15 ± 9
$\dot{y}_{\mathrm{m}}$ (cm)	31 ± 10	40 ± 12	68 ± 14	85 ± 11	48 ± 15

Figure A.10: Temporal tracks of the vertical position (y) and coning angle (θ) for each of our distinguished impact regions. Impact regions are separated by column. Each plot displays data from three trials per species from impact to recovery. The shapes terminating each curve allow the reader to connect unique impacts column to column.

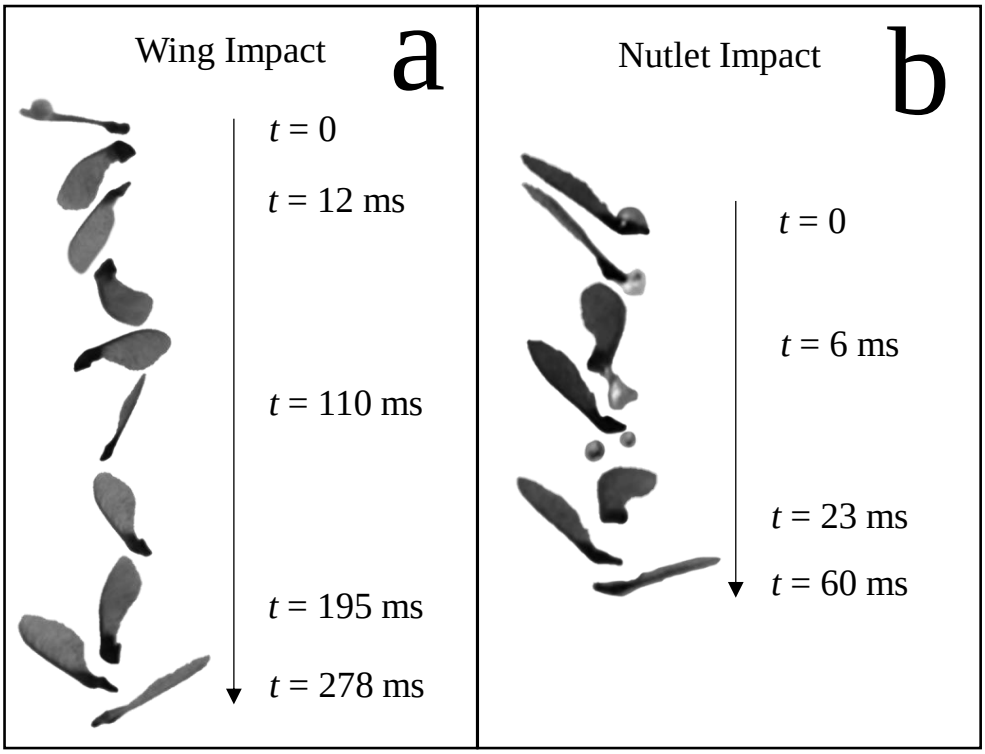

Figure A.11: High-speed impacts. (a) Aggregated image sequence of an *A ginnala* being impacted on the wing by a drop traveling at 77 cm/s. (b) Aggregated image sequence of an *A ginnala* being impacted on the nutlet by a drop traveling at 78 cm/s.

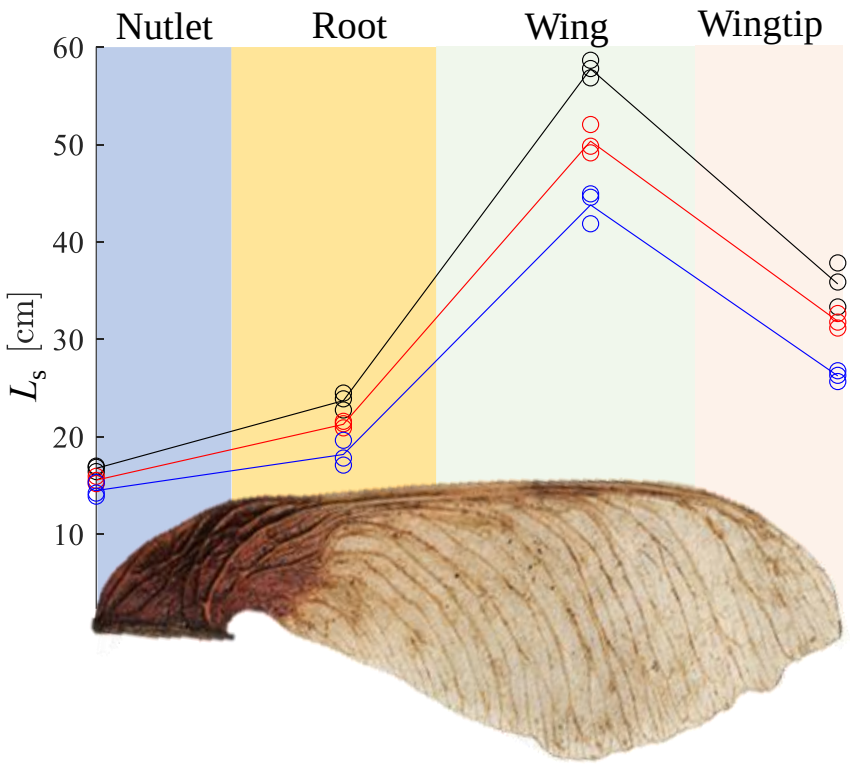

Figure A.12: Rotation initiation distance L_s for drops placed on samaras before release into the wind tunnel.

Appendix B

Rolling samaras are robust to mass and area changes

The autorotation of *Liriodendron tulipifera*, *Fraxinus americana*, and *Fraxinus excelsior* makes these species remarkably robust against perturbations caused by added mass. When mass is increased at the nutlet, the overall moment of inertia rises, slightly altering the balance between gravitational and aerodynamic torques. *L. tulipifera* exhibits a greater change in coning angle than *F. americana* or *F. excelsior*, which can be attributed to its naturally concentrated nutlet mass. The heavier nutlet amplifies asymmetry in the aerodynamic torque distribution, leading to larger deviations in precessional motion. In contrast, the more evenly distributed mass of *F. americana* and *F. excelsior* results in smaller angular adjustments and steadier autorotation.

Both *F. americana* and *F. excelsior* display increases in precessional velocity (ω_p) and rolling velocity (ω_r) as additional mass is introduced. The near-linear trends in normalized precessional and rotational velocity with normalized mass (m/m_0) suggest a proportional aerodynamic response. As the descent speed increases to balance the higher effective weight, the rotational rate scales accordingly to maintain a quasi-steady lift distribution across the wing. The persistence of this proportionality highlights the aerodynamic adaptability of rolling samaras, which self-adjust their kinematics to preserve stability despite perturbations to their inertial properties **Fig.B.1**.

Area reduction experiments produce a similar effect by increasing wing loading (m/A). As surface area decreases, the descent velocity (V/V_0) and rolling velocity (ω/ω_0) both rise. The higher velocities reflect the need to generate sufficient lift to counterbalance weight on a smaller planform, consistent with quasi-steady aerodynamic scaling ($L \propto \rho V^2 A$). *F. americana* exhibits a nearly linear trend in V/V_0 with m/m_0, indicating that its coupled rolling–precessional motion allows efficient aerodynamic compensation across a range of added mass or reduced area conditions **Fig.B.1**.

Rolling samaras sustain dynamically stable descent even when geometry and inertia are altered. Coupled rolling and precessional motions appear to act as passive stabilizing mechanisms, redistributing aerodynamic forces in real time to counter the effects of mass or area perturbations **Fig.B.1**.

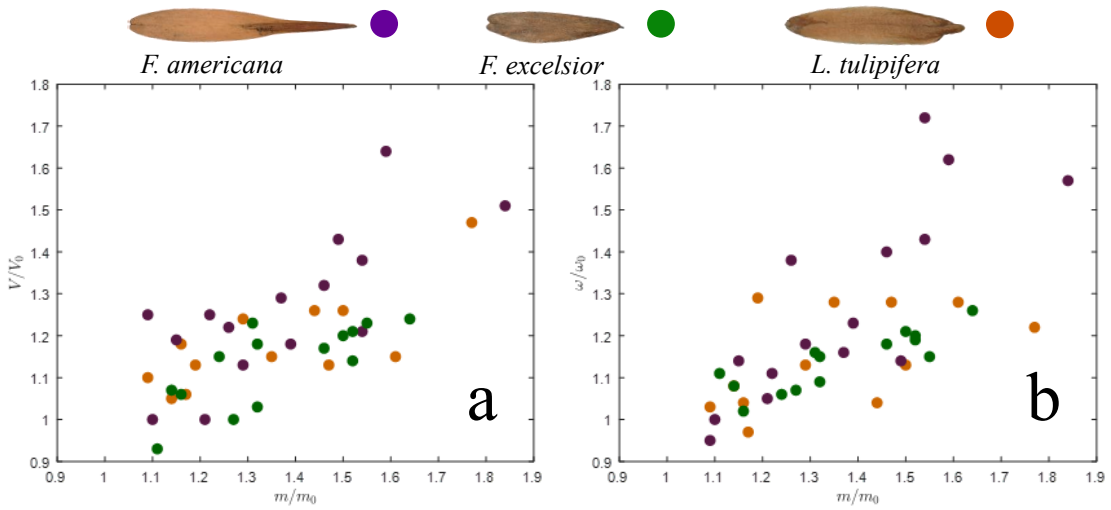

Figure B.1: Normalized descent and rotational velocity as functions of normalized mass for rolling samaras. **(a)** ratio of descent velocity V/V_0 versus mass ratio m/m_0. **(b)** ratio of rotational velocity ω/ω_0 versus mass ratio m/m_0.

Appendix C
Rolling samaras survive collisions with raindrops

Similarly to *Acer* samaras, *Liriodendron tulipifera* exhibits remarkable resilience to raindrop impacts, with recovery of autorotation or rolling motion dependent on the ability to shed residual water. In both species, recovery is governed by the balance between aerodynamic and capillary forces acting immediately after impact. When a raindrop impinges against the direction of rotation, recovery depends strongly on the location of impact. In *L. tulipifera*, drops that strike the wing are more likely to allow rapid recovery compared to those impacting the nutlet.

The seed struggles to shed water deposited directly on the nutlet, as the center of rotation experiences only weak centripetal forces during rolling. Without sufficient rotation, residual water remains pinned to the nutlet surface, delaying recovery. In contrast, drops that impact the wing experience higher tangential velocities and centrifugal acceleration as rolling resumes. The hydrophobic cuticle of the wing promotes drop detachment, and the resulting asymmetric shedding often assists in reinitiating roll.

When the impact opposes the direction of rotation, recovery distance and time both increase because the raindrop imparts a counterrotational impulse that must be overcome before stable motion is re-established. Events of this kind frequently cause a temporary stall in rolling, analogous to the brief pauses observed in *Acer* samaras after high-momentum wingtip impacts. Once the excess water mass is expelled, *L. tulipifera* resumes rolling with a coning angle and rotational frequency comparable to pre-impact conditions.

Impacts that coincide with the direction of rotation permit residual water to roll off the surface almost immediately. Continued rotation accelerates drainage, allowing the seed to maintain aerodynamic stability. Impacts on the sharp edge of the nutlet produce rapid drop fragmentation and dispersion, as seen in **Fig.C.1**. The localized shedding minimizes added loading and enables continuous autorotation with minimal disruption.

Overall, the recovery behavior of *L. tulipifera* parallels that of *Acer* samaras in its reliance on rapid drop shedding and aerodynamic stabilization but differs in the dynamics of recovery due to the rolling degree of freedom. Whereas *Acer* samaras primarily restore autorotational coning through centripetal acceleration and wing-generated torque, rolling samaras must also reestablish spanwise rotation, a process more sensitive to nutlet wetting and localized stalling. Both morphologies demonstrate a robust ability to withstand and recover from rain impacts, emphasizing the aerodynamic stability inherent in their passive flight mechanisms.

Figure C.1: Drop impact on the nutlet of a *L. tulipfidera* rolling samara illustrated with composite frames and tracked motion.

The results align with the findings reported in Schaeffer *et al.* (2024), highlighting that rolling samaras recover with comparable resilience to classical maple samaras, yet through distinct kinematic pathways shaped by their rolling motion.

Appendix D
Particle Image Velocimetry in Samaras

Particle Image Velocimetry (PIV) provides a quantitative window into the flow fields surrounding autorotating samaras. When samaras descend, they generate strong vortices along their leading edges and tips showing structures that sustain lift and slow descent. PIV captures these vortices by seeding the air with tracer particles and illuminating them with a laser sheet. Successive images are then cross-correlated to determine local velocity vectors, enabling researchers to reconstruct vorticity, circulation, and flow topology around the rotating wings.

In maple (*Acer*) samaras, PIV has revealed the formation of a stable leading-edge vortex (LEV) that remains attached throughout the rotation cycle, analogous to insect wings in hovering flight. This attached vortex generates a low-pressure region above the wing, producing steady lift even at low Reynolds numbers. The flow reattaches and sheds periodically, leading to a quasi-steady aerodynamic regime that balances descent velocity and rotation rate. Studies such as those by Lentink *et al.*[73] and Lee *et al.*[177] demonstrate how LEV stability depends on wing camber, twist, and the asymmetric mass distribution around the nutlet.

For double or paired samaras, PIV uncovers even more intricate vortex dynamics. The counter-rotating seeds shed interacting vortices that can merge, distort, or cancel, producing transient wake structures and unsteady pressure fields between the wings. These coupled aerodynamic interactions challenge two-dimensional PIV approaches, as the flow around each wing is inherently three-dimensional and time-varying. The complexity of these flows means that planar PIV alone cannot resolve the full vortex topology. Tomographic PIV, which reconstructs volumetric flow fields from multiple camera perspectives, is therefore required to fully capture the three-dimensional nature of the vortices forming around and between the autorotating wings. Such measurements are critical for understanding how paired samaras balance aerodynamic forces, maintain stability, and interact within shared flow environments.

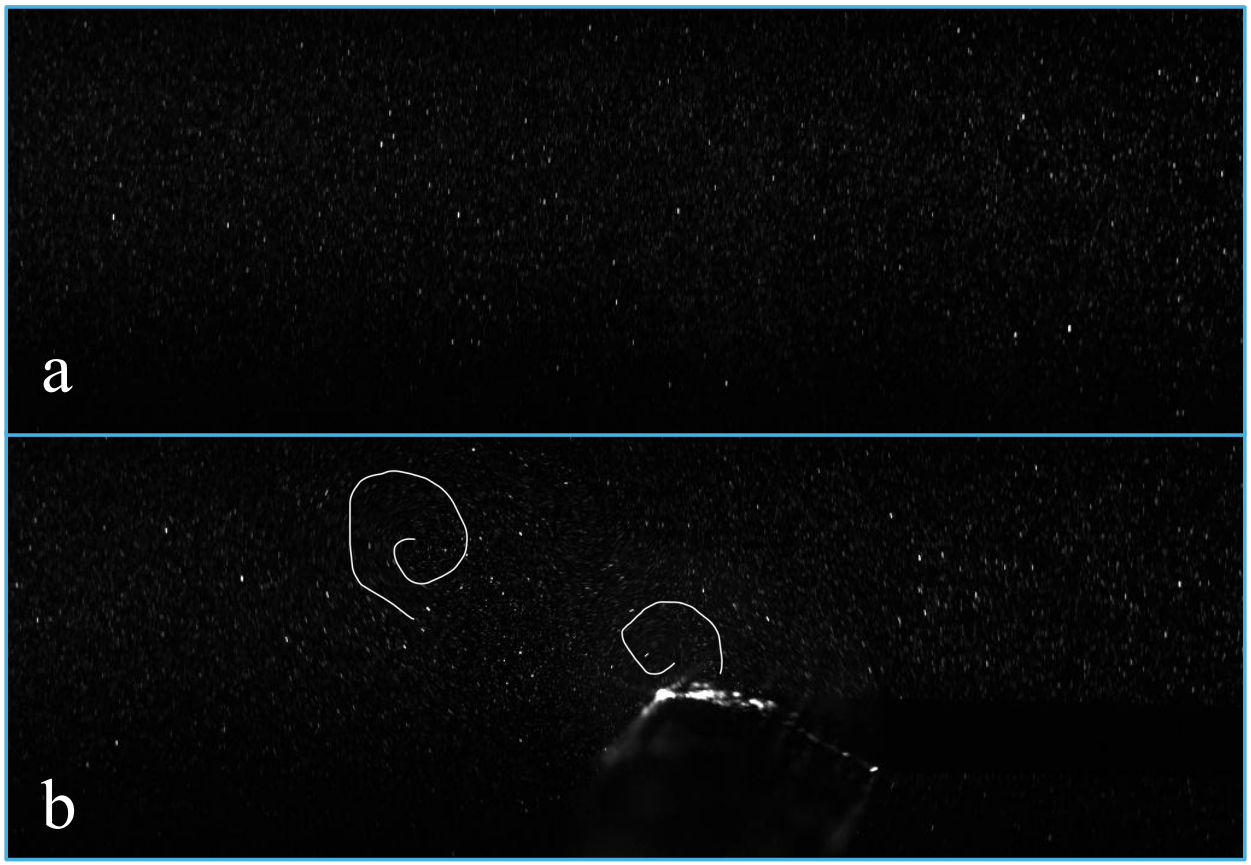

Figure D.1: Planar PIV visualization of *L. tulipfidera* samara in a laser sheet. (a) shows the seeded flow before the samara intersect the sheet. (b) shows the samaras passing through the sheet near the holder; particle streaking reveals coherent spiral structures in the wake, with white overlays indicating the approximate vortex cores shed by each wing. While planar PIV highlights these coherent features and their interaction, the intrinsically three-dimensional, time-varying flow around each wing suggests that tomographic PIV would be required to fully resolve the 3D vortex topology formed around and between the two autorotating samaras.

Vita

Breanna M. Schaeffer was born in Ruidoso, New Mexico, and raised in Alamogordo, New Mexico, where she graduated as valedictorian from Alamogordo High School. She earned both her Bachelor of Science and Master of Science degrees in Mechanical Engineering from the University of New Mexico. During her master's program, her passion for research and discovery led her to pursue a doctoral degree.

She was awarded the Tennessee Top 100 Fellowship upon admittance to the University of Tennessee, Knoxville, where she earned her Doctor of Philosophy in Mechanical Engineering. Her dissertation, titled *"Morphological and Dynamic Perturbations of Autorotating Samaras,"* explores the aerodynamic behavior and resilience of wind-dispersed samaras. During her doctoral studies, Breanna served as a graduate teaching assistant, mentored undergraduate researchers, and completed a year of service with AmeriCorps, teaching STEM education to students and families in the Knoxville community.

Breanna married her husband during her time at UTK, and his encouragement and support proved invaluable throughout her graduate studies. She extends heartfelt thanks to her husband, friends, and family for their unwavering belief in her.